Evaluating Critical Design Parameters of Small Airships Through Analytical Tools

by

Hemil PATEL

THESIS PRESENTED TO ÉCOLE DE TECHNOLOGIE SUPÉRIEURE
IN PARTIAL FULFILLMENT OF A MASTER'S DEGREE
WITH THESIS IN AEROSPACE ENGINEERING
M.A.Sc.

MONTREAL, MARCH 31, 2025

ÉCOLE DE TECHNOLOGIE SUPÉRIEURE
UNIVERSITÉ DU QUÉBEC

BOARD OF EXAMINERS

THIS THESIS HAS BEEN EVALUATED

BY THE FOLLOWING BOARD OF EXAMINERS

Mr. David St-Onge, Thesis supervisor
Department of Mechanical Engineering, École de Technologie Supérieure

Mr. Patrick Germain, Chair, Board of Examiners
Department of Aerospace Engineering, École de Technologie Supérieure

Mr. Azzeddine Soulaïmani, Member of the Jury
Department of Mechanical Engineering, École de Technologie Supérieure

THIS THESIS WAS PRESENTED AND DEFENDED

IN THE PRESENCE OF A BOARD OF EXAMINERS AND THE PUBLIC

ON MARCH 28, 2025

AT ÉCOLE DE TECHNOLOGIE SUPÉRIEURE

ACKNOWLEDGEMENTS

First, I want to thank my research supervisor, Professor David St-Onge. His constant support and guidance have been crucial throughout my studies. His encouragement to try new things and push my boundaries has shaped my research.

I am also grateful to my colleagues at INIT Robots, especially Rafael, Nerea, Aminata, and Corentin. Their feedback and help have been incredibly valuable. Special thanks to Afsaneh and Louis at INIT Robots for their assistance with experimental setups. It would have been much tougher to continue my research without their help.

Thanks to Professor Nicolas Reeves for letting my team and me be part of his project, "Scutigera." I appreciate his guidance and support in organizing our work. Most importantly, I want to thank my parents, Sohiniben and Harshadbhai, and my sisters, Heta and Shweta. Their belief in me has always been a huge source of motivation that helped me push past my limits.

Analyse des paramètres critiques de conception des petits dirigeables à l'aide d'outils analytiques

Hemil PATEL

RÉSUMÉ

Les dirigeables sont des aéronefs polyvalents à sustentation par flottabilité, adaptés à des applications allant de l'observation aérienne au transport de marchandises. Contrairement aux dirigeables rigides, les dirigeables non rigides (ou blimps) reposent uniquement sur la pression interne du gaz (généralement de l'hélium, de l'hydrogène ou un mélange des deux) pour maintenir leur forme, offrant ainsi simplicité et adaptabilité, mais au prix d'une sensibilité accrue aux déformations induites par le stress. Ce compromis affecte ultimement d'autres aspects critiques des performances, notamment l'aérostatisme, l'aérodynamique, l'inertie et la rigidité structurelle.

Cette étude aborde ces défis en développant un cadre paramétrique complet pour évaluer la portance, la perméabilité, la traînée aérodynamique, la masse ajoutée, la rigidité et l'esthétique. Quatre géométries la sphère, l'ellipsoïde oblat, l'ellipsoïde prolato et le cylindre elliptique sont analysées à l'aide d'outils analytiques personnalisés et commerciaux, les résultats étant validés par des méthodes numériques et analytiques. Les résultats obtenus sont présentés sous forme d'un ensemble de données collectif, accompagnés de plusieurs cas d'utilisation particulièrement pertinents pour des opérations de petite taille ou en intérieur, qui doivent fonctionner efficacement et en toute sécurité dans des espaces confinés et nécessitent souvent une infrastructure minimale.

Les conclusions clés révèlent que, parmi les géométries étudiées, les formes sphériques excellent en portance, les ellipsoïdes prolato offrent de meilleures caractéristiques en termes de traînée aérodynamique et de masse ajoutée, les cylindres elliptiques possèdent une rigidité structurelle et des propriétés de masse ajoutée favorables, et les ellipsoïdes oblat présentent un minimum de plis. En intégrant des facteurs moins explorés tels que la perméabilité des matériaux et l'attrait visuel, ce travail élargit les considérations traditionnelles de conception des dirigeables. Le cadre proposé soutient des solutions sur mesure pour des applications intérieures de petite taille et d'autres applications spécifiques, permettant aux nouveaux concepteurs d'équilibrer les compromis entre les différentes performances.

Mots-clés: Dirigeable, Plus léger que l'air, Traînée de forme, Masse ajoutée, Rigidité structurale, Méthode des éléments de frontière, Méthode de conception, Simulation

Evaluating Critical Design Parameters of Small Airships Through Analytical Tools

Hemil PATEL

ABSTRACT

Airships are versatile lighter-than-air aerial vehicles suitable for applications ranging from aerial observation to cargo transport. Unlike rigid airships, non-rigid airships or blimps rely solely on the internal gas pressure (commonly helium, hydrogen or a mixture of both) to maintain their shape, offering simplicity and adaptability at the cost of increased sensitivity to stress-induced deformations. This tradeoff ultimately affects other critical aspects of performance, including aerostatics, aerodynamics, inertia and structural rigidity.

This study addresses these challenges by developing a comprehensive parametric framework to evaluate buoyancy, permeability, aerodynamic drag, added mass, rigidity, and aesthetics. Four geometries sphere, oblate ellipsoid, prolate ellipsoid, and elliptical cylinder are analyzed using custom and general analytical tools, with results validated through numerical and analytical methods. The available results are presented into a collective use cases along with several use cases utilizing the data, particularly relevant for small or indoor operations, which must operate efficiently with safety in confined spaces and can often house minimal infrastructure.

Key findings reveal that, among the geometries studied, spherical shapes excel in buoyancy, prolate ellipsoids offer superior aerodynamic drag and added mass characteristics, elliptical cylinders possess favorable structural rigidity and added mass properties, and oblate ellipsoids exhibit minimal wrinkling. By incorporating less-explored factors such as material permeability and visual appeal, this work expands traditional airship design considerations. The proposed framework supports tailored solutions for small indoor and other specific applications, enabling new designers to balance trade offs among competing performance metrics.

Keywords: Blimp, Lighter than air, Form drag, Added mass, Structural rigidity, Boundary element method, Design methodology, Simulation

TABLE OF CONTENTS

LIST OF TABLES

LIST OF FIGURES

LIST OF ABBREVIATIONS

BEM	Boundary Element Method
CAD	Computer Aided Design
CFD	Computational Fluid Dynamics
FEM	Finite Element Method
FEA	Finite Element Analysis
FVM	Finite Volume Method
HTA	Heavier-than-air
LTA	Lighter-than-air
UAV	Unmanned Aerial Vehicle
SA	Surface Area
SIMPLE	Semi-Implicit Method for Pressure Linked equation

LIST OF SYMBOLS AND UNITS OF MEASUREMENTS

B	Buoyancy force (N)
V	Volume of the subjected body (m^3)
ρ_a	Density of the surrounding air (m^3)
L	Lift force (N)
W	Weight of the body (Kg)
L_d	Disposable lift (N)
ρ_g	Density of the active gas (m^3)
W_b	Weight of the inflatable bladder (Kg)
m_p	Mass of the available payload (Kg)
SA	Surface area of the body (m^2)
t	Thickness of the membrane material (m)
m_m	Mass of the membrane material (Kg)
M_{po}	Mass of the observed payload (Kg)
M_{pr}	Mass of the required payload (Kg)
m_{exp}	Estimated percentage of membrane expansion (%)
D_p	Parasitic drag (N)
D_i	Induced drag (N)
D_f	Form drag (N)
D_{int}	Interference drag (N)

D_s	Skin Friction drag (N)
G_k	Turbulent kinetic energy
G_b	Turbulent kinetic energy due to buoyancy forces
Y_m	Ratio of changing dilatation in compressive turbulence to overall dissipation rate.
C_1, C_2	Constants in $k-\epsilon$ transport equations
$\sigma_k, \sigma_\epsilon$	Prandtl number for k and ϵ terms
S_k, S_ϵ	User-defined source terms in $k-\epsilon$ transport equation
V_r	Relative wind velocity (m/s)
C_d	Coefficient of drag (N)
$\phi = \phi_1 \dots \phi_6$	Potential flows of the body
Δ	Laplace operator
n	Normal unit vector pointing outwards
P	Arbitrary point on the surface of the body
v_p	Velocity vector of point P (m/s)
$v = u, v, w$	Velocity at the origin of body frame (m/s)
$p = x_p, y_p, z_p$	Vector position from origin to point P (m)
$w = p, q, r$	Vector of angular velocity (m/s)
$d(P, Q)$	Distance between integral variable P and point on the surface of body Q (m)
λ_{ij}	Added mass coefficients of the body
k_{ij}	Added mass of the body (kg)

m_{ij}	Mass matrix of the body
σ_{sphere}	Hoop stress of the spherical thin-shell body (MPa)
E	Tensile modulus of the material (MPa)
v	Poisson's ratio
S_x, S_y, S_z	Geometry frontal area in x, y and z axis
$M(\dot{v})$	Total mass matrix
$C(v)$	Coriolis and centripetal matrices
D	Drag coefficient damping matrix
τ	Generalized force vector applied by actuators or external fields

INTRODUCTION

Aircraft have long been a cornerstone of modern transportation and technology, significantly influencing various aspects of global activity, ranging from commercial aviation and military operations to scientific research and recreational activities. Typically, these aircraft are divided into two main groups based on their flight mechanics: Heavier than air (HTA) types, such as airplanes, helicopters, unmanned aerial vehicles (UAVs), and drones, and Lighter than air (LTA) types, including hot air balloons and airships. Each group offers distinct advantages and faces specific operational limitations, often determined by the aircraft's structural design, propulsion system, and operational requirements.

After the Hindenburg disaster in 1937, HTA craft has maintained dominance in most aviation sectors. Airplanes rely on fixed wings to attain aerodynamic lift, enabling longer flight range and payload capacity to become a prominent factor for global long distance transport. Although, despite a century of technological advancements and standardized design methodologies (Raymer (2006)), almost all fixed wing aircraft typically require extensive infrastructure, such as runways, which can be impractical or impossible to build in remote or sensitive environments. Similarly, rotary wing aircraft (helicopters) offer the advantage of vertical takeoff and landing, reducing some infrastructure demands, yet they are constrained by relatively lower endurance and payload capacity.

In recent years, small HTA craft like, drones have proven useful in confined indoor applications such as warehouse inventory management, area surveillance, and research in controlled environments. However, drones face critical limitations in flight duration, payload capacity, and potential collision hazards in tight spaces. Their sole reliance on batteries often limits them between smaller sizes or short operation times, which prevents long endurance missions or continuous monitoring tasks.

Here, buoyant body aircraft, like airships or dirigibles, present a viable alternative to conventional HTA aircraft. Particularly, small, non rigid airships (often termed blimps) emerge as a compelling alternative. Unlike drones that rely purely on aerodynamic or rotary lift, small blimps attain a majority of their lift force by using lighter than air gases such as helium and hydrogen. This buoyancy driven lift allows airships to hover for extended periods with reduced energy demands, making them particularly well suited for long duration flights. Moreover, small airships inherently pose lower collision risks due to their soft envelopes and relatively slow, stable flight dynamics in indoor spaces. These attributes make them particularly attractive for tasks such as Indoor surveillance and monitoring: Large warehouses, sports arenas, or conference halls where occupant safety is critical, Research and data collection: Non intrusive platforms for instruments or sensors that must remain flying for extended periods, Entertainment and advertising: Blimps equipped with displays or banners that can safely navigate among crowds and venue without significant collision risks.

Despite these advantages, designing small indoor blimps has only recently gained increased attention. Many of the existing design guidelines and performance analyses focus on large outdoor airships (e.g., Burgess (2004)) or rely on simplified aerodynamic assumptions, leaving a gap in systematic methodologies that address the unique parameters of small-scale, non-rigid envelopes operating at low speeds in confined spaces. In such cases, the interplay among buoyancy, envelope rigidity, permeability, and internal pressure becomes more significant, leading to stricter material constraints and the potential for envelope wrinkling. Furthermore, most conventional studies often isolate individual parameters (e.g., drag or buoyancy) rather than explore how different physical effects influence each other and the overall airship performance. For instance, a blimp optimized for reduced drag might inadvertently increase wrinkling due to non-uniform pressure distributions, while reinforcing the structural rigidity of the envelope by selecting more rigid material might add weight, reducing net buoyancy. A comprehensive parametric analysis that captures these trade-offs for small indoor airships is largely absent from

the current literature. This study aims to bridge that gap by developing and demonstrating a

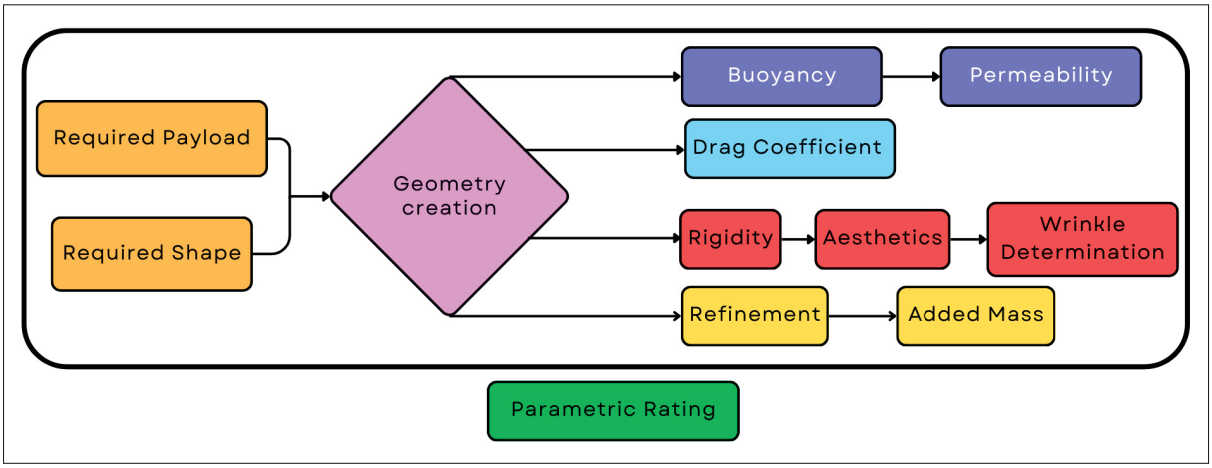

Figure 0.1 Design methodology in focus: Flowchart of key parameters and processes

flexible, data-driven design methodology specific to small, non-rigid airships. The focus is on creating a robust parametric framework that enables both experienced designers to improve their concepts and new users to explore and select blimp shapes from sphere, oblate ellipsoid, prolate ellipsoid, and elliptical cylinder based on critical operational parameters such as payload, envelope volume, internal pressure, and flight speed range. The methodology incorporates a set of methodologies and custom analytical tools to evaluate key performance metrics:

- **Aerostatics calculation using a simple custom python script:** Computes net buoyant force of shape-payload combination selection from aerostatics and material properties. It also estimates flight lift autonomy through a buoyancy cycle under ideal indoor conditions.
- **Added mass calculation using potential theory:** Employs potential flow theory to estimate added mass coefficients for each geometry. The tool accounts for fluid inertia effects during translational motion in low-speed conditions.
- **Aerodynamic drag calculation using ANSYS FLUENT:** Performs CFD simulations in a confined domain to evaluate drag forces under a range of Reynolds numbers for validation cases and various angles of attacks for each shape. The setup includes mesh refinement, wall boundaries, and the realizable $k-\epsilon$ turbulence model.

- **Structural simulation using ABAQUS FLUID-Cavity:** Models the pressure–structure interaction of the inflated membrane envelope using fluid cavity conditions. The analysis captures shape deformation during translation in the x-axis and assesses envelope rigidity under internal pressure.
- **Wrinkle analysis using a simple custom python script:** Estimates wrinkle formation by comparing strain in the discretized local membrane strain against their neighbors. It offers a fast approximation of shape smoothness and aesthetic quality for designed and over inflated pressures.

The broader scope of this work is to establish a comprehensive use cases that not only captures typical values across the studied geometries but also supports scenario-specific extensions by following the outlined methodology. By integrating analytical and computational assessments into a unified resource, the study presents a scalable and accessible framework. Users can either adopt the pre-validated results or extend the approach to meet customized design objectives, thereby optimizing airship performance for mission requirements such as endurance, maneuverability, or operational safety, as illustrated in the process chart shown in Figure 0.1.

CHAPTER 1

LITERATURE REVIEW

The following chapter offers a detailed review of current research related to the methodology employed in this thesis. It discusses the foundational aspects of airship design parameters including dynamics modeling, aerostatics, aerodynamics, added mass, and structural considerations along with the analytical and numerical tools utilized for their assessment.

1.1 Dynamic Modeling of Lighter than air Bodies

Although this thesis primarily focuses on using analytical and numerical tools to define a design process for small, non rigid indoor airships encompassing both conventional and unconventional parameters, there is substantial literature available on airship dynamics modeling that uses many of the same parameters, sometimes even more by the inclusion of propulsion and control systems. Often, these models address specific geometries with complex architectures. Nonetheless, it is extremely important to consider an overall dynamic model of airships to fully realize the potential applications of the parameters discussed in the thesis.

Towards this, a simplified six degree of freedom (6-DOF) dynamic equation of motions is presented by Li, Nahon & Sharf (2011) describing the translational, rotational and inertial behavior of airships. The general form of equation is given such as:

$$\begin{bmatrix} mI_{3\times3} & -mr_G \\ mr_G & J \end{bmatrix} \begin{bmatrix} \dot{v} \\ \dot{\omega} \end{bmatrix} + \begin{bmatrix} m\omega^{\times}v - m\omega^{\times}r_G\omega \\ mr_G\omega^{\times}v + \omega^{\times}J\omega \end{bmatrix} = \begin{bmatrix} mg \\ mr_Gg \end{bmatrix} - \begin{bmatrix} \rho V_B g \\ \rho V_B r_V g \end{bmatrix} + \begin{bmatrix} F_{AD} \\ M_{AD} \end{bmatrix} + \begin{bmatrix} F_C \\ M_C \end{bmatrix} \quad (1.1)$$

where m is the total mass including envelope, $I_{3\times3}$ is the identity matrix, r_G and r_V are the position vectors from the center of gravity and center of volume respectively, J is the rotational inertia matrix, v is the linear velocity vector, ω is the angular velocity vector, $\omega^{\times}$ denotes the skew-symmetric matrix of ω, g is the gravity vector, V_B is the displaced volume of air, F_{AD}, M_{AD} are aerodynamic forces and moments, and F_C, M_C are control forces and moments. Li & Nahon (2007) discuss a similar detailed dynamic model specifically tailored for conventional ellipsoidal

airships, incorporating aerodynamic and added mass effects through empirical data and analytical methods. Their model was validated with real flight test results and then linearized around equilibrium points, supporting more efficient simulations.

Further extending these foundational techniques, Bennaceur & Azouz (2012) develop a dynamic model that accounts for flexible envelope effects and thruster generated forces in unconventional airship configurations. By combining aerodynamic properties with numerical simulations, they demonstrate how nonlinear dynamic responses can be accurately captured across a range of operational scenarios, highlighting the importance of modeling non rigid airship envelopes. Mueller, Paluszek & Zhao (2004) investigate a hybrid airship design that integrates lighter than air principles with fixed wing gliding mechanics. Their research underscores the feasibility of combining aerodynamic and buoyancy based modeling to bridge concepts from fixed wing dynamics with those relevant to lighter than air vehicles.

Focusing more closely on autonomous and indoor operations, St-Onge, Gosselin & Reeves (2015) propose a robust nonlinear dynamics model for autonomous airship navigation. They emphasize the challenges of low speed maneuvers and confined environments, where stable hovering is critical. Their approach integrates advanced aerodynamic modeling, structural flexibility, and control responsiveness into a single framework, mirroring realistic indoor flight conditions. Gomes & Ramos (1998) presented an old but still practical modeling framework for indoor airships, building simplified rigid body motion equations and thruster dynamics to guide control strategies in small scale environments. This methodology offers essential sizing relationships among envelope geometry, onboard electronics, and maneuvering performance, providing designers with actionable guidelines for indoor applications.

Taken together, these dynamic modeling studies form a solid foundation for understanding both conventional and unconventional airship behavior. Nevertheless, most methods are still aimed at streamlined, ellipsoidal, or their study specific configurations and rely primarily on semi empirical aerodynamic models. As a result, their direct applicability to small, non rigid indoor airships often with unconventional shapes and unique flight profiles remains limited. This

gap highlights the necessity for a systematic evaluation of aerostatic and aerodynamic forces, added mass influences, and structural flexibility in unconventional indoor airship geometries. Ultimately, such an effort will support comprehensive and robust dynamic modeling techniques optimized for indoor flight conditions.

1.2 Aerostatics and Aerodynamics for Lighter than air Bodies

Designing effective Lighter than Air (LTA) vehicles requires a comprehensive understanding of two fundamental disciplines: Aerostatics, which governs forces acting on a static body immersed in a fluid (e.g., buoyancy and static pressure), and aerodynamics, which deals with forces acting on bodies in motion such as lift, drag, thrust, and rotational force. Both fields are significantly influenced by a body's velocity, shape, and size, making them essential to predicting and optimizing LTA performance. Over time, methods to study these forces have evolved from basic empirical tests and mathematical derivations to advanced computational fluid dynamics (CFD) techniques. Conventional approaches often combine numerical, experimental, and analytical methods to capture accurate fluid-structure interactions and maximize design efficiency. This section reviews the key developments in aerostatics and aerodynamics, setting the groundwork for how these principle approaches can improve the parametric framework for small, non rigid indoor airships.

1.2.1 Fundamental and Numerical Approaches to Aerostatics

Numerical methods have long helped in understanding the buoyant forces acting on LTA vehicles. Archimedes' principle offers a foundational model for buoyancy, where the *gross lift* (L) of a buoyant body is calculated based on its volume (V) and the density (ρ) of the surrounding fluid Craig (1999):

$$L = V \cdot \rho \tag{1.2}$$

Craig (1999) further examined the effect of changing atmospheric conditions during ascent on ρ, underscoring how lift density fluctuates with altitude. These findings highlight that even static

flight considerations require acknowledgment of dynamic environmental factors particularly important for smaller, non rigid envelopes that operate under constrained margins on available lift.

1.2.2 Advancements in Aerodynamic Drag Calculations

Significant progress has been made in the understanding of aerodynamic drag through comprehensive theoretical frameworks such as those developed by Hoerner (1992). Drag force D typically depends on the fluid density ρ, relative velocity V, reference area S, and a drag coefficient C_d:

$$D = \frac{1}{2} \rho V^2 S C_d \tag{1.3}$$

Feng (2010) applied this formula to derive hydrodynamic drag for spheres, identifying distinct Reynolds number regimes for steady laminar flow ($Re < 1$) and transitional flow ($Re < 75$). Their validation against existing literature proves the robustness of their model further emphasizing the influence of the Reynolds number on overall flow behavior. Hengne, Korade & Jagtap (2019) extended this work by comparing drag across intermediate geometries between spheres and ellipsoids, in identifying an intermediate shape that provides an optimal balance between reduced drag with volume efficiency. A crucial insight for LTA design shapes where both aerodynamic and buoyant performance are critical.

Experimental validation although being the oldest remains a cornerstone of aerodynamic research. Takeda & Kato (1992) investigated wind tunnel blockage effects by varying model scales and tunnel cross sectional areas, proposing a blockage factor to correct for wind induced vibrations in porous bodies. Similarly, Flemmer & Banks (1986) combined wind tunnel data with mathematical approximations to evaluate drag coefficients, performing well at low Reynolds numbers but encountering challenges at higher Reynolds values ($Re > 0.3$), highlighting limitations of purely empirical methods for turbulent flow regimes. Jones & DeLaurier (1983) further examined interference effects between hulls and fins on axisymmetric bodies, yielding

acceptable results for steady flows and suggesting potential applications for unsteady flow modeling.

Dorrington (2006) alongside several other researchers have focused on unconventional designs by introducing a hybrid spherical blimp with a conical appendage. Wind tunnel tests indicated a 50% drag reduction, yet subsequent flight data revealed surface interference effects that increased drag. Wang, Fu, Duan & Shan (2010) explored tandem wing airship designs, revealing a trade off between buoyancy efficiency at 0° and stability at 45°. Additionally, Tran-Cong, Gay & Michaelides (2004) studied free fall drag for spheres in Newtonian fluids, establishing empirical correlations for Reynolds numbers ranging from 0.15 to 1500.

Modern computational methods, particularly CFD, continue to evolve with increasingly complemented numerical and experimental approaches. Reddy & Pant (2018) compared CFD analyses of prolate ellipsoid bodies using conventional fluid dynamic tools such as ANSYS Fluent and OpenFOAM to solve the Reynolds averaged Navier Stokes equations, demonstrating that careful computational modeling can yield precise results despite discrepancies from mesh variations given similar boundary conditions. Similarly, recent work by Anawati (2024) utilizes OpenFOAM to set up a CFD analysis that incorporates a turbulence intensity estimation given by $\bar{I} = 0.16\,(Re)^{-\frac{1}{8}}$, where $\bar{I}$ is the simulated range of turbulence between 1% and 10% for mimicking more realistic behavior for indoor airship operations. Furthermore, this approach details a dynamic meshing strategy where boundary conditions are varied using a Bash script in 10° increments for both pitch and yaw over a full 360° span resulting in 1369 distinct simulations per body geometry. This comprehensive use cases leads to improved determination of aerodynamic coefficients (such as CD and CM) for unconventional shapes, including non rigid indoor blimps. Building on these foundations, Wu, Wang, Huang, Liu & Lu (2015) validated CFD simulations with wind tunnel experiments, reinforcing the importance of cross method verification to test the addition of additional variables to simulate realistic conditions in computational simulations.

Carrión, Steijl, Barakos & Stewart (2016) used CFD to analyze hybrid airship designs, focusing on the contributions of stabilizers to lift and drag. Their findings revealed that while stabilizers significantly enhance lift, they also contribute to drag at high Reynolds numbers. Fei & Zhengyin (2009) investigated actuator induced flow disruptions to optimize laminar drag reduction, achieving a notable 58% improvement in aerodynamic efficiency for specific design configurations.

From Archimedean buoyancy to CFD based aerodynamic analyses, various methods have been developed to characterize forces on LTA vehicles. Numerical, experimental, and hybrid approaches each offer distinct insights and support robust design guidelines for airships. However, most studies have focused on conventional or outdoor platforms, and their applicability to small, non rigid indoor airships often featuring generic geometries and operating at low speeds in confined spaces remains limited. This review indicates that a systematic evaluation of aerodynamic and buoyant forces, added mass effects, and structural rigidity for indoor environments is available, but mostly for specific geometries. The gap is a lack of systematic, cross validated approaches that can accommodate multiple shapes and low speed flight conditions. Towards this, the thesis aims to develop a comprehensive parametric framework using the same principles demonstrated in the review to capture buoyancy, drag, and envelope geometry interactions for several geometric shapes for further optimization of indoor LTA vehicle performance.

1.3 Added Mass Computation for Lighter than air Bodies

A body moving in a surrounding fluid encounters additional resistance due to the inertia of the displaced fluid. This resistance causes the body to behave as though it has a greater effective mass than its actual mass. This phenomenon, known as added mass, is essential for understanding and analyzing the dynamic behavior of bodies in fluid environments. The added mass accounts for the virtual increase in effective mass caused by fluid inertia, making it a crucial parameter in the dynamic analysis of various structures, including ships, airships, and underwater vehicles.

The relationship between the added mass coefficients and theoretical added mass, mass coefficients aligned with their translation axis, and moment of inertia along the rotational axis of the body are derived by Korotkin (2009) in Equation 1.4, where K is the added mass coefficient, i, and j indicates the number of rows and columns for the matrices, λ is the added mass and m is the mass of their respective shapes, serve as initial reference estimations for practical applications.

$$K_{ij} = \frac{\lambda_{ij}}{m_{ij}} \tag{1.4}$$

For semi and fully immersed structures with conventional curved geometries, Korotkin (2009) provides a comprehensive set of equations for added mass estimations. To simplify the analysis of dynamic behavior, only the diagonal terms of these equations are considered, resulting in six sets of equations: three for translational motion along the principal axes and three for rotational motion about the same axes.

Another method for obtaining added mass coefficients is presented by Li & Nahon (2007), which involves modeling the dynamic behavior of a conventional airship with cruciform fins. This approach incorporates both aerostatic and aerodynamic terms into the dynamic model. The added mass coefficients for the airship's hull and fins are calculated and integrated into the model to improve its accuracy. The estimated dynamic behavior is then validated against real-world flight test data, showing strong agreement between the models. This validation demonstrates the viability of the modeling approach, particularly for expanding numerical models to handle more complex geometries. The combination of theoretical modeling and empirical validation makes this method a promising alternative for developing dynamic models of unconventional airship designs.

A popular numerical approach for directly calculating added mass terms is the Boundary Element Method (BEM). In this approach, the simulated geometry is discretized into panel like shape elements (Carbone, Martinat, Farcy & Harion (2019), Ghassemi & Yari (2011)). Velocity potential gradients between each local element and the rest of the geometry are calculated using Green's function. These gradients are then summed into a six-by-six matrix to evaluate the added

mass coefficients. However, challenges arise due to the self-influence terms in Green's function, where the diagonal elements of the influence matrix often approach zero or become irregular, leading to invariable solutions. Regularization factors are employed to mitigate this issue by regulating the terms to remain within a specific range, thereby ensuring a linear solution to the problem. These factors help overcome discrepancies caused by poor mesh quality or inferior elements, improving the robustness of the solution. Despite their effectiveness, regularization factors are often geometry-specific and may not generalize well across different shapes. Tuveri, Ceruti & Marzocca (2014) demonstrates that by carefully applying a relaxation factor, the method can provide reliable results, especially for pre-designed geometries like airships. However, limitations persist, as these factors are uniquely tied to the methods used for specific geometry generation.

A numerical approach to deriving added mass coefficients is demonstrated by Azouz, Chaabani, Lerbet & Abichou (2012), where the added mass of hybrid truncated cone airships is estimated using a 2D numerical analysis. The method involves dividing the airship into more than a dozen cross-sectional slices, each analyzed individually for its added mass contribution. These 2D results are then integrated to approximate the behavior of a 3D airship. The trajectory angle determines which 2D cross-sectional results are applied to calculate the added mass coefficient for specific motion paths. This method effectively reduces computational complexity while providing accurate results for hybrid airship geometries.

While the popular numerical approaches to determining added mass investigate their direct effect on the test geometries, general fluid solvers like ANSYS CFX and FLUENT offer an alternative to calculate hydrodynamic forces over a body (Javanmard, Mansoorzadeh & Mehr (2020)). Both tools follow a typical Computational Fluid Dynamics (CFD) approach, where the desired properties of the simulated flow such as velocity, pressure, and turbulence models are defined as input boundary conditions. The simulated geometry, created using any CAD-based design tool, acts as the boundary inside the fluid domain, which represents the flow volume. Careful consideration is given to the dimensions of the fluid domain to ensure the entire flow pattern is captured while minimizing computational cost by keeping the number of mesh elements

feasible. Hydrodynamic forces, including linear and rotational terms, can be computed using these solvers. To isolate the added mass effects, other flow-dependent forces like drag are subtracted, leaving the inertial forces associated with the acceleration terms. This methodology can also be extended (Bennaceur & Azouz (2012)) to explore the dynamic behavior of flexible airships, enabling the determination of added mass coefficients under various deformation cases and aiding in the development of control and stabilization algorithms for such designs.

In summary, understanding added mass is vital for accurately modeling the dynamic behavior of airships, particularly in contexts where fluid inertia significantly affects performance. By examining various theoretical, numerical, and CFD-based methods for determining added mass, researchers have laid a foundation that can be challenging to address without specialized analytical tools. This thesis aims to replicate the fundamental principles for calculating added mass and adapt them into a custom tool specifically designed for small, non-rigid indoor vehicles ensuring that the unique conditions of indoor LTA operations are properly accounted for.

1.4 Structural Analysis of LTA Structures

1.4.1 Wrinkle Characterization and Analysis

Structural analysis for an LTA structure determines the effectiveness and behavior of airships in delaying the eventual collapse from the wrinkled state under various loading conditions. To this avail, Su & Xu (1999) adopted a visual inspection approach for fabric wrinkle determination. Their experimental setup involved placing wrinkled fabrics over a rotating platform and exposing them to a multi-line projector. The distortion caused by wrinkles on the projected lines was captured by a camera, and a previously trained neural network analyzed the captured images to determine selected wrinkle characteristics. This approach emphasized a unique method for wrinkle density determination. A similar method was presented by Sun, Yao, Xu & Bel (2011), deploying a multi-camera setup to comprehensively capture critical wrinkle parameters, including density, orientation, and rigidity for five different fabrics. Each setup was subjected to five distinct wave patterns, systematically analyzing the differences in characteristics resulting

from each pattern. This allowed the definition of key wrinkle parameters influencing sagging behavior in fabrics.

Another approach simulating wrinkle patterns through computational means was introduced by Liu (2014), where X-shaped wrinkle patterns occurring on apparel over elbows and knees were analyzed. Their setup included 15 different fabric materials for visual wrinkle pattern characterization. Using a custom MATLAB script, simulated wrinkles were compared to real wrinkles, with a wrinkle threshold angle of 45° proposed to standardize wrinkle measurements. This approach provided critical insights into simulating and analyzing wrinkles.

1.4.2 Static Rigidity and Pressure Effects

Another rigidity parameter critical for blimps is the stress-induced distortions caused by thruster propulsion during maneuvering. These effects are generally less prevalent in semi-rigid and rigid blimps due to compensation by rigid structural elements. However, in non-rigid blimps, these distortions can adversely affect flight dynamics if not addressed adequately. Incorporating light structural elements like wires and struts in semi-rigid designs can strike a balance between deflection and rigidity. Tensairity (Luchsinger, Pedretti, Steingruber & Pedretti (2004), Suñol & Vučinić (2020)) is a promising approach where internal lifting fluid pressure is combined with tensioned strings and compression-resistant elements to maintain shape and rigidity. This concept has been demonstrated in the MAAT (Multi-body Advanced Airship for Transport), with its potential evaluated using Finite Element Analysis (FEA) in Abaqus.

The static rigidity effects in LTA structures are influenced by the disparity between internal and external fluid pressures. Vacuum-based concepts, while frequently discussed in theory (Cranston, AlGhofaily & Palazotto (2017)), are often proposed only for rigid airship structures. These designs involve light, dense mesh structures enveloped by skin fabric. Analytical results typically identify icosahedron shapes as optimal for structural efficiency. However, structural weight frequently exceeds lifting capacity, limiting practical applications of vacuum-based

designs. Validation through analytical tools like ANSYS and Abaqus has shown these concepts to be theoretically promising but challenging to implement due to weight limitations.

Another key challenge is the interaction between structural rigidity and aerodynamic forces. Coupled simulations can capture interdependent effects such as bending caused by thermal loads (Wang, Liu & Tan (2017)), which in turn exacerbate buckling. Similarly, as airship geometries deform under aerodynamic loads, the resulting changes in shape significantly influence aerodynamic performance (Bessert & Frederich (2005), Liu, Lu & Xue (2008)). These interactions can be modeled by coupling static structural analysis with fluid flow analysis using tools like ANSYS Static, Dynamic, FLUENT, and CFX, or Abaqus and VS Aero. Such setups enable the resolution of nonlinear effects across critical parameters, providing comprehensive insights into performance under combined loading conditions.

While large-volume airships require intricate rigidity considerations, for smaller indoor airships, simplifying the geometry can expedite design and implementation. A pragmatic methodology involves deploying sensors along the airship body to measure strain and record structural changes during operation (Lu, Song, Wang & Huang (2019)). Although limited to specific deflection behaviors during maneuvering, such methods are effective when zones of influence are predefined. However, simulations remain the preferred starting point for structural analysis, allowing robust general tools like ANSYS and Abaqus to determine effects such as bending, buckling, and stress loads. Simulating these effects ensures optimized designs while maintaining structural integrity during dynamic operations.

The studies on wrinkle characterization and static rigidity indicate how structural integrity whether in terms of fabric wrinkling or pressure-induced distortions can substantially affect LTA performance. By merging experimental observation, computational modeling, and sensor-based monitoring, researchers provide an understanding of materials and design decisions that can influence overall reliability. Although significant work addresses wrinkle characterization, rigidity, and pressure effects in large or specialized airship designs, small, non-rigid indoor blimps often lack dedicated research on how structural deformations interplay with low-speed

aerodynamic forces. This emphasis the necessity of an integrated methodology for predicting envelope wrinkling and rigidity requirements under confined indoor conditions. Hence, this thesis incorporates structural analysis findings into a broader parametric design tool that ensures envelope materials and internal pressure levels are optimized for enhanced stability and minimal deformation during flight.

CHAPTER 2

RESEARCH METHODOLOGY

2.1 Research Process

This chapter presents the research methodology employed to evaluate the key parameters relevant to small, non-rigid indoor airships. Drawing on a Design Science Research (DSR) perspective Hevner & Chatterjee (2010), the overall approach integrates both analytical and numerical tools to systematically assess buoyancy, aerodynamic drag, added mass, structural rigidity, and wrinkling behavior. The primary aim is to establish a clear workflow and set of solution strategies that researchers or designers can follow, thereby facilitating the consistent evaluation of multiple shapes under diverse user-defined conditions (e.g., envelope material, payload requirements, and inflation pressure).

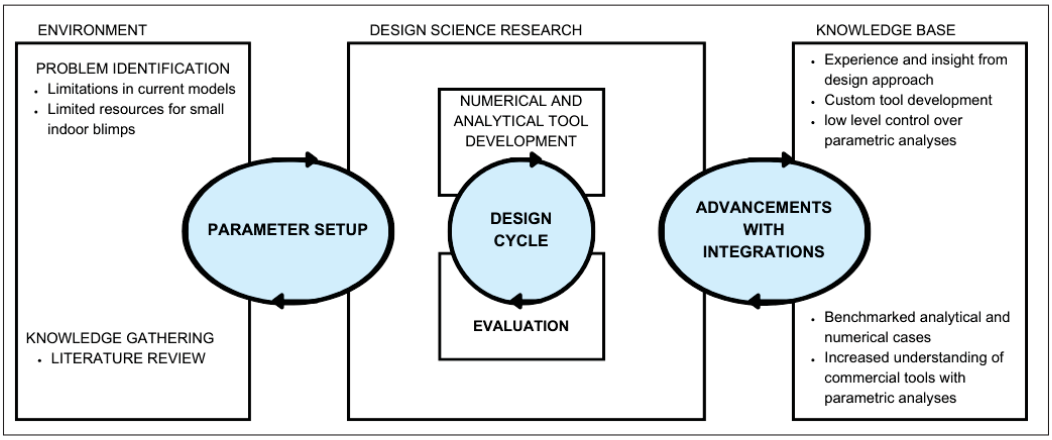

Figure 2.1 Research methodology adapted from Design Science Research (DSR) Hevner & Chatterjee (2010)

2.2 Design Science Research Perspective

The DSR framework emphasizes an iterative cycle of:

1. **Problem Identification:** Recognizing limitations in existing methods for indoor airships, particularly regarding small-scale, non-rigid envelopes.

2. **Knowledge Gathering:** Reviewing relevant literature to extract critical design parameters and technical approaches.
3. **Solution Development:** Creating analytical scripts and leveraging general software to examine each parameter in detail.
4. **Validation and Refinement:** Comparing results with validated references and refining the methods to improve reliability and applicability.

In this work, each parameter is tackled with its own specialized tool (e.g., a Python script for buoyancy or added mass, finite element analysis for structural deformation, and CFD-based approaches for drag). Through careful refinement, each technique is enhanced and tested against reference data. This procedure ensures that the final set of solution tools can handle various shapes and use-case scenarios encountered in small, indoor LTA operations.

2.3 Overview of Shapes and Parameter Tools

In light of the literature review and technical considerations for different envelope designs, four shapes are evaluated:

- **Sphere:** Extensively covered in existing references, it is used for validating fundamental calculations such as buoyancy and for checking analytical or numerical correctness (e.g., drag, added mass, and structural stress) due to its well characterized geometry.
- **Prolate Ellipsoid:** Historically recognized as the classic airship shape, offering a broad base of validation studies (e.g., drag, and added mass) and established aerodynamic estimations.
- **Oblate Ellipsoid:** A common ellipsoidal variant in airship literature, enabling comprehensive cross-comparison of performance and accessible added mass references.
- **Elliptical Cylinder:** A more unconventional geometry chosen to demonstrate the extensibility of the methodology to unconventional aerodynamic shapes, yet geometrically relevant for certain design concepts.

Table 2.1 summarizes these shape selections and the principal reason each is included in this methodology.

Table 2.1 Shapes utilized in the parametric analysis

Shape	Primary Reference Base	Reason for Inclusion
Sphere	Extensive theoretical (classical buoyancy, drag, added mass, stress)	Ideal for validating fundamental computations due to well-established literature and analytical solutions.
Prolate Ellipsoid	Classic airship designs	Represents typical airship geometry. Well documented, facilitating verification of aerodynamic and added mass calculations.
Oblate Ellipsoid	Variant of standard ellipsoid studies	Enables comparison with prolate ellipsoids, ensuring that the methodology can handle different ellipsoidal forms found in literature.
Elliptical Cylinder	Limited direct references (more unconventional)	Tests the methodology with unconventional shapes, demonstrating its extensibility across diverse design concepts.

2.4 Tools and Approaches for Parameter Evaluation

To address the five key parameters (buoyancy, drag, added mass, structural rigidity, and aesthetics), both custom solutions and general software are employed, balancing computational accuracy with practical feasibility.

2.4.1 Buoyancy Analysis

Approach: A custom Python script applies the fundamental principles of Archimedes. Users supply geometry dimensions (e.g., radii, major/minor axes), envelope properties (material

density, thickness) and environmental conditions (ambient temperature, local atmospheric pressure), from which the script computes:

- Enclosed volume and net buoyant force
- Sensitivity to partial inflation and internal pressure variations

Solution Strength:

- Extremely rapid calculation
- Straightforward adaptation for different shapes or advanced gas models (e.g., helium-hydrogen mixes)

Validation: Comparison with known buoyancy data for spheres and ellipsoids, ensuring consistency with classical references and prior airship studies.

2.4.2 Drag Estimation (CFD)

Approach: ANSYS Fluent is selected for aerodynamic modeling:

- Shape geometry is imported or generated parametrically.
- Boundary conditions (low-speed inflow, pressure outlet) replicate indoor flight scenarios.
- Turbulence models (e.g., k-ω) are chosen based on low-to-moderate Reynolds number ranges common in indoor environments.

Solution Strength:

- High-fidelity modeling of flow physics around unconventional geometries.
- Mesh refinement strategies ensure localized accuracy near boundary layers.

Validation: Literature-based drag coefficients for spheres and ellipsoids with any available wind-tunnel or published CFD data. Mesh independence studies further enhance confidence in the results.

2.4.3 Added Mass Computation

Approach: Added mass is crucial in fluid-structure interaction scenarios. Here, a Python-based Boundary Element Method (BEM) with potential flow theory is used:

- Geometry discretized (meshing) into surface panels.
- Influence matrices computed and integrated for an added mass matrix for each shape.

Solution Strength:

- Relatively lower computational cost than full CFD-based transient analysis.
- Direct correlation to classical potential flow solutions.

Validation: Empirical or theoretical references (e.g., sphere test cases, known ellipsoid data) are used to confirm code accuracy.

2.4.4 Structural Rigidity and Wrinkle Analysis

Approach: For non-rigid envelopes under internal pressure, membrane or shell models are built in Abaqus:

- Material properties for typical thin-film fabrics (e.g., polyurethane) are specified.
- Internal cavity pressure simulates inflation; external conditions approximate indoor environments.

A secondary script (in Python) extracts local strain or stress states from Abaqus output to determine potential wrinkling regions.

Solution Strength:

- FEA captures nonlinearities, including large deformations.
- Wrinkle detection methods highlight zones susceptible to structural instability.

Validation: Comparison with published results on fabric wrinkling and membrane structures, along with simpler known cases (e.g., pressurized spheres) to anchor the solutions in recognized benchmarks.

2.5 Parametric Analysis

A central feature of this methodology is a solution package that integrates the above tools into a modular system. End-users can provide:

- **Shape Selection**: Sphere, Ellipsoid (Prolate/Oblate), Elliptical Cylinder, or user-provided geometry.
- **Material Characteristics**: Young's modulus, density, thickness, etc.
- **Operational Conditions**: Payload, internal pressure, ambient temperature, or altitude.

The framework then produces the following outputs:

- Net buoyant force for the specified shape and gas type.
- Estimated drag coefficient at user-defined speeds.
- Added mass coefficients for different axes of motion.
- Envelope stress maps, indicating potential wrinkling zones under internal pressure or minimal aerodynamic loads.

Such a consolidated environment streamlines evaluation, reduces the need for repeated manual setups, and provides a robust foundation for future expansions, such as coupling with refined structural analyses or extended flow simulations.

2.6 Evaluation and Refinement

Following the DSR principles, each tool and approach undergoes:

- **Literature Cross-Checking**: Verifying results with prior studies (where available).
- **Sensitivity Analysis**: Adjusting mesh densities in CFD, boundary conditions, or strain thresholds for wrinkling to confirm stable outcomes.
- **Iterative Updating**: Where discrepancies arise (e.g., under predicting drag or overstating wrinkle extent), the respective scripts or FEA models are refined, ensuring alignment with established reference cases.

CHAPTER 3

THEORETICAL ESTIMATION OF AEROSTATIC FORCES

This chapter examines aerostatic principles essential for defining the geometric characteristics of small non-rigid indoor airships. It specifically addresses buoyancy, and its interconnected parameters that critically influence overall airship design. The chapter begins by examining buoyancy and its implications for airship sizing and geometry.

3.1 Buoyancy

Buoyancy, as described by Archimedes' principle, is the upward force experienced by a body submerged in a fluid, resulting from density differences between the body and its surrounding medium. For airships, buoyancy (also referred to as aerostatic lift) is primarily derived from using lighter-than-air gases, allowing them to achieve a net upward lift force. Figure 3.1 illustrates the key forces acting on an airship, highlighting buoyancy acting upward, gravitational force acting downward, and the internal gas pressure acting radially outward. The buoyancy force B is

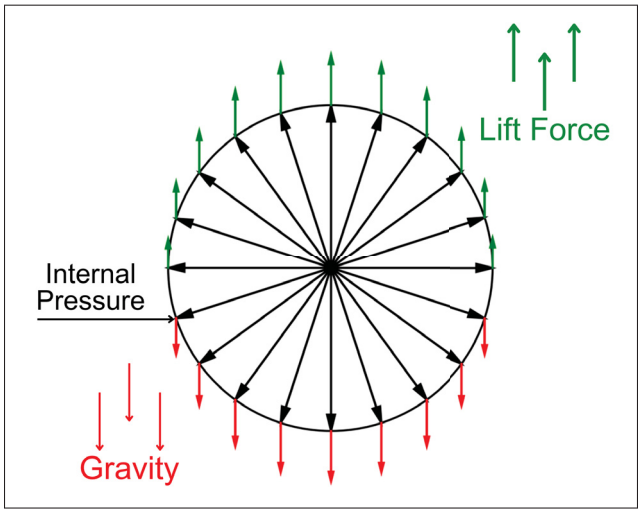

Figure 3.1 Forces acting on a non-rigid airship envelope: buoyancy force (upward), gravitational force (downward), and internal pressure acting radially outward

mathematically expressed as:

$$B = V \cdot \rho_a \tag{3.1}$$

Here, V represents the volume of the airship envelope, and ρ_a denotes the ambient fluid density. The net lift force L experienced by the airship is then determined by subtracting the envelope's weight from the buoyancy force:

$$L = B - W \tag{3.2}$$

where W is the total weight of the envelope.

In the context of our parametric approach outlined in Chapter 2, the primary objective in this chapter is to determine optimal geometric specifications corresponding to a predefined payload. The payload includes the onboard equipment and envelope material. This results in the available disposable lift L_d, which can be defined as:

$$L_d = V(\rho_a - \rho_g) - W_b \tag{3.3}$$

Here, ρ_g is the density of the lifting gas and W_b is the envelope weight. The disposable lift determines airship categories: $L_d < 0$ defines heavier-than-air airship requiring active propulsion for lift, $L_d = 0$ characterizes neutrally buoyant bodies stable at equilibrium, and $L_d > 0$ defines lighter-than-air bodies that inherently possess positive buoyancy. For our case we have determined the basic requirement of disposable lift to be positive therefore expect a inherent positive buoyancy.

3.1.1 Shape Selection and Validation

Four geometric configurations were strategically selected to evaluate aerostatic and aerodynamic performance comprehensively:

- **Sphere:** Selected due to extensive existing literature, making it ideal for numerical and analytical validations.
- **Prolate Ellipsoid:** Widely recognized as the classic airship geometry, offering abundant historical reference data and benchmark solutions.

- **Oblate Ellipsoid:** Chosen as a standard variant of the ellipsoid shape, while not uncommon in airship designs the particular variant was inspired by the existing mini blimps at INIT Lab (Figure 3.2b).
- **Elliptical Cylinder:** A less conventional yet geometrically relevant shape, inspired by the existing Scutigera blimp at INIT Lab (Figure 3.2a), to demonstrate methodology versatility for practical, unconventional designs.

Table 3.1 Geometric dimension ratios of airship envelopes relative to base length (bl)

Geometry	**Dimension Ratios (relative to base length, bl)**
Sphere	$r = 1.0 \times \text{bl}$
Oblate Ellipsoid	$a = b = 0.40 \times \text{bl}, \quad c = 0.25 \times \text{bl}$
Prolate Ellipsoid	$a = 0.40 \times \text{bl}, \quad b = c = 0.25 \times \text{bl}$
Elliptical Cylinder	$a = 0.840 \times \text{bl}, \quad b = 0.375 \times \text{bl}, \quad h = 1.0 \times \text{bl}$

To ensure consistent shape reference and practical design implementation, the concept of a base length is introduced. The base length represents a fundamental flat dimension from which envelope geometries are fabricated. This practical parameter simplifies comparisons across geometries by providing a single reference measurement. This approach facilitates consistent comparison and allows straightforward geometric dimensioning. Specifically, the base length corresponds to the dimension of the initially flat material pieces that, when joined and inflated, form the final three-dimensional envelope shapes used in this study. The dimensional ratios for the oblate and elliptical cylinder geometries were adapted directly from blimp designs present at INIT Lab (Figure 3.2).

Figure 3.3 illustrates the iterative computational strategy developed to calculate buoyancy-derived geometric parameters. Starting from the selected shape, material properties and payload, an iterative calculation begins with an initially small base length, incrementally adjusted until the computed payload aligns with the required payload. For extended material selection, Bradley (1999) outlines several standard membrane materials for airship structures. While MatWeb (2020) provides an extensive source of material properties that can be utilized to gather required input membrane parameters for the study.

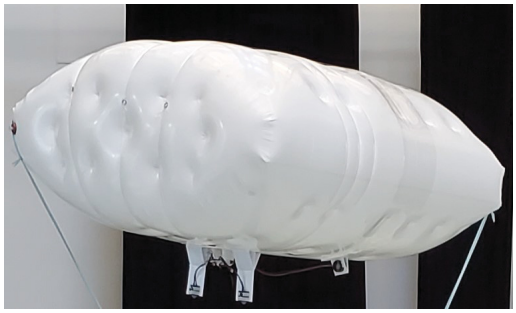

a) Scutigera blimp at INIT Lab

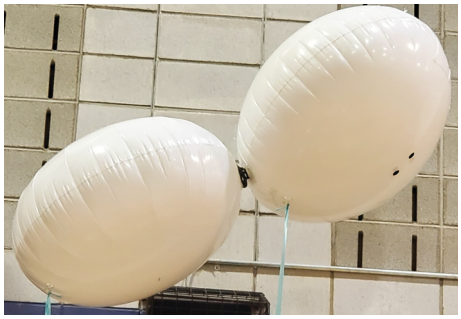

b) Mini blimps at INIT Lab

Figure 3.2 Inflatables used to determine permeability losses

Users can also input their custom geometry in STL format and opt for standard materials conventionally used for airships, such as polyurethane, mylar, polyvinyl fluoride, and polyester. Alternatively, they can input the density of a user-defined material in kg/m^3. Following this, the script provides the required geometry dimensions for a given reference geometry. For the scope of this study, we are designing airships with a disposable mass of 100 grams. Providing $M_{pr} = 0.1Kg$ in the above-mentioned strategy, the dimensions for the required payload mass are presented in Figure 3.4 along with their specific base length.

The payload variations across each geometry's base length and their disposable payload are presented in Figure 3.4. By observing the trajectory, geometry dimensions can be calculated for a disposable payload of up to 100 grams for each shape. As expected, spheres provide the smallest required base length for a specified payload due to their optimal surface area to volume ratio. Elliptical cylinders also show favorable payload capacities due to their elongated dimension, despite their unconventional geometry. Oblate and prolate ellipsoids require progressively larger dimensions for identical payloads, impacting practicality in confined indoor spaces.

The methodology mentioned above is deployed to attain the ideal buoyancy of an airship, along with several additional steps required to enhance the geometry description. Empirical cases often involve related factors contributing to lift generation, which can interact with various local parameters. These factors can reduce the divergence between the ideal case values calculated

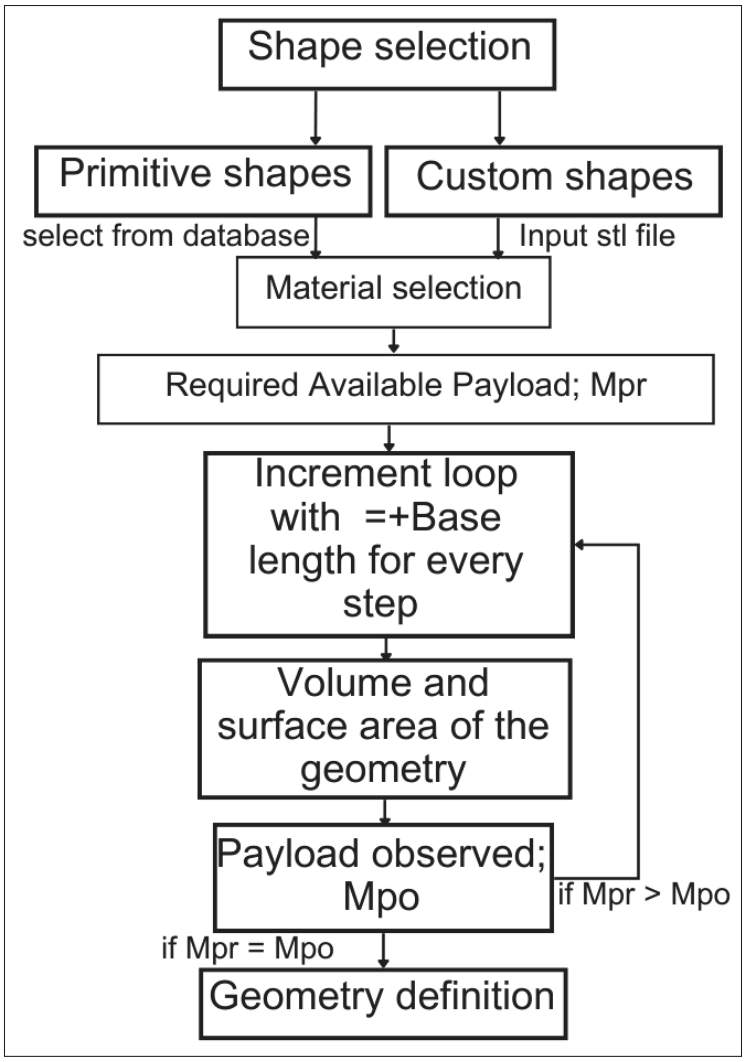

Figure 3.3 Iterative computational flowchart for payload-optimized shape dimensioning based on buoyancy principles

above and those observed in experimental setups. Subsequent sections investigate these factors and propose potential control techniques to mitigate the range of disparity between the calculated and empirical payloads.

3.1.2 Impact of Over Inflation on Buoyancy

Inflatable airships achieve higher buoyancy by utilizing lightweight membrane materials that minimize structural weight while maximizing enclosed lifting gas volume. Consequently,

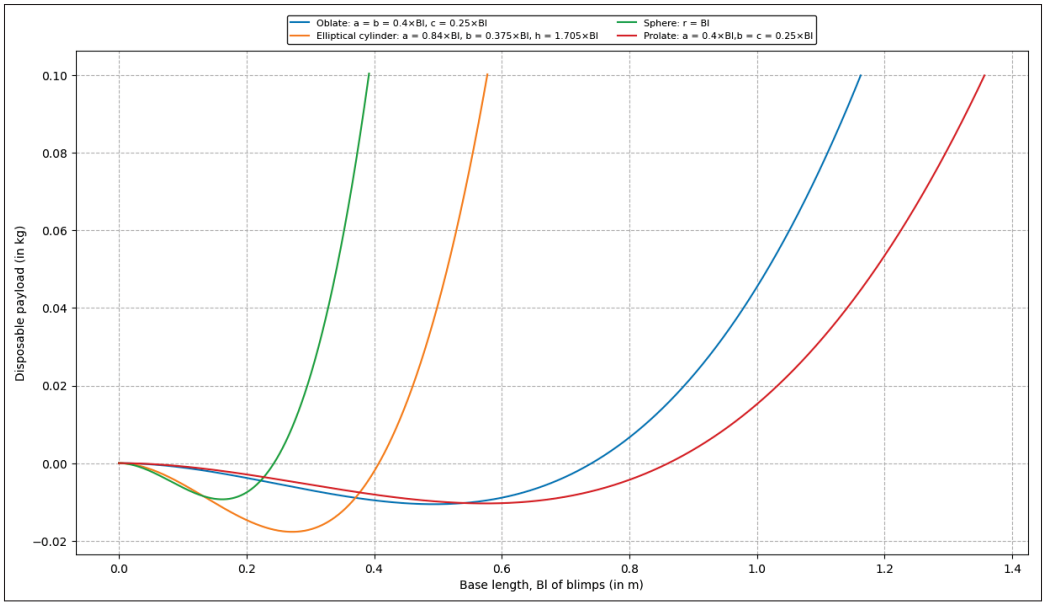

Figure 3.4 Disposable payload versus base length across selected geometries, indicating optimal dimensional ratios for design selection

materials with a high strength-to-density ratio are often preferred for envelope construction. However, most such materials exhibit some degree of elasticity, leading to unintended volume expansion under internal pressure, commonly referred to as over-inflation.

Another crucial aspect of material influence on buoyancy is the stress-strain response of the membrane. Since the internal pressure of the lifting gas is the primary driving force behind inflation in all non rigid airships, the expansion ratio directly correlates with the structural properties of the membrane. Specifically, materials with a lower Young's modulus allow greater expansion, inadvertently increasing both internal volume and overall buoyancy. The necessary parameters required to characterize inflation-induced expansion are discussed in detail in Chapter 6.

Figure 3.5 illustrates both the intended inflation and over-inflation of an elliptical cylinder geometry a shape chosen for demonstration due to its pronounced expansion effects on visual appearance and structural conformity compared to other tested geometries. The additional

payload capacity gained from over-pressurization and the resulting increase in volume for all evaluated shapes is presented in Table 3.2.

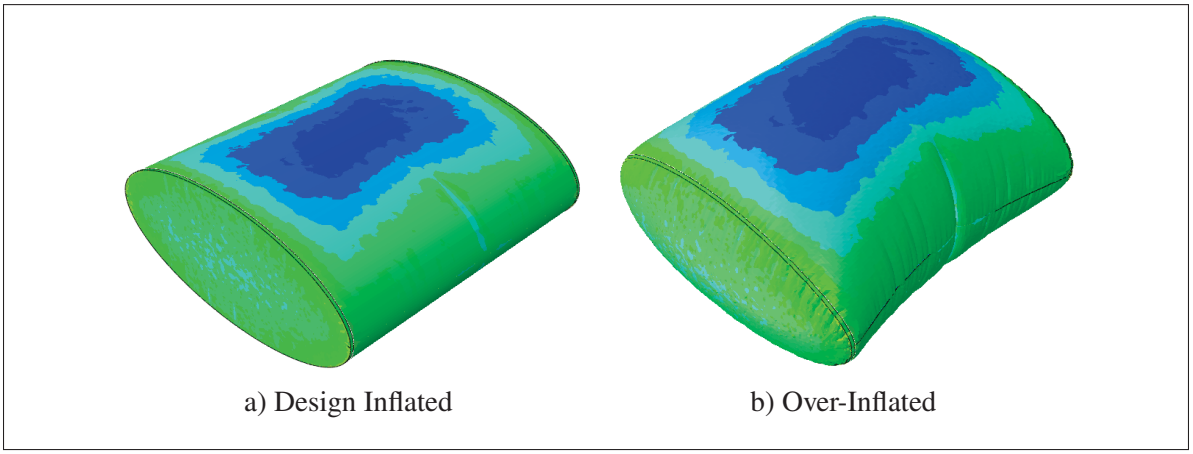

a) Design Inflated b) Over-Inflated

Figure 3.5 Comparison of elliptical cylinder envelope under design inflation and over-inflation

For this section, we use the inflated geometry directly into the buoyancy script as discussed in Figure 3.3 to compute the updated geometry dimensions. These new dimensions are compared against the initial geometry dimension to determine an expansion factor. The corresponding changes in payload volume and surface area for all evaluated shapes are presented in Table 3.2. To incorporate the effects of over-expansion into our buoyancy calculations, we introduce an

Table 3.2 Over-pressured inflatables

Shape	**Original V**	**Original SA**	**Expanded V**	**Expanded SA**	**Added Payload**
Sphere	0.252 m^3	1.93 m^2	0.264 m^3	2.04 m^2	12.55 grams
Oblate	0.263 m^3	2.07 m^2	0.282 m^3	2.16 m^2	20 grams
Prolate	0.261 m^3	2.04 m^2	0.274 m^3	2.22 m^2	13.45 grams
Elliptical Cylinder	0.325 m^3	2.83 m^2	0.429 m^3	3.12 m^2	108.93 grams

expansion factor (α) that represents the user-defined allowable expansion percentage relative to the maximum possible expansion (M_{exp}). This modifies the previous buoyancy equation (Equation 3.3), which is now redefined as:

$$L_d = V \cdot (\rho_a - \rho_h) - M_m + M_{exp} \cdot \alpha \tag{3.4}$$

Here, M_{exp} represents the maximum expansion contribution, derived from inflation measurements, α is a user-defined expansion percentage, determining how much of the maximum expansion is considered in the final buoyancy calculation. For this study, we set $\alpha = 0$, maintaining all airship cases at their desired inflation pressure, preventing unintended over-pressurization. The maximum expansion factors (M_{exp}) for each geometry are provided in Table 3.2. While increasing α may enhance buoyancy and envelope rigidity, excessive over-expansion introduces higher internal stress, risking long-term material degradation. Therefore, selecting an appropriate α value is crucial to optimizing airship lift while maintaining membrane durability.

3.1.3 Membrane Permeability

In examining the adverse effects of inflation on buoyancy, it is crucial to consider the critical factor of permeability, which significantly impacts the reduction in available payload. Permeability, often measured as a flow rate, refers to a material's ability to allow gas flow through its surface. Dense materials may restrict permeability, but gas molecules still diffuse and eventually escape through the inflatable membrane. Understanding permeability is therefore essential to maintain available payload within intended operational parameters. To ensure consistent performance, inflatables must be periodically refilled, as illustrated in Figure 3.6. This cyclic process provides a systematic strategy for actively managing lift loss caused by permeability.

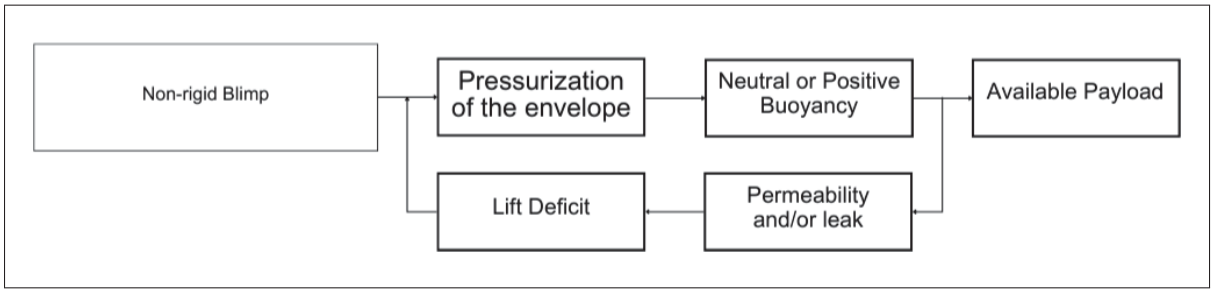

Figure 3.6 Buoyancy cycle of a standard airship

While over inflation increases buoyancy by allowing additional helium, it also leads to an expanded surface area, which stretches the membrane material. This reduces the material's thickness and simultaneously increases internal pressure, leading to higher permeability rates. However, surface area alone does not capture the complete picture. Since payload lift is directly proportional to helium volume, focusing on the relationship between payload loss per hour and volume provides a more unified metric to estimate permeability for different airship geometries.

To accurately quantify permeability-induced payload loss in LTA airships, a controlled experimental setup was designed to evaluate helium leakage through different membrane materials. The test aimed to determine the correlation between payload loss and volume over time, focusing on three commonly used airship materials: Mylar, Thermoplastic Polyurethane (TPU), and Polyurethane (PU) (Figure 3.7).

The experiment was conducted in a controlled indoor environment at a constant temperature of $18 - 23°C$ to minimize variations due to temperature fluctuations. A total of three airships, one for each membrane material, were inflated with helium and suspended in free space using a thin fishing line attached to S-hooks. This ensured that the airships were free from any external forces that might interfere with buoyancy measurements.

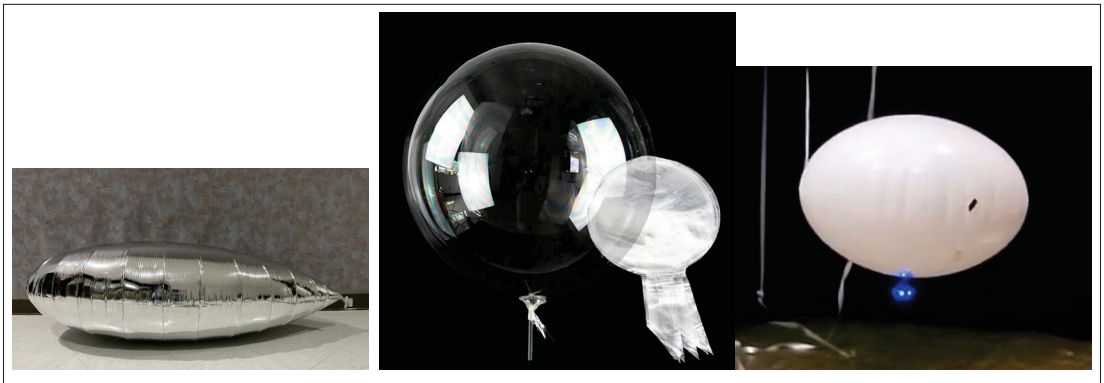

a) Mylar Blimp b) TPU Blimp c) Polyurethane Blimp

Figure 3.7 Three test airships used in the permeability study, fabricated from different materials

The initial payload lift was determined using calibrated weights to establish neutral buoyancy, providing a baseline for measuring helium loss over time. A high-precision scientific scale was used to record weight measurements every two hours, capturing the rate of payload loss due to helium permeability. The collected data was analyzed to establish a correlation between payload loss and airship volume, with a curve-fitting approach used to develop empirical models describing permeability characteristics for each material. To ensure consistency, all tests were conducted under identical environmental conditions, with particular attention to inflation pressure, weighing accuracy, and helium diffusion effects. The final permeability coefficients obtained from the study provide crucial insights for predicting long-term buoyancy loss, optimizing material selection, and refining airship design models.

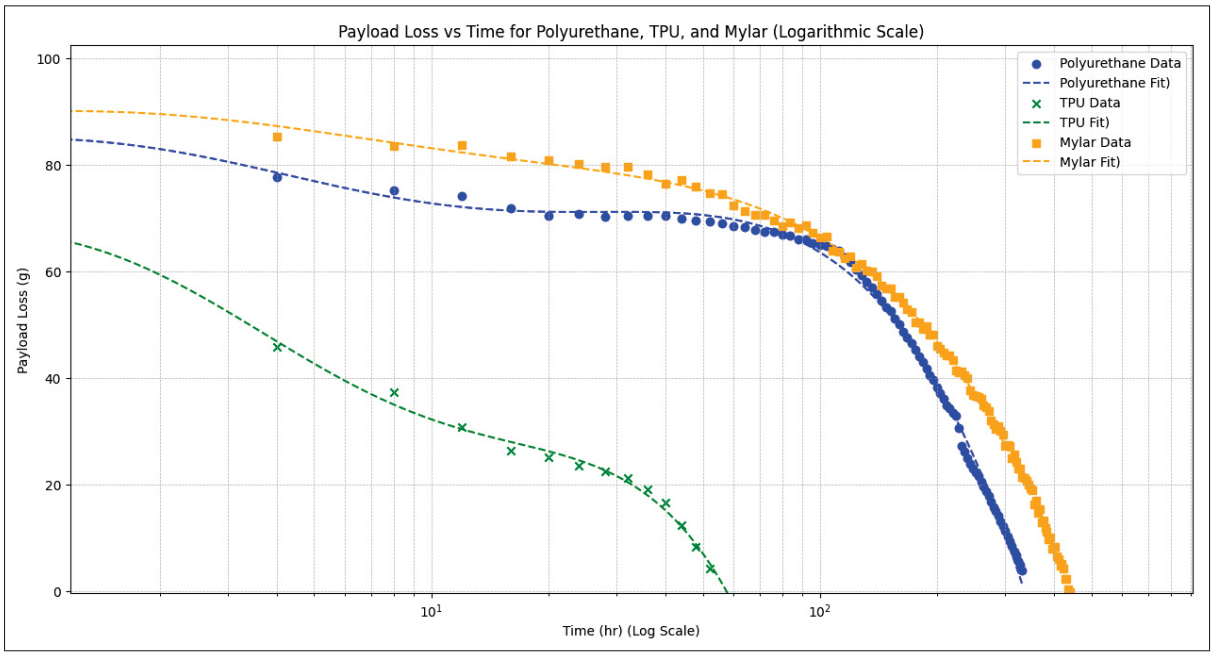

Figure 3.8 Curve-fitted analysis for payload loss(g) vs. time (hr) for different airship materials

To better quantify the relationship between payload loss and volume for different materials, curve fitting was performed for each use cases. Polynomial equations were derived for Polyurethane, Thermoplastic Polyurethane, and Mylar based on their respective data. The resulting equations for payload loss per hour (y) as a function of volume (x) are as follows:

- **Mylar** (Figure 3.9a):

$$y = 30.7x^3 - 18.5x^2 + 3.5x + 0.1 \tag{3.5}$$

- **Thermoplastic polyurethane** (Figure 3.9b):

$$y = 19.4x^3 - 11.2x^2 + 1.6x + 0.2 \tag{3.6}$$

- **Polyurethane** (Figure 3.9c):

$$y = 25.6x^3 - 14.3x^2 + 2.8x + 0.1 \tag{3.7}$$

These equations provide a predictive model for estimating the payload loss rate based on the airship's volume and material. For better visualization, we attach three individual plots in Figure 3.9, illustrating the curve fitting for each material over time.

This study employs a singular curve-fitting methodology based on three predefined curve models to analyze volume-based permeability and predict the operational lifetimes of inflatable airships. With this approach, the user is expected to select one of the three available models, inherently assuming that all membranes exhibit a slightly different response under the tested conditions depending on their material properties. Although this assumption may not capture the full variability in membrane behavior due to excessive external variables like temperature and inlet pressure leakage, the method tries to integrates material-specific characteristics to provide a practical basis for predicting payload losses under empirical conditions.

Table 3.3 Permeability impact on correlation of payload loss and airship volume for polyurethane blimps

Shape	**Volume** (m^3)	**Loss/hour(g)**
Sphere	0.252	0.3072
Oblate	0.263	0.3130
Prolate	0.261	0.3118
Elliptical Cylinder	0.325	0.3784

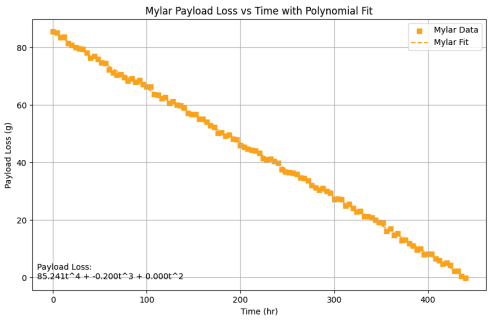

a) Mylar Curve Fit

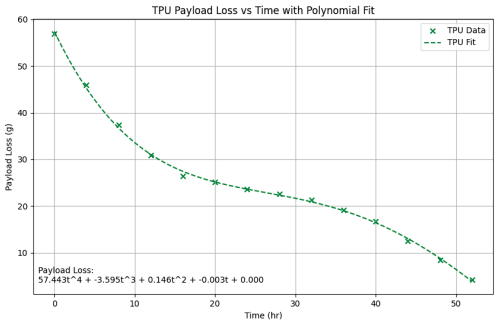

b) TPU Curve Fit

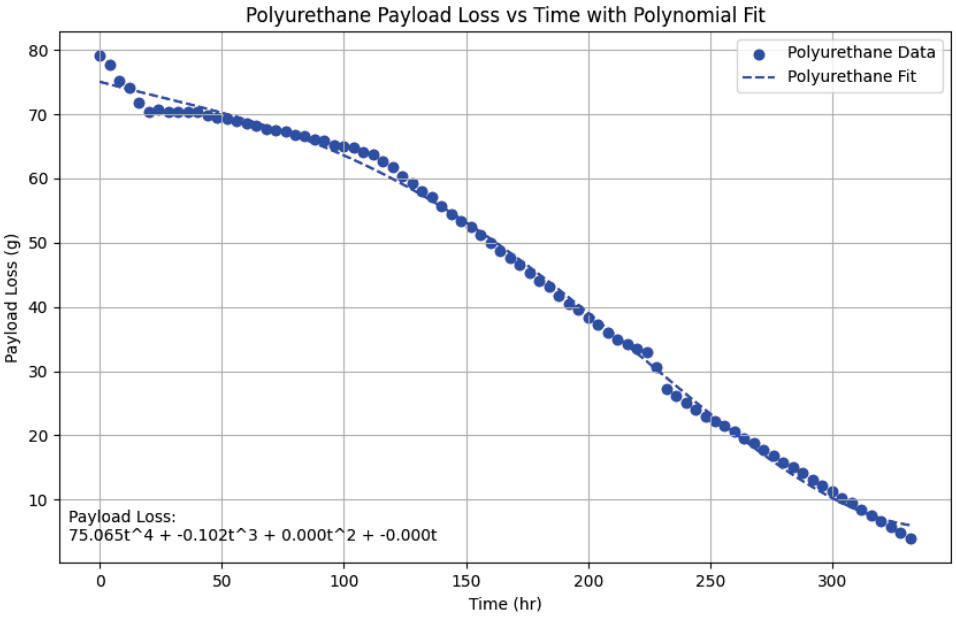

c) Polyurethane Curve Fit

Figure 3.9 Curve fitting analysis of payload loss vs. time for Polyurethane, TPU, and Mylar

The buoyancy life cycle is modeled to incorporate both permeability and temperature effects. By integrating the curve fit equation from the volume-based analysis with the temperature-dependent buoyancy equation, the time-to-deflation for each geometry can be estimated. This provides a comprehensive view of how long an airship can operate with one inflation before requiring refilling.

$$L_d = V \cdot (\rho_a(T) - \rho_h(T)) - M_m + (M_{exp} \cdot \alpha) - (P \cdot \Delta SA) \tag{3.8}$$

Where P is the permeability factor representing the rate of payload loss due to leaks in the inflatable material and ΔSA is the change in the proportional surface area with respect to time due to permeability. The results of the curve fitting backed with experimental observations, are summarized in Table 3.3. The table presents the expected payload loss per hour for each geometry and material type based on its volume.

The correlation between payload loss per hour and volume (Figure 3.8) provides a generalized approach to estimate permeability for other airship geometries. For a given material, the curve-fitted equation can be used to predict the loss rate, which scales directly with the volume. This approach enables designers to anticipate operational lifetimes for airships with varying geometries and materials.

This study highlights the importance of volume-based metrics in understanding permeability. By focusing on the relationship between payload loss per hour and volume, rather than surface area, a unified framework is established to predict permeability for different airship geometries. This method can be extended to include temperature-dependent buoyancy changes, offering a comprehensive solution to managing operational lifetimes for inflatable airships.

CHAPTER 4

CHARACTERIZATION OF AERODYNAMIC FORCES

Fluid dynamics is the study of predicting the motion and behavior of a fluid. At the same time, aerodynamics is the branch of fluid dynamics that focuses on the effects of fluid motion on the body due to their interaction. For aerospace applications, understanding the aerodynamics of a body is crucial, particularly concerning aerodynamic lift and drag effects generated by the flow of the relative wind. The pressure difference over a body, depicted in Figure 4.1, gives rise

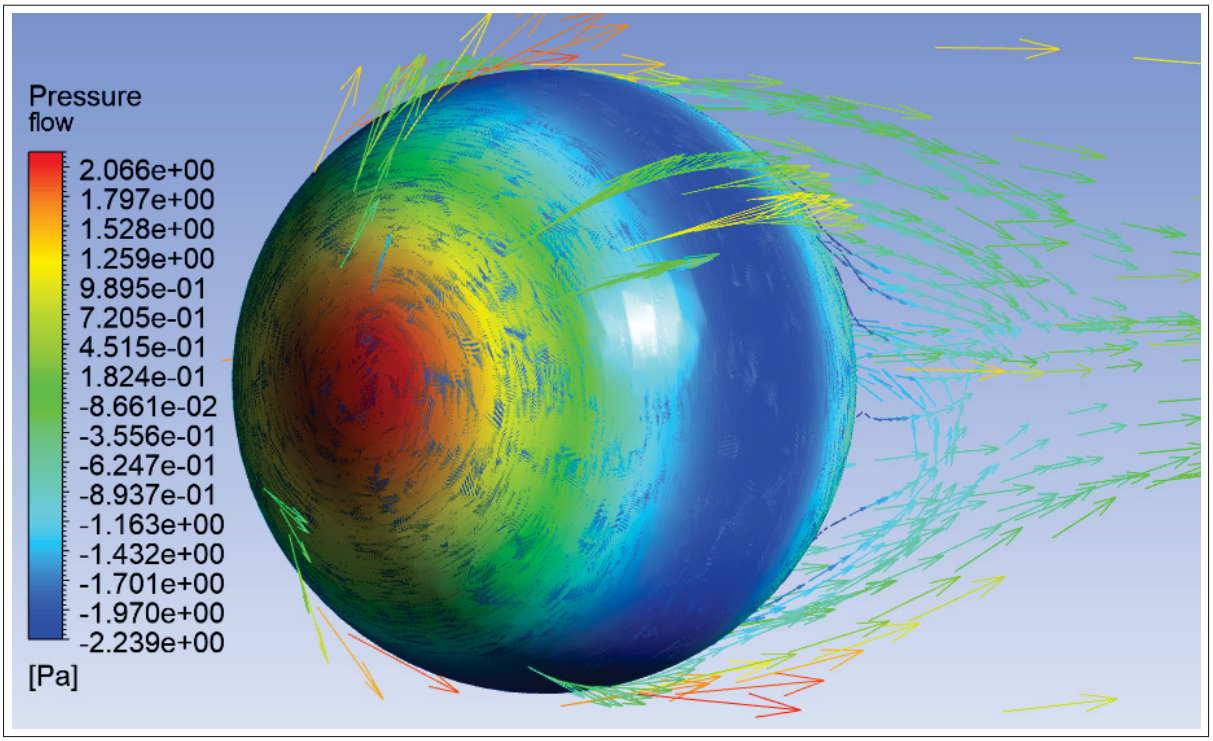

Figure 4.1 Pressure difference observed over the length of a sphere by relative wind at 1 m/s in ANSYS FLUENT

to a disparity between the front edge and the trailing edge of the body. The area where fluid interacts with the body experiences a high-pressure region as the flow of the fluid gets separated along the length of its surface. It observes a low-pressure area, also known as the wake region. The higher-pressure region attempts to move towards the lower-pressure areas to reduce the difference between the pressure along the surface. This variation, in turn, creates momentum between the regions of the body. The perpendicular force generated on the body is known as the

lift force, while the force parallel to the body is called the drag force. Accurately predicting the pressure distribution is crucial in determining aerodynamic lift and drag characteristics.

The body's shape and flow velocity influences lift and drag forces. Hence, several methods have been formulated to define and analyze the specific flow characteristics accurately. Airships, with their large size, are particularly susceptible to the high velocities of the surrounding wind when operating in open environments. Although our focus lies on designing indoor airships operating at lower speeds, the aerodynamic impact of moderate wind velocities is included to enhance the airship's dynamic robustness.

Given the size and velocities of airships, the primary lift observed in their bodies results from the buoyant forces acting upon them. Therefore, our primary focus is determining the drag force and assessing its effects on different shapes for small payload airships.

4.1 Aerodynamic Drag Force

The drag force defined above is an umbrella term for the body's resistance due to its motion in a fluid.

$$D = D_p + D_i \tag{4.1}$$

Which can be further described by Equation 4.1, where D is the drag force generated over the surface of the geometry, D_p is the parasitic drag, which is the drag produced by a body due to the motion of fluid around it. And D_i is the induced drag, which is the drag produced by a body due to its lift.

$$D_p = D_f + D_{int} + D_s \tag{4.2}$$

Equation 4.2 introduces various parasitic drag components, where D_f is the form drag produced due to the body's shape, D_{int} is the interference drag produced due to intersections in the geometry of a body, and D_s is the skin friction drag produced by the body's surface.
Since we are working with symmetric geometries with operations range at low relative wind

velocities, the aerodynamic lift produced by the airships is considered negligible. Therefore, our primary emphasis is parasitic drag as the dominant aerodynamic force acting on the body.

4.1.1 Assessment of Drag Using Computational Fluid Dynamics

The computational workflow in ANSYS FLUENT follows a structured process, ensuring accuracy and efficiency in fluid flow analysis. The process begins in the ANSYS Design Module, where the geometry is defined and prepared for simulation. At this stage, we establish the boundary conditions, specifying key parameters such as inlet, outlet and the extent of the computational domain. Once the geometry and boundary conditions are set up, the model is transferred to the FLUENT Meshing Module, where the element discretization is done. A high-quality mesh is generated, refining critical regions to capture flow variations accurately. To optimize computational efficiency, a grid independence study is often performed to assess the influence

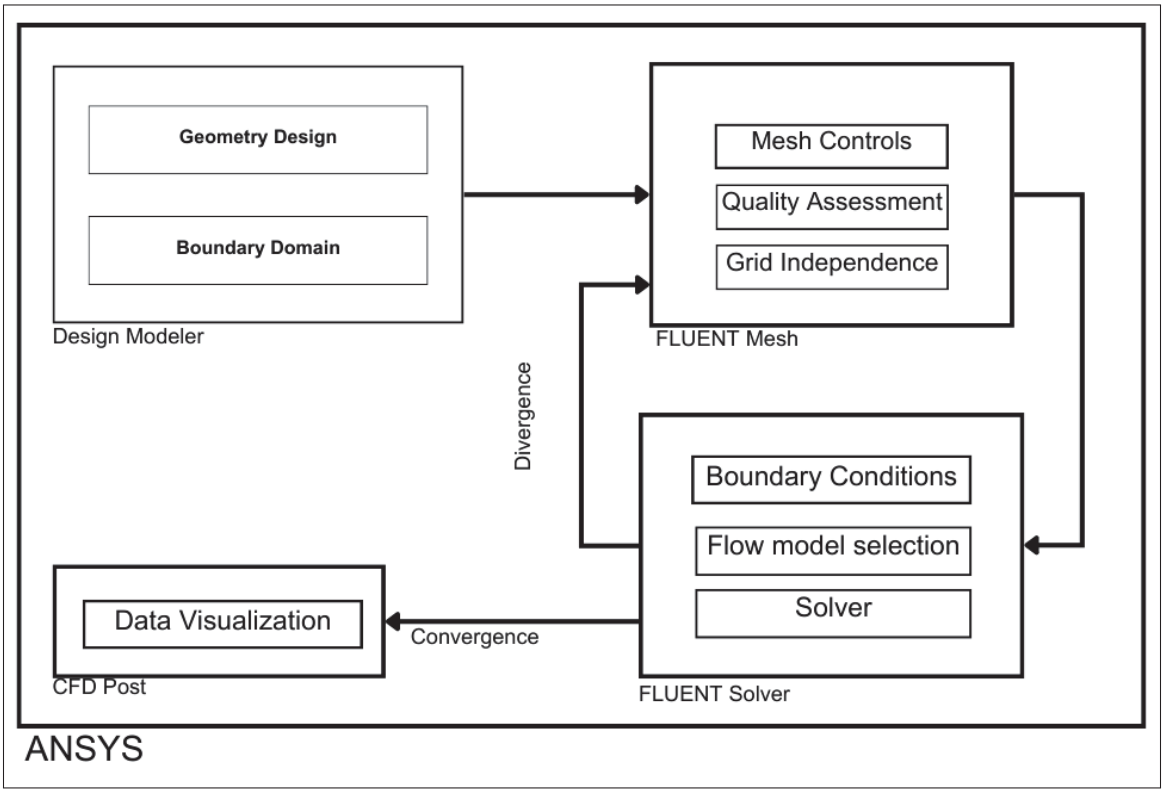

Figure 4.2 Illustrative process chart for predicting drag effects using ANSYS FLUENT

of mesh resolution on the final solution accuracy, ensuring that a lower-element mesh provides results comparable to a finer mesh while significantly reducing computational costs.

With the mesh finalized, the simulation proceeds to the FLUENT Solver Module, where the governing equations are solved under the predefined initial conditions. Here, we configure solver settings such as inlet velocity, outlet conditions, turbulence models, static pressure, and solver discretization schemes to ensure numerical stability and convergence. The solver iterates through the equations until a tolerance threshold is met, ensuring that the fluid dynamics are accurately captured. Once the solution is obtained, the results are transferred to CFD-Post, the post-processing module, where the fluid flow behavior is visualized and analyzed. This stage allows for detailed insights, including pressure distributions, velocity profiles, streamlines, and vorticity contours, which help evaluate the aerodynamic performance and validate the computational model against theoretical or experimental benchmarks. The entire process follows a systematic flowchart illustrated in Figure 4.2

The geometric definitions taken from Figure 3 have been designed using ANSYS Design Modeler Package. To simulate minimal surface friction drag, the blimp geometries are designed to be smooth, ideal membranes free from surface wrinkles or irregularities. Additionally, no supplementary components are attached over the blimps' surface, mitigating the influence of interference drag. Thus, our evaluation of the drag force is primarily attributed to the parasitic drag force.

The design modeler also generates a fluid domain to capture the fluid flow surrounding the geometry. The dimensions of this enclosure are kept proportional to the side length of the designated geometries. Figure 4.3 illustrates the arrangement of the enclosure in relation to the geometries. The geometry domain is designed to effectively capture the impact of fluid-structure interaction. This interaction is configured to ensure that any back pressure from the outlet does not affect the oncoming flow with a relative velocity.

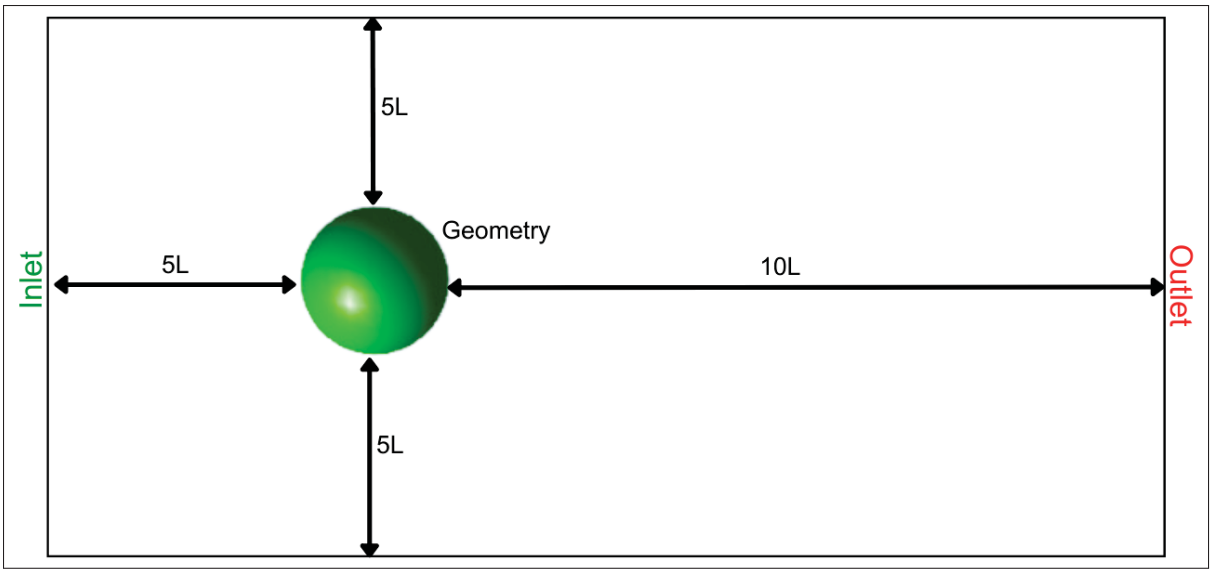

Figure 4.3 Dimensions of the boundary domain generated to simulate fluid flow

4.1.2 Mesh Initialization

The geometry data from the design modeler is then transferred to the FLUENT Mesh package to discretize the geometry into a set of elements and nodes. Two separate meshing approaches simplify the geometry mesh for fluid and solid structures.

- Mesh generation for enclosure domain.
- Mesh generation for the subjected geometry.

The enclosure domain is discretized to accurately capture the complete fluid flow, extending from the inlet to the end of the enclosure, with sufficient density to prevent any adverse reverse flow effects at the outlet. Conversely, a fine mesh grid is employed on the surface of the subject geometries, incorporating a higher mesh quality and an inflation layer to capture boundary layer effects precisely. The mesh accuracy is carefully adjusted to ensure consistent results, irrespective of the enclosure's size and the number of elements.

A grid independence study has been conducted to assess the sensitivity of the aerodynamic drag calculations to mesh quality and determine whether a lower-element mesh can produce results comparable to higher-resolution meshes, thereby reducing computational costs. Three distinct

meshes were generated: Mesh A with 1.5×10^5 elements, Mesh B with 3×10^5 elements, and Mesh C with 4.5×10^5 elements. These meshes vary in element count, inflation layers, and element refinement, which directly impact numerical accuracy. By comparing the results across these different meshes, we validate whether a coarser mesh can achieve equivalent accuracy while significantly reducing computational time, making the methodology more practical for complex geometries.

A consistent boundary condition has been applied to the solution for all shapes across the three mesh qualities. The outcomes obtained from mesh B and mesh C are used as reference benchmarks to assess the performance of mesh A. This comparative analysis aims to illustrate the impact of varying mesh quality on the calculated drag forces for all geometries.

Table 4.1 Mesh metrics generated for selected geometries

Shape	**Element Quality**	**Aspect Ratio**	**Skewness**	**Orthogonality**
Sphere	0.89	1.168	0.188	0.798
Oblate	0.87	1.169	0.186	0.812
Prolate	0.84	1.172	0.188	0.81
Elliptical Cylinder	0.77	1.163	0.199	0.792

Mesh metrics generated from the selected geometries are displayed in Table 4.1, where element quality represents the ability of a finite element to adapt to its geometric criteria. An element quality value of 1 indicates excellent quality, while a value of 0 represents inferior quality. The aspect ratio of the longest edge of an element to its shortest edge. A good aspect ratio closer to 1 is considered excellent, while an aspect ratio around 20 or higher indicates an inferior aspect ratio. Skewness is identified as the distortion in an element's shape. Excellent skewness is near 0, while a skewness value of 1 or higher represents inferior shape distortion. Orthogonal quality evaluates the angles between the edges of an element. Elements with angles closer to 90 degrees are considered excellent with a value of 1, while angles deviating from 90 degrees are inferior and approaching 0.

4.1.3 Defining Fluid Model

The mesh data generated by the FLUENT mesh package is transferred to the FLUENT solver package for further processing. The solver step is crucial in optimizing the model and defining the necessary boundary conditions to accurately predict the drag effects over the body. In our study, we opted to use a pressure-based solver model for its suitability to our research objectives.

We have selected the widely used two-step turbulent flow model realizable k-ϵ to characterize the flow parameters. The selection of this model is based on its ability to satisfy several mathematical criteria on the reynolds stresses, which are coherent with accurate physics models for turbulent flows. The balanced simplicity and the ability to provide accurate solutions based on velocity and length scales alone are due to the two transport equations for the $k - \epsilon$ model presented by Shih, Liou, Shabbir, Yang & Zhu (1995) in Equation 4.3 and Equation 4.4

$$\frac{\partial}{\partial t}(\rho k) + \frac{\partial}{\partial x_j}(\rho k u_j) = \frac{\partial}{\partial x_j}\left[\left(\mu + \frac{\mu t}{\sigma k}\right)\frac{\partial k}{\partial x_j}\right] + G_k + G_b - \rho_\epsilon - Y_M + S_k \tag{4.3}$$

and

$$\frac{\partial}{\partial t}(\rho \epsilon) + \frac{\partial}{\partial x_j}(\rho \epsilon_j) = \frac{\partial}{\partial x_j}\left[\left(\mu + \frac{\mu t}{\sigma \epsilon}\right)\frac{\partial \epsilon}{\partial x_j}\right] + \rho C_1 S_\epsilon - \rho C_2 \frac{\epsilon^2}{k + \sqrt{v\epsilon}} + C_{1\epsilon}\frac{\epsilon}{k} C_{3\epsilon} G_b + S_\epsilon \tag{4.4}$$

Where

$$C_1 = max\left[0.43, \frac{\eta}{\eta + 5}\right], \eta = S\frac{k}{\epsilon}, S = \sqrt{2 S_{ij} S_{ij}} \tag{4.5}$$

The equations mentioned above introduce various parameters, where G_k represents the turbulent kinetic energy induced by mean velocity gradients, G_b is the turbulent kinetic energy originating from buoyancy forces, and Y_M is the contribution of changing dilatation in compressive turbulence to the overall dissipation rate. C_1 and C_2 are constants, and S_k and S_ϵ serve as user-defined

source terms. Meanwhile, the turbulent prandtl numbers for the k and ϵ terms are represented by σ_k and σ_ϵ, respectively.

Regarding the inlet and outlet boundary conditions, the fluid flow's velocity and pressure gradually diminish to zero as they approach the outlet to avoid adverse reverse flow effects. To accurately simulate indoor conditions, wall boundary conditions (No-slip boundary condition) are applied on the lateral faces of the enclosure, where the tangential and normal force and velocity becomes zero as they approach the boundary walls. These boundaries represent physical constraints mimicking as walls or ceilings typically found in indoor environments, where airflow recirculation and confinement can significantly affect drag behavior. This setup ensures the interaction between the airship and the enclosure mimics empirical indoor fluid-structure interactions. Specific consideration is taken to place the walls sufficiently far from the body to avoid artificially increasing drag due to proximity effects, based on recommended best practices for confined flow simulations.

The model incorporates reference values for the geometry's frontal area and side length obtained from Table. 3.1 to determine the drag coefficient accurately. These reference values play a critical role, as the flow model utilizes them to establish an initial estimate. Subsequent correction steps are then executed to refine the initial estimation. Therefore, the accurate setting of these reference values is crucial, as errors in the initial values can lead to substantial discrepancies in the final drag coefficient solution.

4.1.4 Aerodynamic Drag Results for the Selected Geometries

The solution derived from the grid independence study, as illustrated in Figure 4.4, indicates that the variations in the coefficient of drag (C_d) values between mesh A, mesh B, and mesh C remains within an acceptable error margin. As such, the meshing strategy employed for the baseline case is considered robust and is applied across other simulations involving different Reynolds numbers and angles of attack.

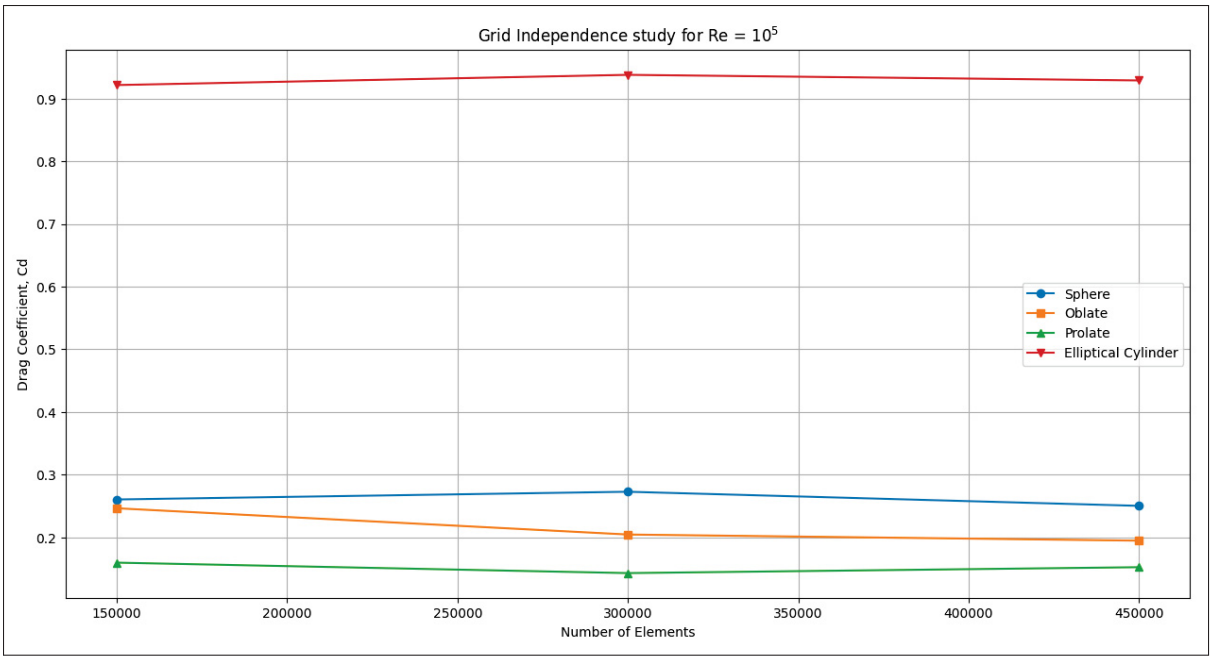

Figure 4.4 Comparative grid independence analysis for different airship geometries

To validate the accuracy of the CFD model, drag coefficient predictions for the sphere are compared against empirical data from established literature. Figure 4.6a presents the computed drag coefficients across a range of Reynolds numbers, defined as:

$$Re = \frac{\rho u L}{\mu} \tag{4.6}$$

Here, u represents the relative wind velocity, L is the characteristic length of the body, ρ is the fluid density, and μ is the dynamic viscosity. For validation, the sphere is used as the benchmark case due to its well-documented aerodynamic behavior. Our simulation range spans Reynolds numbers from 10^2 to 10^5, which reflects to the low-velocity indoor operating conditions desired for small blimp applications. To confirm model reliability, Figure 4.5 illustrates the classical variation of drag coefficient with Reynolds number for a smooth sphere, adapted from White & Xue (2021). Our CFD results for the sphere align well with the empirical trend observed in the laminar and early transitional regions. While a transition toward turbulent boundary layer behavior typically begins near $Re \approx 10^5$, indoor airships operate well below this

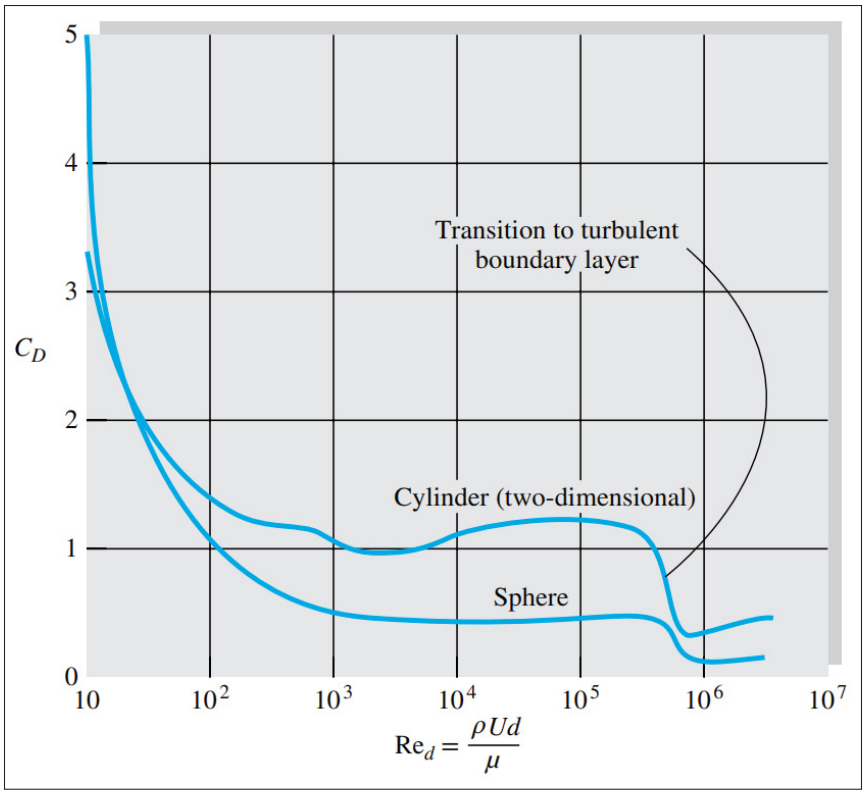

Figure 4.5 Empirical drag coefficient variation with Reynolds number for a smooth sphere, adapted from White & Xue (2021))

threshold. Therefore, it is appropriate to assume laminar flow for the majority of the operational envelope, and the results fall within the expected physical regime. This empirical validation reinforces the credibility of the CFD setup, including the chosen turbulence model, domain configuration, and wall boundary conditions.

The calculation for drag forces based on drag coefficients is determined using Equation 4.7, and the relative wind velocities obtained from the Reynolds number are derived using Equation 4.6. Figure 4.6b showcases the converged drag force solutions across different relative wind velocities.

$$D = \frac{1}{2}\rho V^2 S C_d \tag{4.7}$$

Where D is the required drag force, ρ is density of the surrounding fluid, V is the relative velocity of the subjected fluid, and C_d is the coefficient of drag.

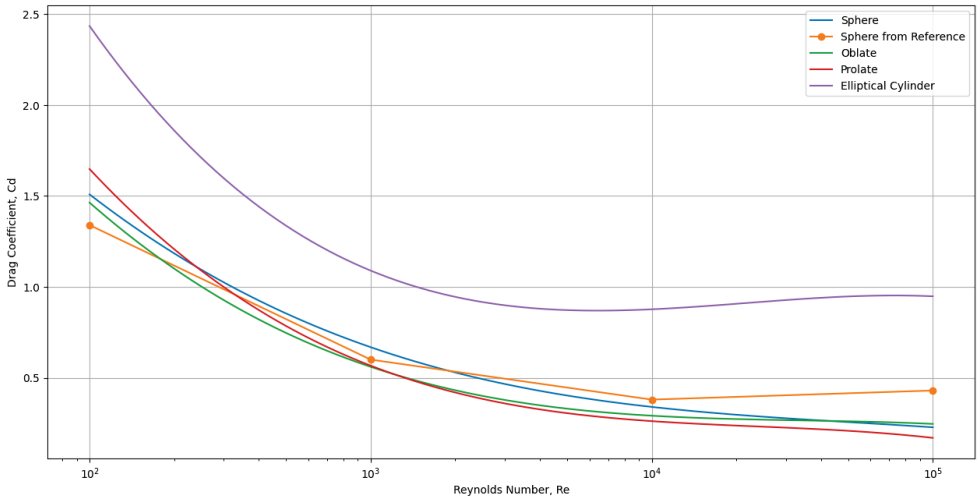

a) Drag coefficient (C_D) vs Reynolds number: CFD predictions compared with empirical values from White & Xue (2021), validating accuracy within the laminar and transitional flow regime

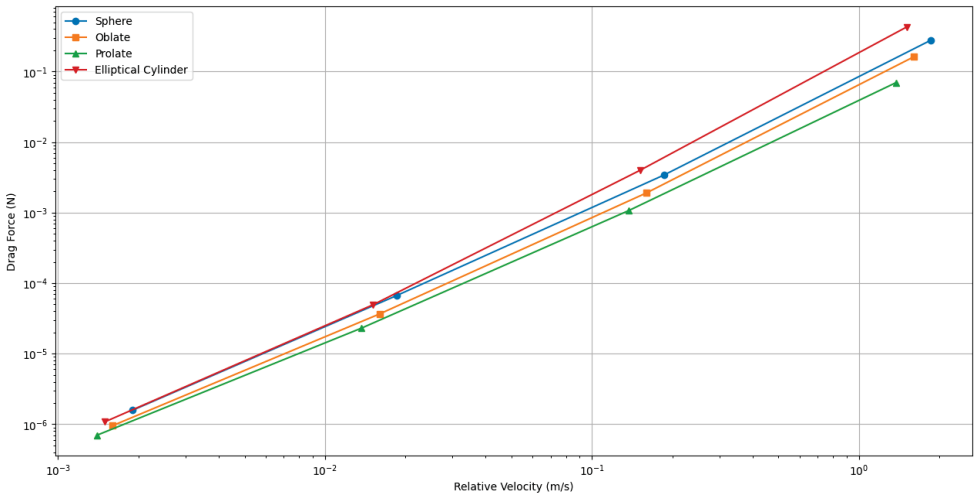

b) Drag Force vs relative wind velocity

Figure 4.6 Drag effects determined for all the shapes

A comprehensive parametric study using ANSYS Workbench is conducted for four distinct geometric shapes sphere, oblate ellipsoid, prolate ellipsoid, and elliptical cylinder to evaluate the drag coefficient across 0°-360° angles of attack. The methodology follows the established analysis framework in ANSYS FLUENT, where different angles of attack are systematically introduced as input boundary conditions. To ensure consistency in evaluation, each shape's

dimensions, reference area, and characteristic parameters are incorporated as input variables within the parametric setup.

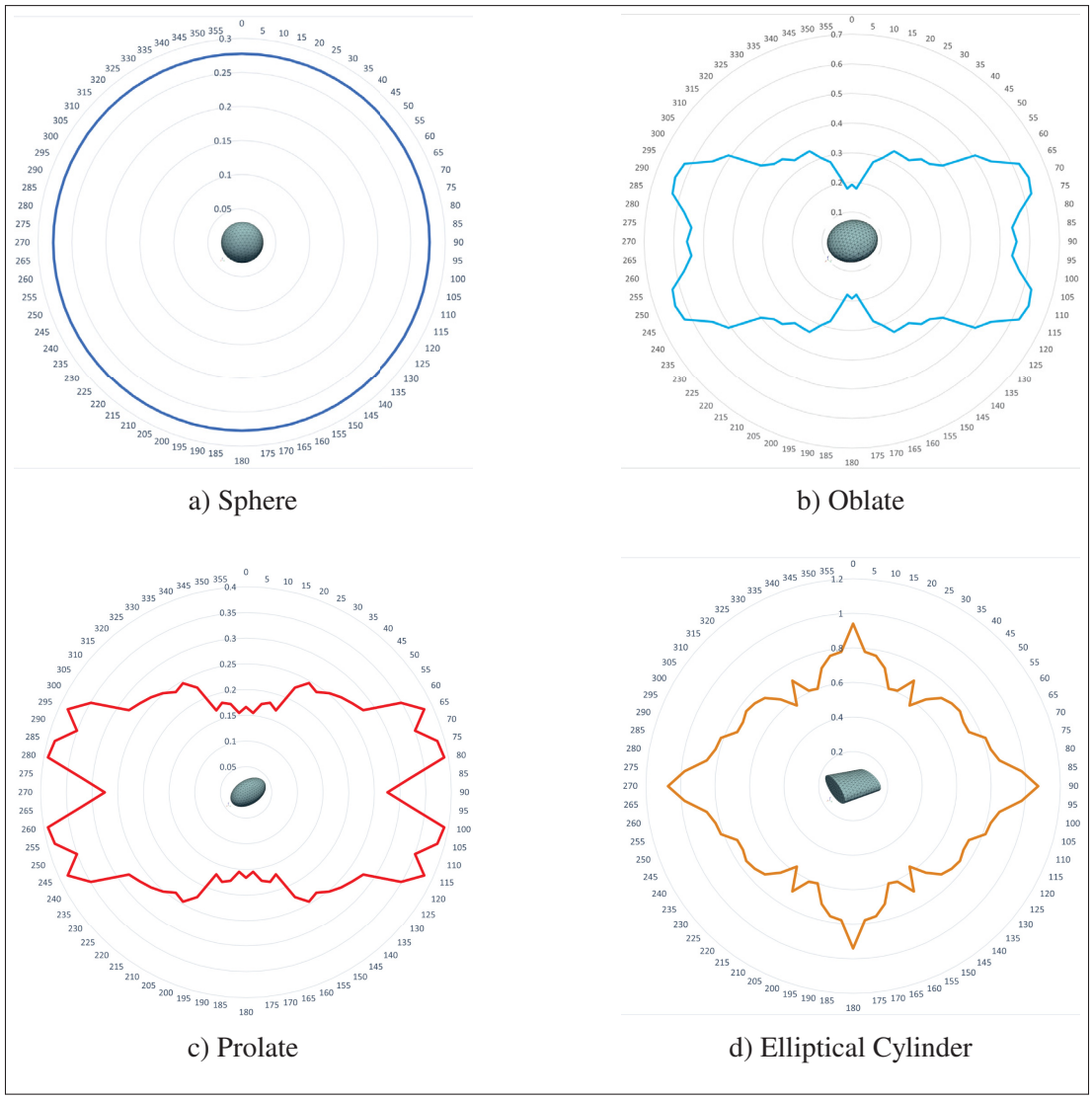

a) Sphere

b) Oblate

c) Prolate

d) Elliptical Cylinder

Figure 4.7 Drag coefficient of studied geometries at varied angles of attack (pitch axis)

For this study, the pitch axis revolution is specifically chosen as the reference frame to calculate drag coefficients, serving as a proof of concept. The selection of the pitch axis allows for a complete rotational evaluation of drag forces, ensuring that the methodology captures variations in aerodynamic behavior at all orientations. While this approach provides a solid foundation for understanding drag characteristics, the model can be further extended by incorporating additional

rotational frames, particularly yaw and roll axes, for oblate, prolate, and elliptical cylinder geometries. Such extensions would enable a more comprehensive aerodynamic characterization, accounting for asymmetries and shape-dependent drag variations, particularly relevant for non-spherical bodies.

The drag coefficients derived from the pitch-axis study are subsequently used to generate polar plots for each shape, illustrating the drag distribution across different angles of attack. These plots provide visual insights into the aerodynamic efficiency of each geometry, demonstrating the applicability of the proposed methodology while paving the way for further refinements in future studies.

CHAPTER 5

ESTIMATION OF ADDED MASS COEFFICIENTS USING BOUNDARY ELEMENT METHOD

Accurately predicting added mass effects is essential for understanding the dynamic behavior of airships, particularly in low-density fluid environments where inertia-driven fluid interactions become significant.While several methodologies exist for evaluating these effects, the Boundary Element Method (BEM) has proven to be one of the most effective numerical approaches. This chapter builds upon the work of Breches (2016) and Carbone *et al.* (2019) by presenting

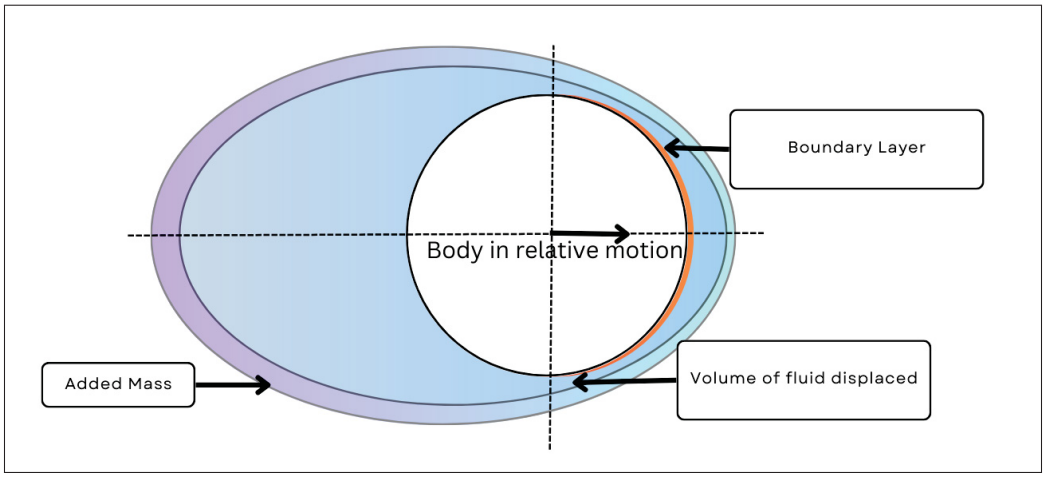

Figure 5.1 Added Mass effect over the surface of the body

an approach that utilizes potential flow theory and adapts BEM formulations to develop a computational tool capable of calculating added mass for any CAD geometry. By leveraging existing numerical methodologies, the tool allows for geometry independent estimation of added mass forces, ensuring applicability across both conventional and unconventional LTA designs. The following sections outline the theoretical foundations of the approach, the implementation of the computational tool, and validation cases for sphere, oblate, prolate and elliptical cylinder that validates the tool's performance against analytical and numerical references.

While Breches' formulation serves as a foundation, this thesis extends and adapts his methodology in the following ways:

- **Generalization for Any CAD Geometry:** Unlike Breches' predefined geometries, our implementation enables added mass computations for arbitrary CAD-based geometries.
- **Tool Development and Automation:** We develop a Python-based computational tool that automates added mass computation by discretizing any user-provided STL geometry into boundary elements.
- **Refined Discretization and Paneling Strategy:** To improve numerical accuracy, our implementation integrates adaptive meshing techniques to balance computational cost with solution precision.
- **Theoretical Foundation and Methodology:** The following sections summarize Breches' key derivations, ensuring clarity for the theoretical foundation, which is then extended toward our developed computational approach.

5.1 Application of Potential Theory to Derive Added Mass Coefficients

For clarity, we recall from Breches (2016) and Carbone *et al.* (2019), the fundamental assumptions made in deriving the added mass coefficients for a body moving in an ideal fluid:

- The flow is steady, irrotational, and inviscid—simplifying the Navier-Stokes equations.
- The fluid is infinite, homogenous, incompressible, and laminar.
- The relative velocity between the body's boundary and the surrounding fluid is zero.
- At infinity, the potential function satisfies: $\nabla\phi \rightarrow 0$ and $\phi \rightarrow 0$.

Under these conditions, the velocity potential ϕ satisfies Laplace's equation:

$$\Delta\phi = 0 \tag{5.1}$$

where Δ is the Laplace operator.

$$\frac{\partial\phi(P)}{\partial n} = \mathrm{v}_p \cdot n \tag{5.2}$$

Where n represents the outward-pointing normal vector from the surface of the body at point P, and v_p is the velocity vector of point P. A fixed frame (XYZ) and a body frame $(O - xyz)$ are

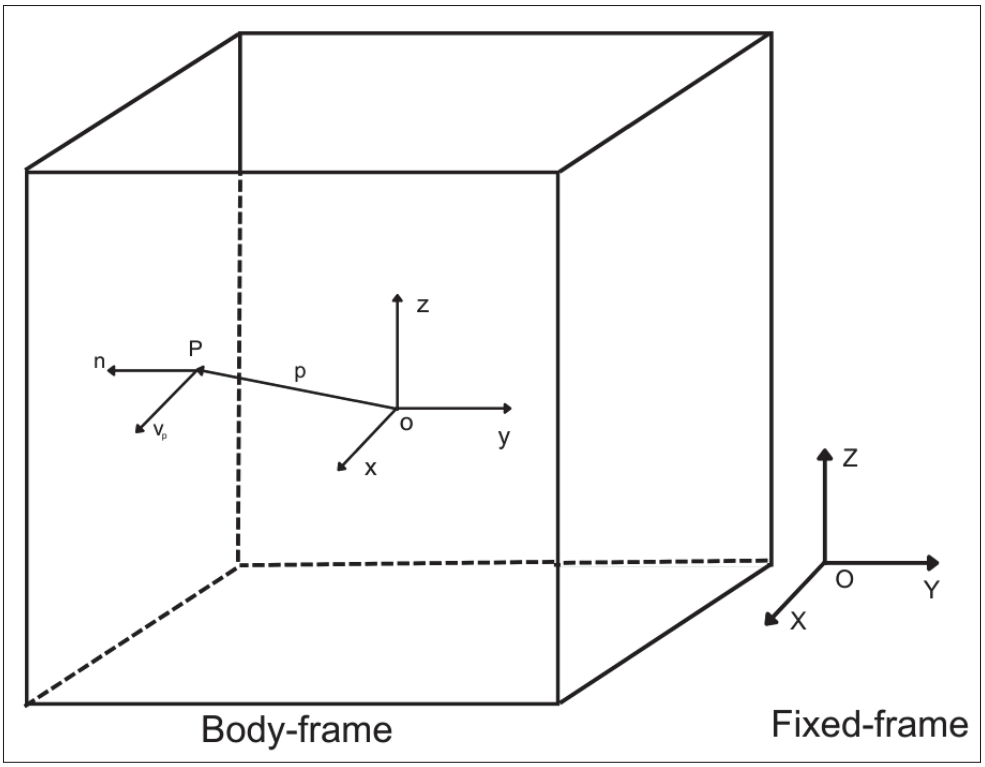

Figure 5.2 Inertial frame of reference for point P on the surface of a geometry

defined to obtain a scalar expression of Equation 5.2. Velocity v_p is further expanded into:

$$\mathrm{v}_p = v + \omega \times p \tag{5.3}$$

Where $\mathrm{v} = [u, v, w]^T$ is the velocity at the origin of the body frame, $\mathrm{p} = [x_p, y_p, z_p]^T$ is the vector position from the origin of the body frame to point P, and $\omega = [p, q, r]^T$ is the vector of angular velocity for the body. Their body frame can be expressed by point P and ω to transform v_p into:

$$\begin{aligned} u_p &= u + (qz_p - rx_p) \\ v_p &= v + (rx_p - pz_p) \\ w_p &= w + (py_p - qx_p) \end{aligned} \tag{5.4}$$

Taking n in its body frame components, Equation 5.2 can be rearranged as:

$$\frac{\partial \phi(P)}{\partial n} = x_n u + y_n v + z_n w + p(z_n y_p - z_n x_p) + q(x_n z_p - z_n x_p) + r(y_n x_p - x_n x_p) \tag{5.5}$$

Here, $x_n, y_n, z_n, x_p, y_p, z_p$ depend on the body's geometry. Furthermore, $u, v, w, p, q, andr$ represent the body's motion and dynamics of the fluid flow. phi can also be represented as:

$$\phi = u\phi_1 + v\phi_2 + w\phi_3 + p\phi_4 + q\phi_5 + r\phi_6 \tag{5.6}$$

Where $\phi_1, \ldots, \phi_6$ are the potential flows of the body. Assuming ϕ_i's to be independent as shown by Korotkin (2009). The equations derived by simplifying the initial assumptions can be written as:

$$\phi_i = 0 \tag{5.7}$$

and,

$$\frac{\partial \phi_i(P)}{\partial n} = \zeta_i \tag{5.8}$$

Where, the respective coefficient ζ_i can be written as:

Table 5.1 Values of coefficient ζ_i^k

i	**1**	**2**	**3**	**4**	**5**	**6**
ζ_i^k	x_n	y_n	z_n	$z_n y_p - z_n x_p$	$x_n z_p - z_n x_p$	$x_n y_p - x_p y_n$

The Equations 5.1 and 5.2 are numerically transformed using the following equation presented by Morino (1974):

$$2\pi\phi_i(Q) = -\iint_S \frac{\partial \phi(P)}{\partial n} \frac{1}{d(P,Q)} ds + \iint_S \phi_i(P) \frac{\partial}{\partial n} \left(\frac{1}{d(P,Q)} \right) ds \tag{5.9}$$

Where P is the integral variable, S is the surface area of the body, Q is a point on the surface area S, $\phi_i(P)$ and $\phi_i(Q)$ are the ϕ_i calculated at point P, and $d(P,Q)$ is the euclidean distance between P and Q.

By following the link between added mass and potential flow from Morino (1974), The kinetic energy of the fluid moved by the body is derived such as:

$$T = -\frac{1}{2}\rho \iint_S \phi \frac{\partial \phi}{\partial n} ds \tag{5.10}$$

Substituting Equation 5.6 in the above equation, the kinetic energy can be changed in a finite double summation:

$$T = -\frac{1}{2}\sum_{i=1}^{6}\sum_{j=1}^{6} \lambda_{ij} u_i u_j \tag{5.11}$$

Where, $u = u_1, v = u_2, w = u_3, p = u_4, q = u_5, r = u_6$ and the equation for added mass coefficient can be written as:

$$\lambda_{ij} = -\rho \iint_S \phi_i \frac{\partial \phi_j}{\partial \mathbf{n}} ds, (i, j) \in [1, \ldots, 6]^2 \tag{5.12}$$

The terms obtained for λ_{ij} are called the added masses of the body. The added mass coefficients can be calculated with the mass matrix of the body with the following:

$$K_{ij} = \frac{\lambda_{ij}}{m_{ij}} \tag{5.13}$$

Where,

$$K_{ij} = \begin{cases} 0, & \text{for } m_{ij} = 0, (i, j) \in [1, \ldots, 6]^2 \\ \frac{\lambda_{ij}}{m_{ij}}, & \text{for all the other cases.} \end{cases} \tag{5.14}$$

5.2 Application of BEM for calculation of Added Mass Coefficients

Following the methodology outlined by Breches (2016) and Carbone *et al.* (2019), Equation 5.14 presents a numerical formulation for computing added mass coefficients, converting the numerical solutions to an analytical implementation. Figure 5.3 showcases a linear cube geometry. Where:

- p_k is the center of the k^{th} element.

- n_k is the normal unit vector of the k^{th} element pointing away from the surface of the body.
- n_e is the number of elements in the geometry.
- ϕ_i^k is the potential flow calculated at the k^{th} element; i = [1,. . . ,6], k = [1,...n_e].
- S_k is the surface area of the k^{th} element.
- $[O - X, Y, Z]$ is body fixed frame for origin O.

By utilizing the above notations in Equation 5.9, the new discretized formula is written as:

$$2\pi\phi_i^k = -\sum_{l=1}^{n_e} B_{kl}\frac{\partial\phi_i^l}{\partial n_l} + \sum_{l=1}^{n_e} C_{kl}\phi_i^l, (k,i) \in [1,\ldots,n_e] \times [1,\ldots,6] \tag{5.15}$$

Equation 5.15 can also be represented in matrix form as:

$$2\pi\mathbf{I}_{ne}[\phi_i] = -\mathbf{B}\left[\frac{\partial\phi_i}{\partial\mathbf{n}}\right] + \mathbf{C}[\phi_i], i \in [1,\ldots,6] \tag{5.16}$$

Where, $[\phi_i^l]$ and $\left[\frac{\partial\phi_i^l}{\partial\mathbf{n}_l}\right]$ are the components of the potential flow for $l \in [1,\ldots,n_e]$, and the values for $\left[\frac{\partial\phi_i^l}{\partial\mathbf{n}_l}\right]$ are taken from Table 5.1. The quantities of matrices **B** and **C** become:

$$B_{kl} = \iint_{S_l} \frac{1}{d(P,P_k)} ds \tag{5.17}$$

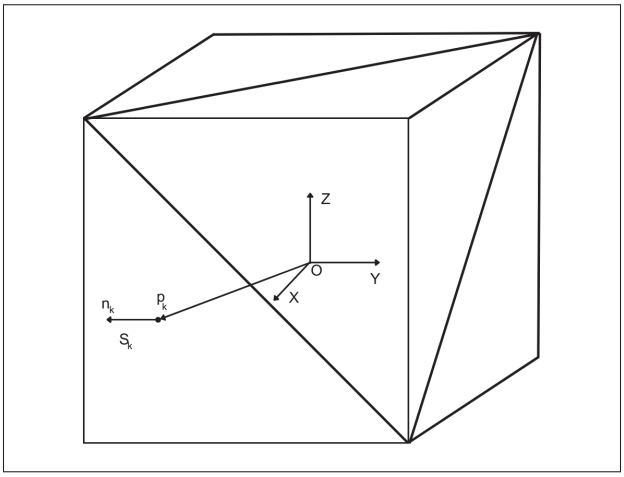

Figure 5.3 Discretization of linear geometry in triangular elements

$$C_{kl} = \iint_{S_l} \frac{\partial}{\partial \mathbf{n}} \left(\frac{1}{d(P, P_k)} \right) ds \tag{5.18}$$

To solve for the potential flow on surface Equation 5.16 can be rearranged as:

$$[\phi_i] = -(2\pi \mathbf{I}_{np} - \mathbf{C})^{-1} \mathbf{B} \left[\frac{\partial \phi_i}{\partial \mathbf{n}} \right], i \in [1, \ldots, 6] \tag{5.19}$$

and substituting Equation 5.19 in Equation 5.12, the newly defined terms for added mass coefficients are:

$$\lambda_{ij} = -\rho \sum_{k=1}^{n_e} \phi_i^k \frac{\partial \phi_j^k}{\partial n_k} S_k, (i, j) \in [1, ..., 6]^2 \tag{5.20}$$

5.2.1 Subdividing Elements for Singularity Prevention

As the geometry is discretized into k elements, the entries of the influence matrices B_{kl} and C_{kl} in the added mass formulation become integrals of the form:

$$B_{kl} = \int_{T_l} \frac{1}{d(\mathbf{P}_l, \mathbf{P}_k)} \, dA, \tag{5.21}$$

$$C_{kl} = -\int_{T_l} \frac{(\mathbf{P}_l - \mathbf{P}_k) \cdot \mathbf{n}_l}{\|\mathbf{P}_l - \mathbf{P}_k\|^3} \, dA, \tag{5.22}$$

where $\mathbf{P}_l$ and $\mathbf{P}_k$ denote points on the source element l and relative element k triangles, respectively, and $\mathbf{n}_l$ is the unit normal of the source element l. A singularity occurs in the process $d(\mathbf{P}_l, \mathbf{P}_k)$ when $\mathbf{P}_l = \mathbf{P}_k$, making the distance approach zero. To avoid numerical instability and to capture the near-singular behavior accurately, further subdivision or specialized quadrature methods are commonly applied.

5.2.2 Singularity Avoidance by Subdivision

Subdivision refers to the process of dividing a geometric element into smaller, simpler elements typically triangles or quadrilaterals for use in numerical methods such as the finite element or finite volume method. The idea is to create elements with nearly uniform shape and size to

minimize numerical errors and enhance simulation stability. In structured meshing, the elements are often transformed into a simpler parametric grid where vertices can be easily generated and later mapped back to the original geometry. A similar reference in grid generation is provided by Thompson, Warsi & Mastin (1985). Their work provides a comprehensive foundation for generating curvilinear grids using coordinate transformations. In particular, they describe the mapping of an annular region defined by two concentric circles onto a unit square. This transformation is key to enabling structured discretization in polar coordinates.

Consider an annular region in the physical space with polar coordinates (r, θ), where the radial coordinate r ranges between r_1 and r_2 and the angular coordinate θ spans $(0, 2\pi)$. The transformation to Cartesian coordinates is given by:

$$x = r\cos\theta, \quad y = r\sin\theta. \tag{5.23}$$

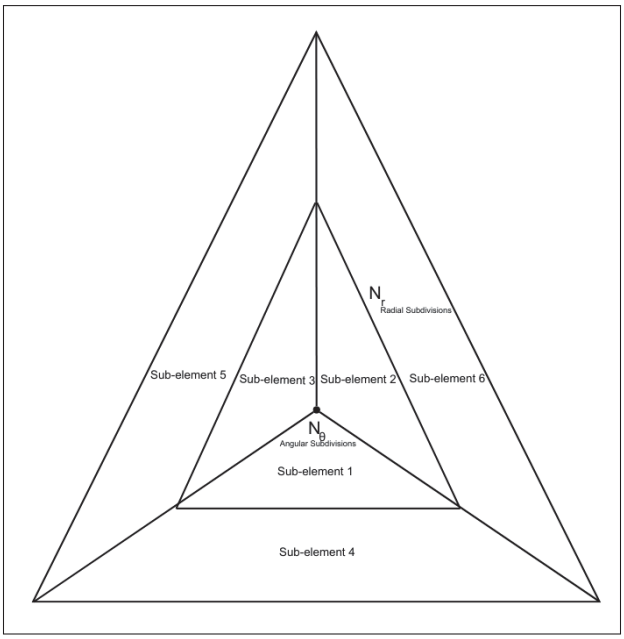

Figure 5.4 Discretization of linear geometry in angular and radial geometry

To facilitate a structured mesh, the radial coordinate is normalized as follows:

$$\xi = \frac{r - r_1}{r_2 - r_1}, \quad \xi \in [0, 1], \tag{5.24}$$

and the angular coordinate is similarly normalized:

$$\eta = \frac{\theta}{2\pi}, \quad \eta \in [0, 1]. \tag{5.25}$$

Thus, the annular region is mapped onto the unit square $[0, 1] \times [0, 1]$. The inverse mapping, which recovers the physical coordinates, is:

$$\begin{aligned} &r = r_1 + \xi(r_2 - r_1), \quad \theta = 2\pi\,\eta, \\ &x = \Big[r_1 + \xi(r_2 - r_1)\Big]\cos(2\pi\eta), \quad y = \Big[r_1 + \xi(r_2 - r_1)\Big]\sin(2\pi\eta). \end{aligned} \tag{5.26}$$

In practical mesh generation, each unit is discretized by dividing the ξ (radial) direction into n_r segments and the η (angular) direction into n_θ segments as described in Figure 5.4. Each grid cell in the unit is then mapped to the physical space using the inverse transformation above.

This discretization typically results in:

- **Central Fan Elements:** Near $\xi = 0$ (or the inner boundary), a fan of triangles is created by connecting the central point to the points on the first concentric ring.
- **Annular Rings:** For $0 < \xi \leq 1$, the grid cells form quadrilaterals. These quadrilaterals can be subdivided into two triangles if a fully triangular mesh is desired.

5.2.3 Gaussian Quadrature for Triangular Integration: The Dunavant Rules

In many fluid mechanics applications especially in the context of potential flow and added mass calculations with our approach, it is necessary to calculate inter element influence efficiently. Another method to evaluate them is to evaluate integrals over triangular domains with high accuracy. Traditional subdivision methods can be straightforward but may require an excessive number of sub-elements for acceptable accuracy. In contrast, gaussian quadrature provides an

efficient means to approximate such integrals by exactly integrating polynomials up to a certain degree with a small number of strategically chosen points. For triangles, one of the most widely used sets of quadrature rules is the family developed by Dunavant Dunavant (1985).

5.2.3.1 Overview of Gaussian Quadrature in Triangles

Gaussian quadrature approximates an integral of a function $f(x, y)$ over a domain Ω by a weighted sum:

$$\int_{\Omega} f(x, y)\, dA \approx \text{Area}(\Omega) \sum_{i=1}^{N} w_i\, f(P_i), \tag{5.27}$$

where P_i are the quadrature points and w_i are the corresponding weights. In the case of a triangle, it is customary to express the points in barycentric coordinates. For a triangle with vertices A, B, and C, any point P inside the triangle can be written as

$$P = \lambda_1 A + \lambda_2 B + \lambda_3 C, \quad \lambda_1 + \lambda_2 + \lambda_3 = 1, \quad \lambda_i \geq 0. \tag{5.28}$$

The use of barycentrics naturally adapts the quadrature points to any triangle regardless of its shape or orientation.

5.2.3.2 Dunavant Rules: Derivation and Properties

Dunavant's quadrature rules are derived by enforcing exactness of the quadrature formula for all polynomials up to a given degree. In practice, this is achieved by:

1. Expressing the integral over the triangle in barycentric coordinates.
2. Setting up the *moment equations* so that for each monomial $\lambda_1^a \lambda_2^b \lambda_3^c$ with $a + b + c \leq p$, the following equality holds:

$$\int_{T} \lambda_1^a \lambda_2^b \lambda_3^c\, dA = \text{Area}(T) \sum_{i=1}^{N} w_i\, \lambda_{1,i}^a \lambda_{2,i}^b \lambda_{3,i}^c. \tag{5.29}$$

3. Imposing symmetry constraints. Since a triangle is symmetric under any permutation of its vertices, quadrature points are chosen in symmetric (cyclic or fully symmetric) configurations. This greatly reduces the number of independent unknowns.
4. Solving the resulting nonlinear system under the constraint that the weights w_i remain positive. The positivity condition is essential for numerical stability.

The outcome is a set of quadrature rules with specific numbers of points (N) that are optimal in the sense that they integrate all polynomials up to degree p exactly. Dunavant's original work presents rules for $p = 1, 2, 3, 4, 5, 6, 7, 8, 9, \ldots$ which, in practical usage, correspond to the following common configurations: 1-, 3-, 4-, 6-, 7-, 12-, 13-, 16-, 19-, 25-, 37-, and 64-point rules. The existence of a rule with a particular number of points is not arbitrary, the nonlinear system combined with the symmetry and positivity constraints has solutions only for specific numbers of points. Therefore we only utilize configurations 1, 3 and 12 for our application with the added mass calculations to verify the accuracy at low to intermediate rules with respect to computational cost.

5.2.3.3 Application of Dunavant Rules for Added Mass Calculations

In our script, we employ the Dunavant rules to evaluate integrals over the surfaces of triangular elements. The integrals are used to compute influence coefficients that form the C and B matrices in the boundary integral formulation for potential flow. Specifically, we compute:

$$C_{ij} = -\int_{T_j} \frac{r(P) \cdot n_j}{\|r(P)\|^3}\, dA, \tag{5.30}$$

$$B_{ij} = \int_{T_j} \frac{1}{\|r(P)\|}\, dA, \tag{5.31}$$

where $r(P)$ is the vector from the centroid of the field (or main) element i to a point P in the source (or interacting) element j, and n_j is the unit normal of element j.

Using Dunavant's rules, the integration in Equations (5.30) and (5.31) is approximated by:

$$\int_{T_j} f(P)\, dA \approx \text{Area}(T_j) \sum_{k=1}^{N} w_k\, f(P_k), \tag{5.32}$$

with the points P_k given in barycentric coordinates and then converted to Cartesian coordinates according to the vertices of triangle T_j. This approach allows us to calculate the entries of the influence matrices accurately without resorting to finer subdivisions of the triangle.

After assembling the C and B matrices from these integrals, we solve the resulting linear system for the potential ϕ and subsequently compute the added mass coefficients. The high degree of accuracy provided by the Dunavant rules is critical in ensuring that the added mass (a sensitive quantity in potential flow problems) is computed reliably.

From obtaining necessary data from the mesh geometry file to evaluating the added mass coefficient, the entire process is represented in Figure 5.5 and will be collectively represented as the added mass algorithm for further applications.

5.3 Integrating BEM for Added Mass with Python

This section presents the implementation of the BEM solution for calculating added mass coefficients. A python-based algorithm is developed as a versatile tool to accurately estimate the added mass coefficients for custom geometries. Figure 5.5 illustrates the planned approach for the algorithm, along with the Python dependencies and their operational requirements. A tolerance-based error step is introduced to ensure accurate estimations in cases where satisfactory mesh quality cannot be achieved.

The geometries have been generated using 2D triangle elements in HYPERWORK's HYPERMESH. Although any arbitrary software such as blender can be used to create the geometry files. Critical parameters like aspect ratios and uniform surface area of all elements are filtered against a modified tolerance, and error-adjusted values are utilized as the final estimation of the added mass coefficients.

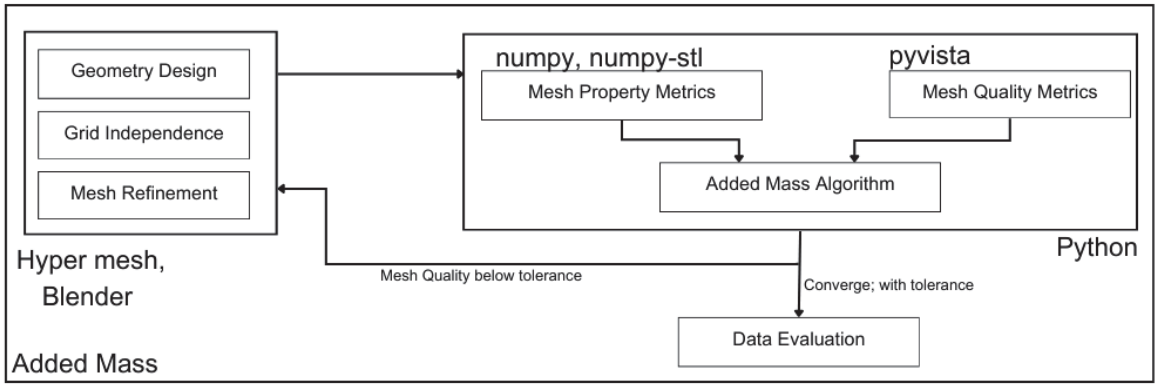

Figure 5.5 Application of BEM using python and its dependencies

The following sections discuss the available results for all the selected shapes and the influence of element quality over the accuracy of added mass coefficients.

5.3.1 Deploying Added Mass Algorithm for Standard Geometries

For this study, added mass coefficients are calculated using a laptop on Intel i7-11800H, with 16 GB RAM. Different cases with varied number of elements are considered to showcase the potential relation between the number of elements and accuracy of the solutions, computational costs in terms of time are also given for reference.

5.3.1.1 Added Mass Estimation for Sphere

The added mass coefficients obtained for the different number of elements for sphere are presented in Table 5.2 along with the theoretical reference presented by Morino (1974). The meshing for the sphere geometry is performed using the 2D mesh generation in HYPERMESH. The values for k_{11}, k_{22}, and k_{33} are equivalent as the Sphere has a uniform geometry across all axis. The small discrepancy observed between each value is considered due to the discretization techniques employed for the geometry. The values for k_{44}, k_{55} and k_{66} are under 10^{-9} and considered zero. While the additional refinement step enhances the overall estimation of the solution, achieving a perfect solution is not feasible due to the algorithm's reliance on STL files

Table 5.2 Estimated added mass of sphere using k_{11} values for gaussian quadrature (3-point rule) and subdivision (Nr, Nθ = 2), with reference values from Morino (1974)

n_e	Gaussian Quadrature (3-point rule)		Nr, Nθ = 2	
	k_{11}	Time	k_{11}	Time
1000	0.493470	145.80 s	0.498472	921.54 s
1500	0.493990	316.58 s	0.498404	2639.22 s
2000	0.494480	548.69 s	0.498697	1.05 h
2500	0.494880	823.10 s	0.498917	2.13 h
3000	0.495200	1670.73 s	0.499023	3.05 h
Reference (Morino (1974))	0.5000	—	0.5000	—

with triangular meshes for curved geometries. Thus, obtaining a fully discretized solution for a curved geometry remains unattainable.

5.3.1.2 Added Mass Estimation for Oblate Ellipsoid

The meshing for oblate ellipsoid is done with a similar approach as sphere, the element properties across the lateral axis have been redefined to achieve uniform surface area for all elements. The results obtained from the added mass algorithm are provided in Table 5.3 The values of k_{11} and

Table 5.3 Estimated added mass of oblate ellipsoid using gaussian quadrature (3-point rule) and subdivision (Nr, Nθ = 2) with reference values from Morino (1974)

n_e	Gaussian Quadrature (3-point rule)			Nr, Nθ = 2		
	$k_{11} = k_{22}$	k_{33}	Time	$k_{11} = k_{22}$	k_{33}	Time
1000	0.36102	0.85362	222.63 s	0.36441	0.86333	846.93 s
1500	0.36137	0.85535	489.33 s	0.36434	0.86389	2132.15 s
2000	0.36168	0.85664	859.80 s	0.36454	0.86467	1.05 h
2500	0.36194	0.85786	1355.56 s	0.36469	0.86541	1.68 h
3000	0.36213	0.85859	1923.45 s	0.36478	0.86568	2.72 h
Reference (Morino (1974))	0.365	0.865	—	0.365	0.865	—

k_{22} are equal for an oblate ellipsoid as the dimensions towards their lateral axis remain the same. Similarly the values for k_{44} and k_{55} remain same. The k_{66} value is considered zero as it tends to fall below 10^{-10} for all cases.

5.3.1.3 Added Mass Estimation of Prolate Ellipsoid

The estimated added mass coefficient for prolate ellipsoid is presented in Table 5.4 The values of

Table 5.4 Estimated added mass of prolate ellipsoid using gaussian quadrature (3-point rule) and subdivision (Nr, Nθ = 2) with reference values from Morino (1974)

n_e	Gaussian Quadrature (3-point rule)			Nr, Nθ = 2		
	k_{11}	$k_{22} = k_{33}$	Time	k_{11}	$k_{22} = k_{33}$	Time
1000	0.27679	0.63235	188.67 s	0.27939	0.63912	859.83 s
1500	0.27701	0.63229	464.45 s	0.27931	0.63840	0.69 h
2000	0.27723	0.63316	824.72 s	0.27944	0.63899	1.23 h
2500	0.27741	0.63377	1.34 h	0.27954	0.63935	1.92 h
3000	0.27756	0.63437	1.87 h	0.27957	0.63955	2.26 h
Reference (Morino, 1974)	0.278	0.634	—	0.278	0.634	—

k_{22} and k_{33} are equal in a prolate ellipsoid as the dimensions towards their vertical axis remain the same. Similarly, the values for k_{55} and k_{66} remain constant at pitch and yaw axis. The k_{44} value is considered zero as there is minimal moment upon the rolling axis, and the values obtained through the algorithm tend to fall below 10^{-10} for all cases with different numbers of elements.

5.3.1.4 Added Mass Estimation for Elliptical Cylinder

The estimated added mass coefficient for elliptical cylinder is given in Table 5.5 The values of

Table 5.5 Estimated added mass of elliptical cylinder using gaussian quadrature (3-point rule) and Subdivision (Nr, Nθ = 2)

$\mathbf{n_e}$	Gaussian Quadrature (3-point rule)				Nr, Nθ = 2			
	k_{11}	k_{22}	k_{33}	Time	k_{11}	k_{22}	k_{33}	Time
1000	0.53460	0.60548	0.80886	207.59 s	0.53237	0.60174	0.82082	931.15 s
1500	0.53706	0.61020	0.81567	456.17 s	0.53516	0.60679	0.82465	2612.09 s
2000	0.53835	0.61226	0.81874	807.71 s	0.53690	0.60900	0.82650	1.20 h
2500	0.53974	0.61467	0.82195	1722.30 s	0.53844	0.61141	0.82946	2.18 h
3000	0.53974	0.61467	0.82195	1814.90 s	0.53844	0.61141	0.82946	2.58 h

k_{11}, k_{22} and k_{33} represent added mass force acting towards the x, y and z axis, respectively.

Value of k_{33} is the highest of all other coefficients as the dimensions towards their vertical axis are the longest. Similarly, the values for k_{11} and k_{22} remain closer due to the similarity in dimensions over the lateral and longitudinal axis of the geometry. The values for roll, pitch and yaw are also given by k_{44}, k_{55} and k_{66}.

Both the angular radial subdivision and gaussian quadrature methods yield highly accurate non-dimensional added mass coefficients across different geometries. Notably, the gaussian quadrature approach proves to be more cost effective in terms of computation time while maintaining similar accuracy levels. Its efficiency makes it particularly preferable for extending analyses to more complex geometries. The complete implementation code for this method is available in the Appendix I.

CHAPTER 6

STRUCTURAL ANALYSIS OF PRESSURIZED AIRSHIPS USING FINITE ELEMENT ANALYSES

Structural conformation plays a significant role in maintaining the desired performance of any airship in ensuring its stability, maneuverability, and overall operational efficiency. In contrast to rigid and semi-rigid airships, which consists of dedicated load bearing structures, non-rigid airships rely entirely on internal gas pressure and membrane material properties to sustain their shape and operational performance. Ensuring adequate structural rigidity is, therefore, essential for stability, maneuverability, and payload optimization.

Figure 6.1 showcases the systematic procedure taken with ABAQUS, a general structural

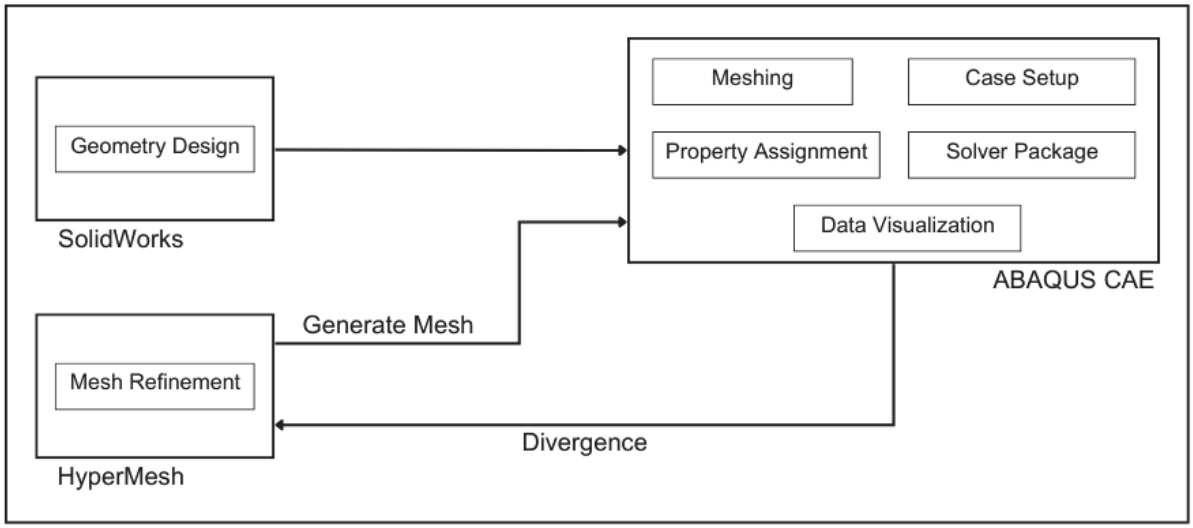

Figure 6.1 Detail procedure taken for rigidity assessment

analytical tool from Dassault Systemes. The details about the ABAQUS architecture are referenced from Smith (2009). This chapter discusses several conceptual arrangements designed and applied to analyze the structural behavior of all the geometries selected in the study. By leveraging the insights from the analytical solution, a reliable methodology and a specific data set are demonstrated to aid the airship selection process between all the geometries considered for the study.

6.1 Geometry Design and Visual Evaluation

The geometry designs required for the ABAQUS analysis have been performed using a separate CAD Package by Dassault Systemes called SOLIDWORKS. Similar to the designing process implemented in Section 4.1.1, SOLIDWORKS exceeds from Design Modeler's ability by providing extensive control over the design process and a vast array of post-processing features for further applications.

Unlike aerodynamics-based geometries, structural analysis models must explicitly account for inflation effects by discretizing the geometry into individual planar surfaces. This segmentation enables accurate finite element simulations, replicating real world inflation characteristics of non-rigid airships. All individual segments are later adjoined in the assembly module present in ABAQUS.

The exact dimensions and shape of the panels are derived from their manufacturability of the geometries. displays a four-panel assembly performed for the spherical airship used in the study. The significance of the number of panels and other related factors about the shape of airships is discussed in Chapter 6.6.

6.2 Material Selection and Property Assignment

The geometry designed in SOLIDWORKS is exported to ABAQUS through parasolid formats (.x_t, .x_b or .xmt). Appropriate scaling for the model is implemented before adding the imported geometries, as ABAQUS inherently uses micrometre (mm) as the import dimensions.

Table 6.1 Material definition of mylar

Density, ρ	1390 Kg/m^3
Membrane thickness, t	0.000254 m
Tensile Modulus, E	3.5 Gpa
Poissons ratio, ϵ	0.38
Friction Coefficient, μ	0.49

The subsequent step after geometry creation is to assign material and section definitions. The

required membrane must be light to reduce the material weight, less permeable, and easily accessible while being rigid enough to perform under subjected loading conditions. For the scope of the current analyses, Mylar is selected as the choice of material. All the required material properties of mylar are taken from MatWeb (2020) and provided in Table 6.1 for reference. To implement the methodology with custom materials, designated material properties can be changed with other popular membrane choices like polyurethane and poly vinyl chloride, which have been discussed in detail by Khoury & Gillett (1999).

6.3 Characterizing Contact Behavior Between Membrane Surfaces

This section delves into the interaction properties and conditions governing the inflatable segments and the entire geometry. We explore two distinct types of connections crucial to the overall structure. The first involves connecting individual membranes to form a single-piece envelope. This connection process is vital in creating a cohesive and robust airship structure.

The second connection type considers the self-interactions between the inflatable membranes while subjected to structural loading. These interactions are essential to accurately predict the behavior of the inflatable structure under applied forces and external conditions. Proper accounting for these interactions is crucial in obtaining a reliable and accurate solution estimation during finite element analysis (FEA).

The interaction module in ABAQUS addresses both types of connections and serves as a vital tool in simulating the behavior of the inflatable geometry and establishing the necessary boundary between the inflatable segments to ensure a stable and well-functioning airship design.

6.3.1 Contact Properties For Connections Between Distinct Panels

The assembly of individual membrane pieces to form a unified inflatable envelope involves employing a connection type known as tie constraints in the interaction module of ABAQUS. The most common types of joints for airship membranes are referenced from Mulay & Pant (2013), and demonstrated in Figure 6.2. The airships are designed to be an enclosed structure

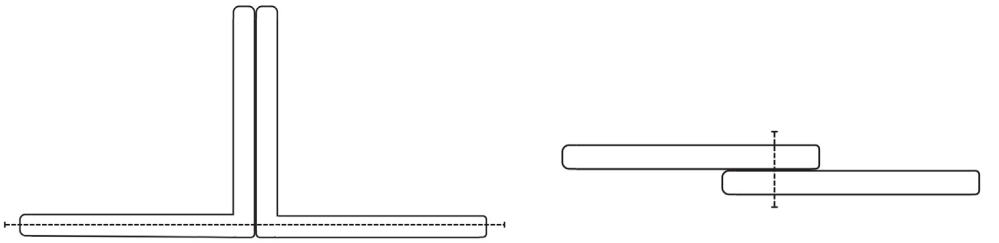

a) Edge Joint between inflatable segments b) Lap Joint between inflatable segments

Figure 6.2 Common edge joints in inflatables

and it is desirable to have a smooth outer surface for the inflatables to improve its aerodynamics performance. Since exploring the effects of different joint types is also crucial for accurately estimating airships' permeability and structural rigidity, we have selected edge joints due to their widespread use and ease of application in inflatable construction. A tie constraint between the curved edges of the membranes is added while placing the segments adjacent to each other to simulate a seam-like joint behavior between the edges.

6.3.2 Contact Properties for Interactions Between Inflatable Membranes

Airship membranes undergo significant changes during the inflation/deflation of their bladders. These changes in their geometry shape give rise to self-interaction between various membrane surfaces, while additional interactions can be observed at the troughs and wrinkles on the geometry's surface. Although such behavior may not be of concern in practical cases, analyzing thin shell bodies requires special consideration to maintain their structural integrity.

Particularly, elements with interconnected surfaces and those interacting under tension or compression can create intersection points, leading to inter-element penetration beyond their structural boundaries. This phenomenon is known as the intersection between interlinked elements.

To address these intersections and ensure accurate simulations, a reliable approach involves producing a refined mesh and reducing the interaction area between elements. The interaction

area can be reduced by designing fine mesh geometries. While this approach is a viable option, it increases the computational cost required to perform the simulations. Therefore, this study introduces an additional condition by using an intersection penalty factor between the elements. This penalty prevents negative intersections by providing a frictional force between interacting surfaces, ensuring they maintain a distinct boundary between their edges. To maintain consistency amongst all simulation cases, a standard penalty factor of 0.5 has been introduced. A detailed approach can be considered for dedicated analysis cases to predict a more accurate value of the penalty factor, thereby improving the overall behavior prediction.

By accurately accounting for these effects during the analysis, we can gain insights into understanding the response of the airship's membrane towards different forces and conditions, enhancing the design and performance assessments.

6.4 Mesh Generation in the Inflatable Membranes

Similar to the mesh generation procedure followed in Section 4.1.2, ABAQUS incorporates an inherent meshing module to perform geometry discretization for all selected geometry shapes. Moreover, ABAQUS also offers an additional element designation approach that utilizes membrane elements. This study utilizes element type "M3D3" to predict membrane behavior accurately. In this context, "M" signifies the element being a membrane element, "3D" represents its three-dimensional aspect, and "3" denotes the number of nodes in the element.

The loading conditions for assessment employ a consistent mesh profile across all geometry cases to ensure coherence in the final structural solutions within FEA. Pecora (2017) provides a comprehensive resource for further insights into structural analyses of inflatable structures and detailed information about different element types representing thin shell elements and their properties.

6.5 Grid Independence and Rigidity Assessment with Analytical Solutions

This study investigates the behavior of blimps under various loading scenarios using three arbitrary cases standard in blimp operations. The first case involves pressure loading to assess the stress distribution over the blimps. The subsequent two cases focus on maneuvering in the X and Y direction of the blimps. For the maneuvering cases, a cylinder geometry is introduced as an actuator on the blimp surfaces, attached using tie constraints to establish a load point. A grid independence study is performed for the stress evaluation case across all four blimp geometries. This study uses three distinct meshes with varying numbers of elements to perform a grid independence test to evaluate their impact on accuracy and computational costs. The study aims to obtain accurate solutions at lower computational costs.

The load module of ABAQUS is employed for all three loading conditions. For the pressure case, internal pressure is applied to the inflatables, while the maneuvering cases are subjected to additional loads on the actuators, simulating a thrust force in their body. This approach allows us to gain an elementary data set for the structural behavior of blimps under different operating conditions.

6.5.1 Structural Assessment of Spherical Blimp

This section is divided into three cases: pressure-induced stress evaluation and two maneuvering cases. The detailed methodology presented for the sphere is then applied to the other geometry cases.

6.5.1.1 Pressure Evaluation of Spherical Blimps

For the analytical approach to calculating stress and strain performance in a spherical inflatable, a standard numerical solution for stress and strain in a thin-walled spherical vessel is derived as a reference. Assuming the blimps are inflated to the desired geometry dimensions, then the internal pressure is the same as the external pressure acting on the geometry. Consequently, considering the standard external pressure as 1 atm, the internal pressure P is also presumed at

101,325 Pa. Using the available data for mylar in Table 6.1 and the internal pressure value, the stress for the studied spherical thin-walled vessel is determined as follows:

$$P\pi r^2 = \sigma_{sphere} 2\pi r t \tag{6.1}$$

where P is the internal pressure of the thin shell vessel, r is the radius of the vessel, σ_{sphere} is the stress induced by the internal pressure in the vessel, and t is the difference between the external surface and the internal surface of the pressure vessel.

To derive a solution for stress, Equation 6.1 can be further arranged as:

$$\sigma_{sphere} = \frac{pr}{2t} = \frac{101325 \cdot 0.392}{2 \cdot 0.000254} = 7.82 \times 10^7 Pa \tag{6.2}$$

Similarly, Equation 6.3 presents the numerical solution for the change in dimensions of a thin-shell spherical pressure vessel.

$$\Delta r = \frac{Pr^2}{2Et}(1 - \nu) = \frac{101325 \cdot 0.392^2}{2 \cdot 3.5 \times 10^9 \cdot 0.000254}(1 - 0.38) = 0.005429m \tag{6.3}$$

Where Δr is the change in the radius of the pressure vessel, P is the pressure, r is the radius of the vessel, and E is the Tensile modulus of the material of the pressure vessel, which in our case is $3.5 \times 10^9 Pa$ for mylar, and ν, the Poisson's ratio for the membrane is 0.38.

The change in the dimension obtained from the Equation 6.3 can be used to find the strain component of the pressure vessel:

$$\epsilon = \frac{\Delta r}{r} = \frac{0.005429}{0.392} = 0.01385 \tag{6.4}$$

where ϵ is the strain in the pressure vessel, corresponding to the change in the dimension by the original dimension of the vessel.

The described internal pressure of $P = 101325pa$ is imposed on the internal surface of the generated mesh grids in the load module of the ABAQUS to obtain the analytical solution for

the spherical geometries. A grid independence study is performed along with a numerical assessment where mesh A has 25,224 elements, mesh B has 40,080 elements, and mesh C has 82,216 elements. Section 6.5.2 - Section 6.5.4 summarizes the stress analysis obtained using FEA for all the inflatables with their corresponding geometries. The discrepancy between the

Table 6.2 Numerical and analytical solution from mesh independence study of sphere

Sphere	Number of elements	Stress, σ (Pa)	Strain, ϵ ($\frac{\delta r}{r}$)	Error (%)
Mesh A	25,224	7.93×10^7 Pa	0.01406	0.17
Mesh B	40,080	7.94×10^7 Pa	0.01407	0.12
Mesh C	82,216	7.97×10^7 Pa	0.01412	0.09
Numerical solution	-	7.82×10^7 Pa	0.01385	-

results presented in Table 6.2 demonstrates that increasing mesh resolution beyond Mesh B yields diminishing improvements in accuracy while significantly raising computational costs. Therefore, Mesh A is selected for subsequent studies, balancing precision with computational efficiency. Thus to reduce the computational time needed for the convergence, mesh A is selected for the remainder of the loading cases.

6.5.1.2 Deflection Analysis for Standard Maneuvering Cases in Spherical Blimp

Precise actuator placement is crucial for achieving efficient control and maneuverability in non-rigid airships. Unlike rigid configurations where actuators are mounted on dedicated structures, non-rigid airships must attach actuators directly to their membrane surfaces. This results in localized deflections that can affect thrust alignment, introducing unwanted flight deviations. In the case of non-rigid or semi-rigid airships, these actuators are typically laid upon the rigid components of the structure to ensure optimal performance and avoid potential misalignment in the actuators. However, non-rigid airships gain their rigidity solely through their internal pressure and lack such rigid elements for actuator attachment. Thus actuators are directly attached to the membrane surface in non-rigid blimps. When the actuators are engaged in the operation, this direct attachment creates a deflection between the alignment of the actuators. This deflection can reduce the airship's dynamic robustness and performance.

Thus, assessing deflection can help select a satisfactory actuator location and maintain ideal flight performance.

This study assumes the airships are inflated at a balanced pressure to maintain rigid surface integrity. The deflection performance between actuators is analyzed for two standard maneuvering cases. The first case involves maneuvering towards the X-direction, corresponding to forward thrust. The second case involves maneuvering towards the Z-direction to attain additional lift through thrust maneuvering. By comprehensively assessing the membrane deflection under these maneuvering scenarios, we can improve our understanding of the dynamic behavior of non-rigid airships and optimize actuator placement for their effective control and maneuverability. To

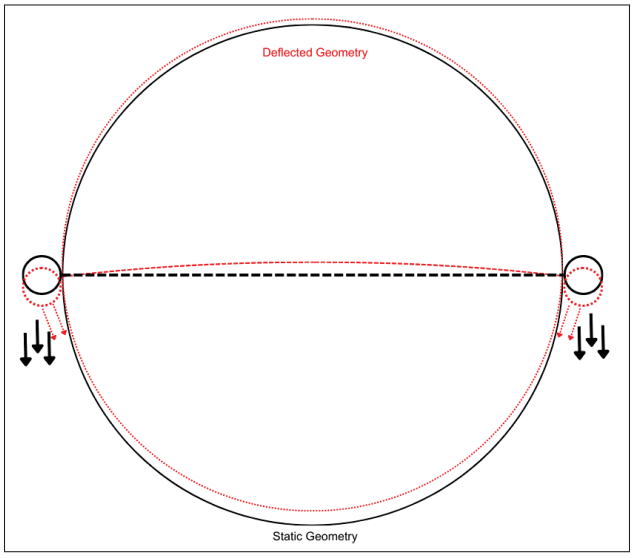

Figure 6.3 Actuator placement in spherical blimp

simplify both cases and minimize any additional dynamic effects, Figure 6.3 showcases the planned location for the actuators in a static spherical blimp depicted in black and the actuator deflection occurring under thrust generated while maneuvering depicted in red.

As discussed in the previous section, the joints between the actuator surface and the blimp membrane are performed by adding tie constraints between the surfaces. The mesh for the actuator is performed using the standard rigid "C3D8R" element type, which are "3D" elements with eight nodes in their geometry.

The deviations between the actuators are analyzed using a parametric study while the geometries maneuver at a velocity of $1m/s$, and a sudden thrust of $1N$ is added to simulate an acceleration. The deflection occurring between the actuator due to this sudden change in its actuator motion is summarized for X and Y maneuvering in Figure 6.4 The deflection between the actuators is

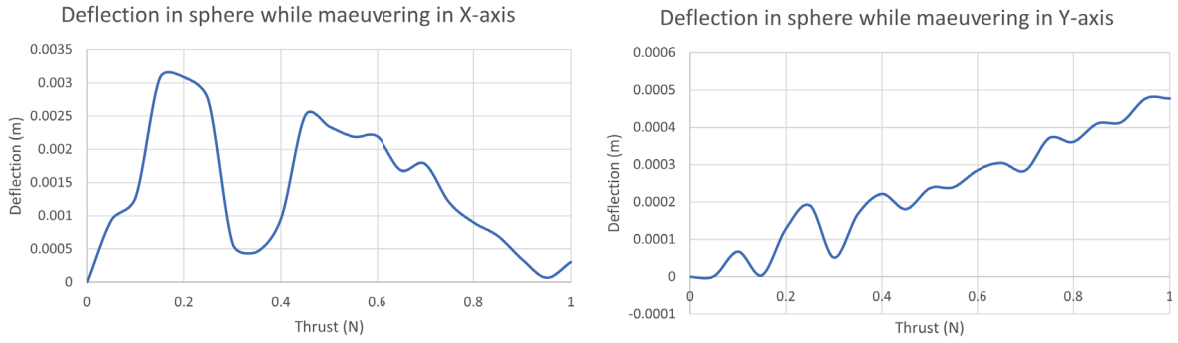

a) Deflection while X maneuvering

b) Deflection while Y maneuvering

Figure 6.4 Analytical solution for deflection analysis in sphere

negligible with the current actuator placement, which is sufficient for the intended design range, considering that the airships are designed for low-speed indoor operations. Figure 6.4 presents the deviation between the actuators at specific range of thrust vectors. The change variation in the deflection across range of thrust is attributed to the local inertia effects occurring at the specific actuator present at the membrane joint. In the future, the data for this deflection can be utilized in a simple dynamic model to test and improve the dynamic maneuvering of the airships. The methodology described here is applied to all the other geometries, with adjusted parameters for the different shapes.

6.5.2 Structural Assessment of Oblate Blimp

The actuator placement in spherical blimp and oblate blimp would be same from the top view for representation. The grid independence study performed for stress analysis in oblate blimp include mesh A with 24,722 elements, mesh B with 51,146 elements, and mesh C with 98,542 elements. All the elements are "M3D3" membrane-type "3D" elements with structured meshing

implemented in the ABAQUS meshing module. Table 6.3 provides the solution obtained for the ultimate stress observed in varied mesh profiles of oblate blimp. The actuator deflection test

Table 6.3 Analytical solution from mesh independence study of oblate

Oblate	Number of elements	Stress, σ (Pa)
Mesh A	24,722	1.349×10^8 Pa
Mesh B	51,146	1.415×10^8 Pa
Mesh C	98,542	1.438×10^8 Pa

conducted for the oblate blimp with mesh A demonstrates a maximum deviation of $1.6 \times 10^{-4} m$ while translating forward along the X-axis, and $1.8 \times 10^{-3} m$ while changing altitude along the Z-axis. While the deflection in the X-axis is considered negligible, the actuator placement for the vertical axis can be improved through further experimentation in the actuator positions or by implementing additional reinforcement at the structure-membrane interaction surface. The deflection occurring between the actuator with change in the thrust of actuators is summarized for X and Y maneuvering in Figure 6.5.

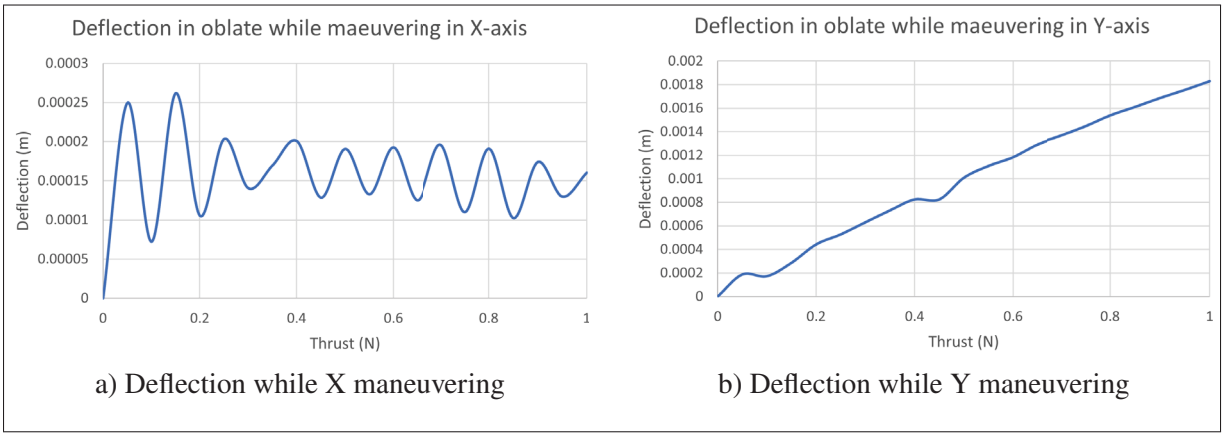

a) Deflection while X maneuvering

b) Deflection while Y maneuvering

Figure 6.5 Analytical solution for deflection analysis in oblate

6.5.3 Structural Assessment of Prolate Blimp

Figure 6.6 showcases the planned location for the actuators in a static prolate blimp. The grid independence study performed for stress analysis in prolate blimp include mesh A with 25,982

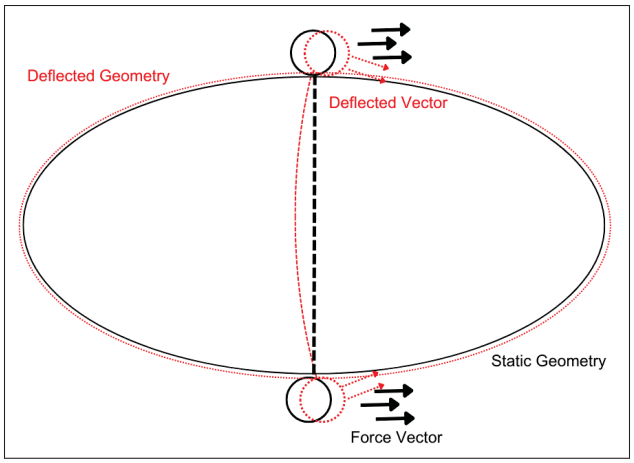

Figure 6.6 Actuator placement in prolate blimp

elements, mesh B with 50,520 elements, and mesh C with 1,01,472 elements. All the elements are modeled "M3D3" membrane-type "3D" elements with structured meshing implemented in the ABAQUS meshing module. Table 6.4 provides the solution obtained for the ultimate stress observed in varied mesh profiles of prolate blimp. The actuator deflection test conducted

Table 6.4 Analytical solution from mesh independence study of prolate

Prolate	Number of elements	Stress, σ (Pa)
Mesh A	25,982	1.034×10^8 Pa
Mesh B	50,520	1.085×10^8 Pa
Mesh C	1,01,472	1.026×10^8 Pa

for the prolate blimp with mesh A demonstrates a maximum deviation of $5 \times 10^{-4} m$ while translating forward along the X-axis, and $1.1 \times 10^{-4} m$ while changing altitude along the Z-axis. The actuator placement for the longitudinal and vertical axis can be improved through further experimentation in the actuator positions or by implementing additional reinforcement at the structure-membrane interaction surface. The deflection occurring between the actuator with change in the thrust of actuators is summarized for X and Y maneuvering in Figure 6.7.

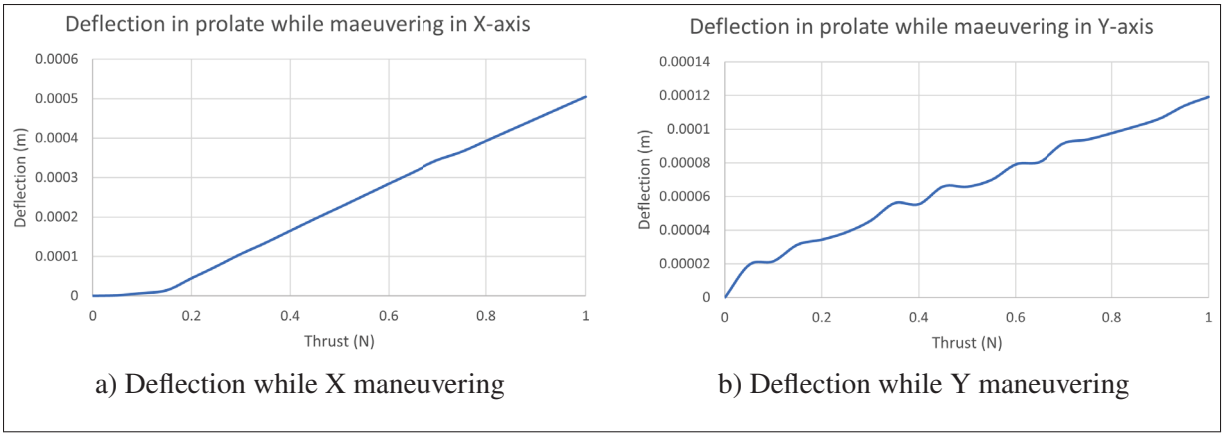

a) Deflection while X maneuvering

b) Deflection while Y maneuvering

Figure 6.7 Analytical solution for deflection analysis in prolate.

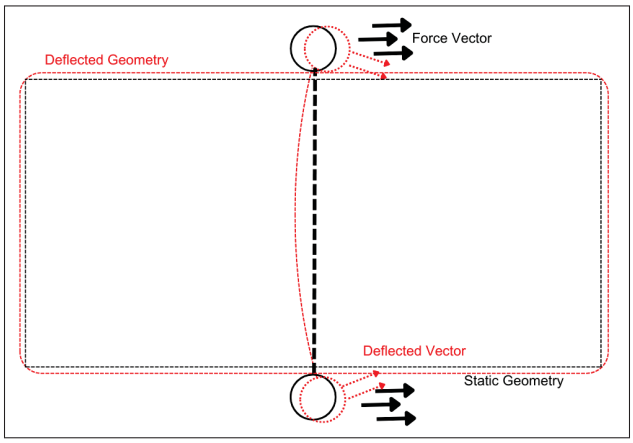

Figure 6.8 Actuator placement in spherical blimp

6.5.4 Structural Assessment of Elliptical Cylinder Blimp

Figure 6.8 showcases the planned location for the actuators in a static elliptical blimp. The grid independence study performed for stress analysis in elliptical cylinder blimp include mesh A with 27,334 elements, mesh B with 46,554 elements, and mesh C with 1,00,820 elements. All the elements are modeled "M3D3" membrane-type "3D" elements with structured meshing implemented in the ABAQUS meshing module. Table 6.5 provides the solution obtained for the ultimate stress observed in varied mesh profiles of the elliptical cylinder blimp. The actuator deflection test conducted for the oblate blimp with mesh A demonstrates a maximum deviation

Table 6.5 Analytical solution from mesh independence study of elliptical cylinder

Elliptical Cylinder	Number of elements	Stress, σ (Pa)
Mesh A	27,334	3.095×10^8 Pa
Mesh B	46,554	3.078×10^8 Pa
Mesh C	1,00,820	3.045×10^8 Pa

of $4.9 \times 10^{-4} m$ while translating forward along the X-axis, and $3.8 \times 10^{-4} m$ while changing altitude along the Z-axis. The deflection in the X axis is better than the prolate blimp, while the actuator placement for the vertical axis is better than both oblate and prolate blimps. The deflection occurring between the actuator with change in the thrust of actuators is summarized for X and Y maneuvering in Figure 6.9.

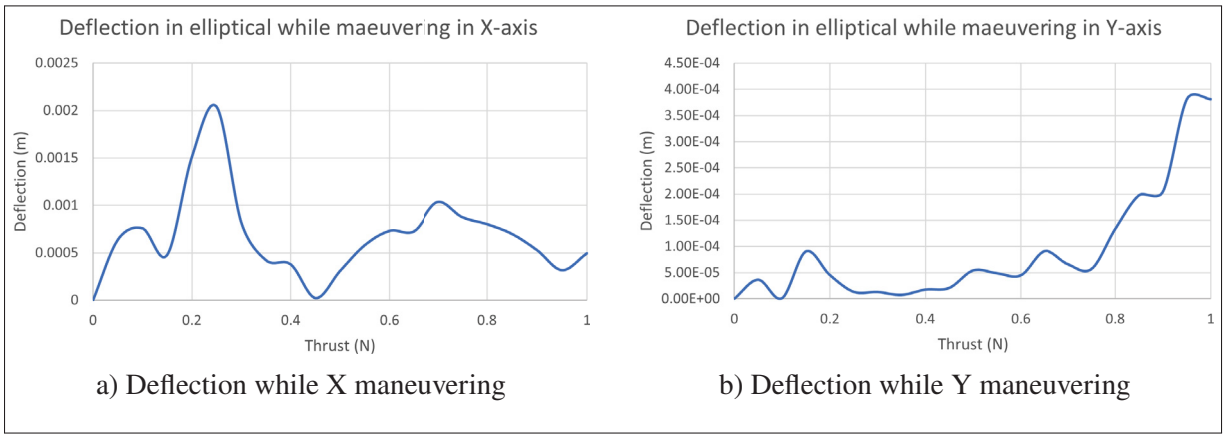

a) Deflection while X maneuvering

b) Deflection while Y maneuvering

Figure 6.9 Analytical solution for deflection analysis in elliptical.

6.6 Analyzing Surface Wrinkle Density for Aesthetic Evaluation

Aesthetics in airships refers to their capacity to retain their intended shape appeal after inflation. The following chapter evaluates the surface geometry to identify variation in their local area with respect to the total surface area to ascertain a distinct parameter and define the aesthetics of each considered shape. The assessment utilizes a Python-based script over the designed geometries to process and identify wrinkles over the local surface area and illustrate the geometry region with wrinkle definitions.

6.7 Aesthetic Characterization of the Designated Geometries

This chapter offers a methodology to create piece-wise segments that, when adjoined, facilitate the fabrication of an airship featuring their ideal desired shape. Mueller *et al.* (2004) and Gawale, Raina, Pant & Jahagirdar (2009) briefly describe the challenges associated with the fabrication of an airship. Instead, the subsequent step of the aesthetics factor focuses on attaining dimensions of flattened parts capable of achieving the required form for inflated airships. This ensures a stable and aesthetic airship design as we are only concerned with the non-rigid airships for this study. This complexity is reduced to seam joints between individual segments. By following the procedure of the aesthetics factor, more complex rigid structures can be incorporated into the design to improve the airship's rigidity performance.

6.7.1 Effects of Wrinkles Over Aesthetics

Wrinkles significantly impact the rigidity performance of airships by introducing localized weak points that can compromise structural integrity, especially in non-rigid or semi-rigid designs. Beyond structural concerns, aesthetics also plays a critical role, particularly for indoor airship applications where human-blimp interactions are possible. A visually appealing design enhances the airship's public perception, making it essential for blimps to maintain a presentable appearance when interacting with the general public.

In this section, we use the same geometry analyzed for rigidity to evaluate wrinkle formation over specific areas of the geometry. By identifying zones prone to wrinkle formation, targeted modifications can be implemented, such as deploying rigid elements in semi-rigid and rigid designs, to mitigate these effects and enhance both structural performance and visual appeal.

6.7.1.1 Flattening the Dissected Geometries for Inflation Analysis

The subsequent step in the process involves utilizing the flatten module in SOLIDWORKS to facilitate the manufacturing of the inflatable airship. However, it's important to note that

this module can only be applied to surface geometries. Therefore, before proceeding with the flattening process, all the geometry surfaces are remodeled as planar models.

The flatten module allows us to obtain flattened segments from the reference geometry. These segments serve as crucial components for the subsequent manufacturing process. To ensure proper segmentation during manufacturing, initiation points are established to determine the locations at which the geometries are effectively flattened.

The flattened segments and the reference geometry, representing the initiation points located at the bottom of the geometry in the segmentation process. Having obtained the flattened pieces, we can measure their dimensions. These measurements determine the separate membrane pieces required for assembling the inflatable airship.

The number of pieces needed for assembly and the complexity involved in manufacturing them are essential considerations for assessing the aesthetics of the inflatable airship. By carefully examining these factors, we can make informed decisions regarding the optimal shape factor that ensures efficient manufacturing and accurate representation of the desired final shape.

6.7.1.2 Wrinkle Analysis of Sphere Airship After Inflation

This section discusses the ability of the airship to retain its desired form after inflation. The blimps created by adjoining the individual pieces are inflated to check their aesthetics and Wrinkle analysis performance. This change in shape is a crucial identification to determine their significance over other parameters. Figure 6.10 displays pressure contour in an inflated spherical blimp. While the desired shape is maintained, there is an 4.38% expansion in the volume of the geometry. This expansion increases the corresponding payload, and the change in shape increases the drag force affected on the body.

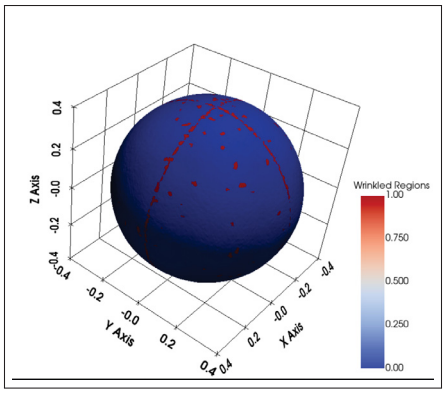

Figure 6.10 Visualizing spherical blimp in fully inflated state

6.7.2 Wrinkle Analysis of Oblate Airship After Inflation

Following the methodology demonstrated in Section 6.7, the oblate airship is manufactured by an edge joint between two flat pieces. Having the lowest number of pieces, oblate has the lowest manufacturing complexity amongst all the other shapes taken in the study. ABAQUS is used for

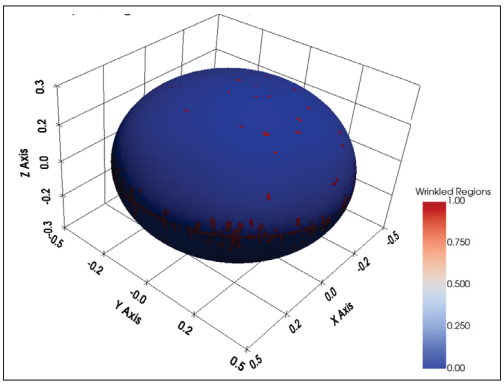

Figure 6.11 Visualizing oblate blimp in fully inflated state

inflation analysis as it has an inherent Fluid Cavity Module. The source of the fluid pressure is kept at the center of the volume of the geometry. The shape attained after pressure inflation of the designed geometry observes an additional 6.8 % expansion in the geometry volume. Similar to the spherical blimp, this expansion increases the available payload and subjected drag force. Several wrinkle patterns are also observed along the seam, indicating overstretching at the top and bottom edges of the body.

6.7.3 Wrinkle Analysis of Prolate Airship after Inflation

The dimensions of the prolate blimp derived through the aesthetics procedure. It is designed using four individual segments. Unlike the spherical blimp, the flat planes for prolate blimps have higher height and less width to define the elongated geometry. All the pieces are joined with an edge joint to create an enclosed envelope.

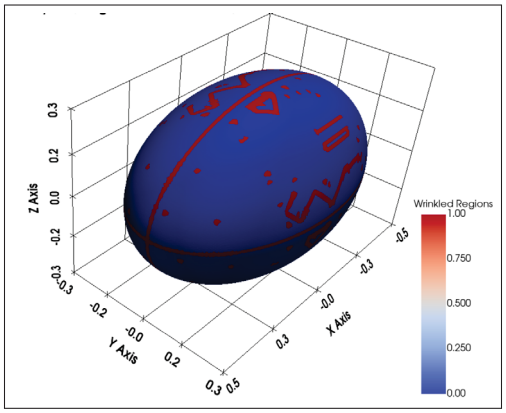

Figure 6.12 Inflated prolate blimp

The final inflated geometry for the prolate airship has a 4.73% increase in volume to the ideal geometry. Figure 6.12 displays the pressure contour generated over the inflated geometry showcasing that the highest pressure is observed towards the lateral axis of the blimp.

6.7.4 Wrinkle Analysis of Elliptical Cylinder Airship after Inflation

The elliptical cylinder airship is designed using two elliptical pieces and two rectangular pieces, reducing the aesthetics of the shape as the edge joints are made between the rectangular edges, and the elliptical pieces are used as the end plugs for the cylinder.

The final inflated geometry for the elliptical cylinder airship has a 24.06 % higher volume than the designed ideal geometry. The higher volume increases the buoyancy and drag force over the body. Figure 6.13 shows the distortion at the lateral axis of the geometry due to the pressure difference. Excess wrinkles are present over the seam length of the geometry, where further reinforcement is required to reduce expansion and increase rigidity over the geometry.

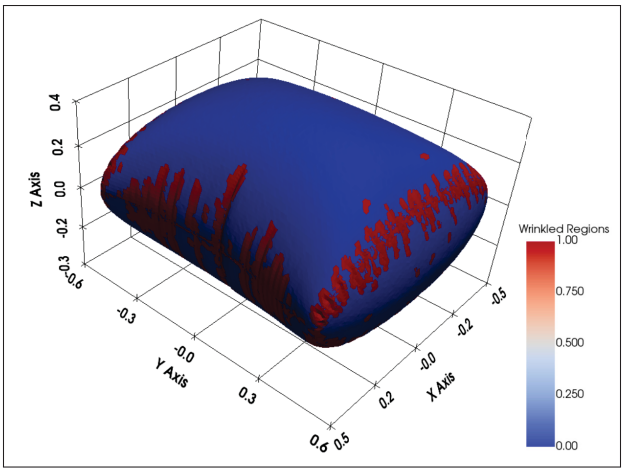

Figure 6.13 Inflated elliptical cylinder blimp

6.7.5 Adapting Methodology for Comprehensive Analyses

The following methodology can be adapted to determine the aesthetics of all the airship shapes discussed in the section. This methodology can be utilized to create complex custom structures for varied operational requirements by making a reference geometry for any desired shape. Furthermore, by aligning the geometry in SOLIDWORKS rather than in the assembly module of ABAQUS before performing the necessary analytical study, we can streamline the process while ensuring the accuracy and stability of the final inflated airship. The described methodology can be used to improve the overall performance and aesthetics of the airship, Thus making it a critical parameter in the design and manufacturing of airships for various applications.

CHAPTER 7

PARAMETRIC ANALYSIS FOR AIRSHIP DESIGN OPTIMIZATION

Designing an effective non-rigid airship requires a comprehensive evaluation of multiple parameters, encompassing aerostatic, aerodynamic, and structural performance. While previous chapters provide methodology for analyzed these parameters, a complete parametric evaluation along with the evaluated results are presented in this chapter.

7.1 Comparative Analysis Framework

This chapter presents a systematic and quantitative analysis, comparing the selected airship geometries sphere, prolate ellipsoid, oblate ellipsoid, and elliptical cylinder using standardized metrics. The study provides a structured design optimization framework integrating aerostatic lift efficiency, aerodynamic drag, added mass effects, structural integrity, manufacturability, and operational sustainability.

7.1.1 Airship Geometries Considered

The following four geometries are analyzed based on the parametric dimensions defined in Table 3.1:

- **Sphere**: Baseline shape with lowest surface-to-volume ratio, often used for validation.
- **Prolate Ellipsoid**: Conventional airship geometry optimized for aerodynamics.
- **Oblate Ellipsoid**: A low aspect-ratio variant, influencing aerodynamics and stability.
- **Elliptical Cylinder**: Unconventional shape providing high payload but increased drag.

7.1.2 Evaluation Parameters

Each airship geometry is evaluated across five major performance categories: Aerostatic, aerodynamic, inertial, structural, and aesthetics that are considered as the key design constraints and performance parameters of small indoor blimp operation. These parameters are selected

based on their critical contribution to operational feasibility. Table 7.1 includes the selected parameters and their corresponding notations and units.

Table 7.1 Comparison parameters for parametric evaluation of airship geometries

Category	**Parameter**	**Symbol**	**Unit**
Aerostatic	Volume	V	m^3
Aerostatic	Surface Area	S	m^2
Aerostatic	Payload Lift	L_d	g
Aerostatic	Expansion Factor	α	%
Aerostatic	Permeability Loss	P	g/hr
Aerodynamic	Drag Coefficient	C_D	-
Inertial	Added Mass Coefficient	K_{ij}	-
Structural	Maximum Stress	σ	Pa
Structural	Deflection under Load	δ	m
Aesthetics	Wrinkle Density	ω	%

Each parameter listed above are taken from the detailed analyses presented in Chapter 3 to Chapter 6, derived from numerical, and analytical solutions performed for each shape. These results are used not only to evaluate the individual performance of each shape but also to provide a comparative framework that enables holistic design optimization.

To facilitate an objective and visual comparison between shapes, all parameter results are normalized to a non-dimensional scale of $[0, 1]$, where higher values indicate superior performance. For metrics where lower values imply better performance such as drag coefficient (C_D), permeability loss (P), wrinkle density (ω), and maximum stress (σ), an inversion method is applied prior to normalization. This ensures consistent interpretation across all parameters, allowing performance strengths and weaknesses to be visualized uniformly across different categories.

The normalization follows the general rule:

$$x_{\text{norm}} = \begin{cases} \frac{x - x_{\min}}{x_{\max} - x_{\min}}, & \text{if higher is better} \\ 1 - \frac{x - x_{\min}}{x_{\max} - x_{\min}}, & \text{if lower is better} \end{cases} \tag{7.1}$$

This transformation allows for effective multi-criteria decision-making and enables performance mapping with plots. The normalized scores are subsequently used in the shape-specific evaluations and design recommendations. This parametric evaluation methodology aims to bridge the gap between validated analysis and accessible design decision making, enabling users to rapidly identify geometries that align with their specific operational requirements whether maximizing lift, minimizing drag, or ensuring structural stability for confined environments.

7.2 Equations of Motion for Small Indoor Airships

To evaluate the dynamic behavior of the blimps within confined indoor spaces, it is essential to define their governing equations of motion. These equations serve as the framework where all evaluated parameters including drag, added mass, and buoyancy are generalized to determine the forces influencing translational and rotational dynamics of the blimp.

In this work, the general form of the nonlinear 6-DOF equations of motion follows the formulation presented by Li et al. Li *et al.* (2011), as shown earlier in Equation (1.1). This model captures both translational and rotational dynamics and accounts for inertial coupling, gravitational effects, and external aerodynamic and control forces. For the purposes of this study, the model of equations are adapted and simplified to suit low-speed, passively stabilized indoor airship operations.

The following assumptions are introduced based on the nature of small, non-rigid indoor blimps:

- The body's motion is assumed to be primarily translational in the longitudinal x direction.
- Rotational forces are considered negligible due to active stabilization and slow maneuvering.
- Coriolis and centripetal effects are considered minimal resulting in negligible effects.
- Buoyancy forces are assumed constant which act as static offsets.

Under these assumptions, we adopt a simplified body-fixed 6-degree-of-freedom (DOF) dynamic model from Fossen (1994). The general form of the equations of motion for a rigid body

immersed in surrounding air is expressed as:

$$M\dot{v} + C(v)v + Dv = \tau \tag{7.2}$$

Where in 7.2:

- $v = [u, v, w, p, q, r]^T$ is the velocity vector in surge, sway, heave, roll, pitch, and yaw.
- $fM = M_{RB} + M_A$ is the total mass matrix including rigid body and added mass contributions.
- $C(v)$ is the Coriolis and centripetal matrix (neglected here).
- D is the damping matrix, predominantly governed by drag coefficients.
- τ is the generalized force vector applied by actuators or external fields.

Given the operating conditions of small indoor airships, we simplify the model to focus on drag and added mass coefficients:

$$\mathbf{M}_{3\times3}\dot{\mathbf{v}} + \mathbf{D}_{3\times3}\mathbf{v} = \boldsymbol{\tau}_{3\times1} \tag{7.3}$$

The mass matrix **M** includes added mass coefficients extracted from numerical results (Chapter 5), and the damping matrix **D** incorporates directional drag coefficients derived from CFD simulations (Chapter 4).

The simplified force equation in matrix form becomes:

$$\begin{bmatrix} k_{11} & 0 & 0 \\ 0 & k_{22} & 0 \\ 0 & 0 & k_{33} \end{bmatrix} \begin{bmatrix} \dot{u} \\ \dot{v} \\ \dot{w} \end{bmatrix} + \begin{bmatrix} \frac{1}{2}\rho S_x C_{D_x} & 0 & 0 \\ 0 & \frac{1}{2}\rho S_y C_{D_y} & 0 \\ 0 & 0 & \frac{1}{2}\rho S_z C_{D_z} \end{bmatrix} \begin{bmatrix} u \\ v \\ w \end{bmatrix} = \begin{bmatrix} \tau_x \\ \tau_y \\ \tau_z \end{bmatrix} \tag{7.4}$$

Where:

- k_{ii} are added mass coefficients for surge (k_{11}), sway (k_{22}), and heave (k_{33}) directions.
- C_{D_i} are drag coefficients along each principal axis, computed via CFD.
- S_i are the projected frontal areas in the respective directions.
- τ_i are the net actuator forces or disturbances.

These matrices provides a unified representation of how geometry shape properties affect their dynamic behavior. The specific values for k_{ii} and C_D used in the above formulation are summarized in Table 5.2-5.5 and Figure 4.7. By substituting geometry specific parametric values into Equation 7.4, each performance criteria and dynamic response are compared quantitatively across different geometry shapes.

7.3 Parametric Evaluation and Equations of Motion for Airship Geometries

Having established the governing equations of motion and the evaluated parameters, this section presents a detailed comparative evaluation of each shape. By using normalized performance metrics, we visualize the comparison for each geometry, their parametric strengths and weaknesses are identified based on their physical characteristics and analytical results. We also present the motion equations using the specific values of added mass and drag coefficients obtained from CFD (ANSYS FLUENT) and BEM (Potential theory) analyses, providing a performance profile. Key observations from each evaluation support geometry selection based on desired operational requirements.

7.4 Parametric Evaluation and Equations of Motion of Shapes

This section presents a detailed performance comparison of the four airship geometries using the normalized parameters as defined previously. The selected parameters originate from numerical and analytical simulation and analysis from Chapter 3 to Chapter 6. Each geometry is evaluated individually by their aerodynamic, and inertial parameters into a dynamic equation of motion.

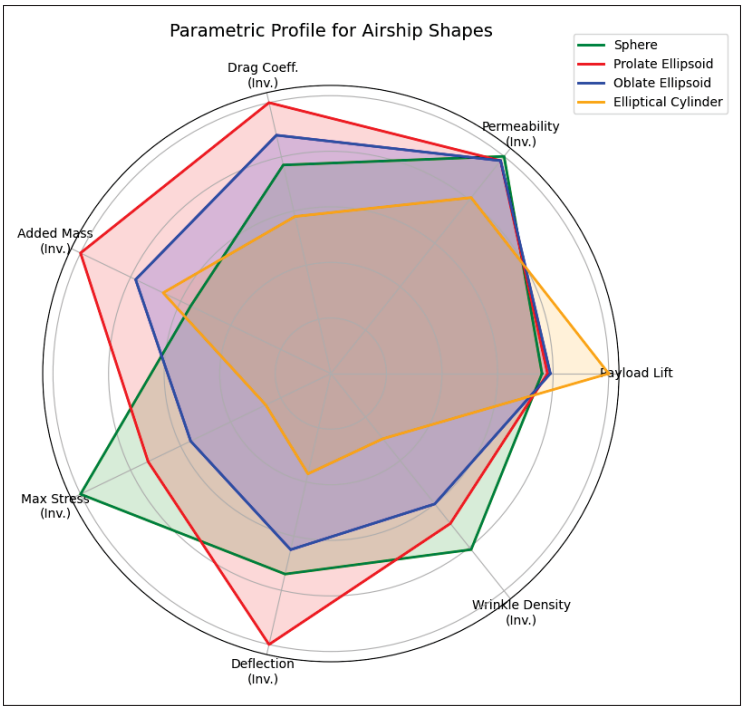

Figure 7.1 Normalized parameter radar plot for all shapes

The radar plots included in Figure 7.1 represent normalized scoring across seven key parameters: payload lift, permeability loss (inverted), drag coefficient (inverted), added mass (inverted), maximum stress (inverted), deflection (inverted), and wrinkle density (inverted). By normalizing these parameters on a scale from 0 to 1, higher scores consistently denote better performance, allowing for an intuitive visual comparison between all selected shapes.

The geometry specific dynamic equation of motion, derived using the added mass and drag values discussed in previous chapters and the parametric plots of each shapes are used to summarize relative strengths and weaknesses for a cross performance metrics.

7.4.1 Evaluation of Sphere

The sphere, as the most symmetrical shape with significant references, provides a reliable baseline for performance validation. Due to its symmetry, its dynamic response is same across

all translational axes. The results show near identical values for added mass and drag in all directions, confirming the geometric symmetry and uniform fluid-body interaction.

Dynamic Equation of Motion:

$$\begin{bmatrix} 0.50 & 0 & 0 \\ 0 & 0.50 & 0 \\ 0 & 0 & 0.50 \end{bmatrix} \begin{bmatrix} \dot{u} \\ \dot{v} \\ \dot{w} \end{bmatrix} + \begin{bmatrix} 0.27 & 0 & 0 \\ 0 & 0.27 & 0 \\ 0 & 0 & 0.27 \end{bmatrix} \begin{bmatrix} u \\ v \\ w \end{bmatrix} = \begin{bmatrix} \tau_x \\ \tau_y \\ \tau_z \end{bmatrix} \tag{7.5}$$

Key Insights:

- Symmetrical performance allows predictable dynamics and straightforward control tuning.
- Excellent aerostatic properties with the lowest permeability loss and highest material stability.
- Higher added mass induces slower acceleration but adds stability.
- Well suited for test platforms and indoor hovering use cases.

7.4.2 Evaluation of Oblate Ellipsoid

The oblate ellipsoid is flattened along the vertical axis, enhancing lateral stability and reducing rotation in pitch axis. Its drag performance is slightly better than the sphere, while retaining similar aerostatic benefits.

Dynamic Equation of Motion:

$$\begin{bmatrix} 0.362 & 0 & 0 \\ 0 & 0.362 & 0 \\ 0 & 0 & 0.859 \end{bmatrix} \begin{bmatrix} \dot{u} \\ \dot{v} \\ \dot{w} \end{bmatrix} + \begin{bmatrix} 0.19 & 0 & 0 \\ 0 & 0.19 & 0 \\ 0 & 0 & 0.56 \end{bmatrix} \begin{bmatrix} u \\ v \\ w \end{bmatrix} = \begin{bmatrix} \tau_x \\ \tau_y \\ \tau_z \end{bmatrix} \tag{7.6}$$

Key Insights:

- Offers a good compromise between visual aesthetics and performance.
- High added mass in heave (k_{33}) implies lower vertical agility.
- Slightly better drag efficiency than sphere but lower structural efficiency.

- Ideal for indoor promotional displays and payload surface mounting.

7.4.3 Evaluation of Prolate Ellipsoid

The prolate ellipsoid, being aerodynamically optimized along the flow axis, has the lowest drag of all shapes. This makes it ideal for efficient forward flight or surveillance tasks requiring endurance.

Dynamic Equation of Motion:

$$\begin{bmatrix} 0.278 & 0 & 0 \\ 0 & 0.634 & 0 \\ 0 & 0 & 0.634 \end{bmatrix} \begin{bmatrix} \dot{u} \\ \dot{v} \\ \dot{w} \end{bmatrix} + \begin{bmatrix} 0.16 & 0 & 0 \\ 0 & 0.27 & 0 \\ 0 & 0 & 0.27 \end{bmatrix} \begin{bmatrix} u \\ v \\ w \end{bmatrix} = \begin{bmatrix} \tau_x \\ \tau_y \\ \tau_z \end{bmatrix} \tag{7.7}$$

Key Insights:

- Best aerodynamic performance, lowest C_D and favorable K_{ij} values.
- Balanced structure allows good control response and minimal wrinkle formation.
- High normalized scores make it ideal for long-endurance applications.
- Suitable for continuous motion indoor missions like inspection or tracking.

7.4.4 Evaluation of Elliptical Cylinder

The elliptical cylinder maximizes volume and lift, but suffers from compromised aerodynamic and structural properties. It is best suited for applications where static lift and payload matter more than mobility.

Dynamic Equation of Motion:

$$\begin{bmatrix} 0.54 & 0 & 0 \\ 0 & 0.61 & 0 \\ 0 & 0 & 0.82 \end{bmatrix} \begin{bmatrix} \dot{u} \\ \dot{v} \\ \dot{w} \end{bmatrix} + \begin{bmatrix} 0.92 & 0 & 0 \\ 0 & 0.64 & 0 \\ 0 & 0 & 0.113 \end{bmatrix} \begin{bmatrix} u \\ v \\ w \end{bmatrix} = \begin{bmatrix} \tau_x \\ \tau_y \\ \tau_z \end{bmatrix} \tag{7.8}$$

Key Insights:

- Largest volume and payload capacity among the evaluated shapes.
- Highest drag and poor structural conformation demand extra reinforcement.
- Significant vertical added mass indicates inertia against lift forces.
- Best suited for static advertising or light-lift display roles in open indoor environments.

7.5 Use Cases: Shape Selection Based on Demonstration Application Requirements

This section highlights a practical methodology of utilizing the parametric results for application specific design selection. The normalized scores, equations of motion, and operational trade-offs enable designers to match airship geometry to desired performance attributes.

7.5.1 Use Case I: Long-Duration Surveillance Blimp

Requirements: Sustained flight time, low drag for energy efficiency, stable lift-to-weight balance, minimal oscillations during slow maneuvering.

Recommended Shape: Prolate Ellipsoid

Motivation:

- The prolate ellipsoid exhibits a relatively low drag coefficient ($C_D \approx 0.16$ in x-axis), as shown in Chapter 4, minimizing drag forces and thereby extending flight duration on limited energy requirements.
- Its added mass distribution is balanced across longitudinal and vertical axes ($k_{11} \approx 0.278$, $k_{33} = k_{33} \approx 0.634$), promoting smooth transitions during acceleration and deceleration without inducing sharp pitch or sway.
- The elongated geometry contributes to a high internal aspect ratio, which improves volume-to-surface efficiency and helps maintain envelope pressure under small perturbations, crucial for stability in indoor conditions.

- From the plot (Figure 7.1), the prolate shape ranks favorably in drag, stability, and inertial characteristics while trading off slightly in surface area and compactness—acceptable for a surveillance role.

Key Insights: The prolate ellipsoid's aerodynamic efficiency and stable motion response make it well suited for persistent aerial monitoring tasks such as warehouse patrolling or automated inventory tracking.

7.5.2 Use Case II: Advertising Blimp for Indoor Events

Requirements: High surface area for branding, visual symmetry, low-speed mobility or static hovering, structural resilience.

Recommended Shape: Oblate Ellipsoid or Elliptical Cylinder

Motivation:

- The oblate ellipsoid offers a wide horizontal profile and smooth curvature, providing both visual appeal and moderate lift ($C_D \approx 0.19$ in x-axis). Its symmetrical shape ensures stability in hover and minimizes sway during slight air disturbances.
- The elliptical cylinder maximizes usable surface area for advertising payload and LED displays. It supports a high frontal area (S_x and S_y both large), though it incurs higher added mass in the vertical direction ($k_{33} \approx 0.859$) and increased damping needs.
- Structural damping may be required for the elliptical cylinder to reduce oscillatory behavior from its flat sidewalls. However, this is acceptable in mostly stationary use cases.
- Figure 7.1 shows the elliptical cylinder scoring highest in surface area related parameters while ranking lower in dynamic performance tradeoff are well aligned with its intended purpose.

Key Insights: Both shapes offer strong visual presence and ample area for branding logos. The oblate ellipsoid is better suited for lighter, more elegant displays, while the elliptical cylinder is ideal for maximal payloads in static or tethered indoor use.

This chapter attributes the multi disciplinary analysis of airship geometries into a parametric evaluation framework. By adding the evaluated data into the equations of motion, we highlight how specific shape dependent properties affect practical performance. These insights enable a structured approach for shape selection in practical missions, setting the foundation for expanded design recommendation systems in future work.

Key Takeaways:

- **Sphere** is favored for minimal helium leakage and robust structural performance but lags in aerodynamic efficiency.
- **Prolate Ellipsoid** offers superior drag and lower added mass, suiting agile or corridor based flights.
- **Oblate Ellipsoid** balances shape aesthetics with moderate drag, though it can face higher stress loads.
- **Elliptical Cylinder** excels in maximum payload lift at the expense of significant aerodynamic and structural drawbacks.

In practice, users/mission specific weighting factors can adjust the normalized scaling e.g., doubling the importance of lift if the payload is critical. Looking ahead, further extension to dynamic shape morphing, advanced envelope materials, or coupled actuator models (for real time altitude and attitude control) could refine this framework and expand its applicability to broader indoor or mixed-environment flight conditions.

CONCLUSION AND RECOMMENDATIONS

This study explores the comprehensive analysis and evaluation of various airship geometries to determine their performance under different criteria. By performing various simulations and parametric studies, we examined the behavior of different airship shapes concerning buoyancy, rigidity, added mass, drag force, and aesthetics. Each geometry, including sphere, oblate, prolate and elliptical cylinder, is assessed to identify the positive and negative parameters for each case.

The spherical blimp demonstrated exceptional performance in terms of buoyancy and rigidity. Its simple design ensures a minimal volume-to-surface area ratio for efficient lift and stability. The spherical blimp also observes balanced stress distribution, contributing to its enhanced structural rigidity for non-rigid cases.

The oblate blimp resolves a satisfactory performance in various criteria, including buoyancy, rigidity, and drag. Its simple design makes it more suitable to manufacture while attaining Wrinkle analysis than the ideal geometry. The recommended application for oblate airship includes research applications requiring a swarm of airships.

With its elongated slender shape, the prolate blimp demonstrated excellent drag performance among all the shapes considered for the study. This geometry is recommended for volatile dynamic performance operations, making it suitable for research applications or indoor-outdoor operations where the velocity of the airship is paramount.

On the other hand, the elliptical blimp expends reduced added mass due to its inherent dynamic stability. However, its high volume-to-surface area ratio impacts the available payload, and the complex curved geometries affect its aesthetics. Despite these limitations, the elliptical blimp is deemed favorable for applications prioritizing stability over other criteria.

In conclusion, this research offers insight into the performance of different airship geometries, attaining considerations while designing and manufacturing airships for different applications.

By understanding the characteristic strength of each shape, designers can make informed choices to tailor custom airships for their specific operational requirements.

The study can be further advanced by coupling all the analysed parameters into a unified software tool, enabling the creation of a rapid design tool without the need of manual and individual derivation of critical parameters using multiple standard and custom software environments. Each parameter can also be further investigated to improve the low control over model fidelity, providing valuable insights about the evaluated parameters.

The dynamic model of equations can also be improved from a simplified 6-DOF model based solely on translational behavior and linear damping to a complete dynamic foundation that can cover effects of the additional forces such as angular accelerations, Coriolis and centripetal forces, and rotational damping. These forces become critical when modeling airships for high speed or high maneuverability cases. Expanding the current model will also allow a better prediction of instability modes and control responses, especially for their applications in dynamic modeling and simulations.

Additionally, the current aerodynamic analysis focuses on the laminar regime and assumes a stable rigid body under low speed flow conditions. While this is suitable for the low conditions often observed in indoor environments, further exploration with higher reynolds number flows are also necessary to improve the performance prediction under turbulent conditions or during transitional behaviors when a sudden gust even in indoor environments can subject a mixed flow condition over the airship. More advanced boundary conditions including slip-free domains could help define drag performance over a larger indoor spaces and enhance the model's reliability when app;ied to more dynamic settings.

Overall, this research lays a foundation for continued exploration into parametric optimization and dynamic modeling for small indoor LTA airships. With further refinement of aerodynamic,

structural and dynamic models, the current framework can evolve into a versatile tool set capable of supporting both academic and manufacturing developments of novel airship designs.

APPENDIX I

APPENDIX: ADDED MASS COMPUTATION

1. Overview

This appendix presents the Python scripts used to compute the added mass matrix of a 3D body. Two numerical integration approaches are used:

1. **Angular-Radial Subdivision**: The surface triangles are subdivided into smaller elements (by radial and angular subdivisions) to numerically evaluate the influence integrals.
2. **Gaussian Quadrature**: A Dunavant quadrature rule is used for accurate integration over triangular facets.

The scripts include functions for:

- Loading and processing geometry from an STL file.
- Computing geometric properties (centroids, normals, areas).
- Calculating the boundary conditions ($\partial\phi/\partial n$) for the six rigid-body modes (three translations and three rotations).
- Building influence matrices C and B via both integration methods.
- Solving for the potential ϕ and integrating the added mass matrix.

2. Python Code

Below is the complete Python code:

Listing I.1: Combined Scripts for Added Mass Computation

```
import numpy as np
from stl import mesh as stl_mesh
from typing import List, Tuple, Optional, Callable

# ----------------------------------
# Common Geometry Functions
```

```
# ------------------------------
def compute_centroid_triangle(A: np.ndarray, B: np.ndarray, C:
    np.ndarray) -> np.ndarray:
    return (A + B + C) / 3.0

def compute_normal(triangle: np.ndarray) -> np.ndarray:
    A, B, C = triangle
    n = np.cross(B - A, C - A)
    norm_n = np.linalg.norm(n)
    return n / norm_n if norm_n > 0 else np.array([0.0, 0.0,
        0.0])

def compute_triangle_properties(vertices: np.ndarray,
                                ref_normal: Optional[np.
                                    ndarray] = None
                                ) -> Tuple[float, np.ndarray,
                                    np.ndarray]:
    A, B, C = vertices
    n = np.cross(B - A, C - A)
    norm_n = np.linalg.norm(n)
    normal = n / norm_n if norm_n > 0 else np.array([0.0, 0.0,
        0.0])
    if ref_normal is not None and np.dot(normal, ref_normal) <
        0:
        normal = -normal
    area = 0.5 * norm_n
    centroid = compute_centroid_triangle(A, B, C)
    return area, centroid, normal
```

```
def load_geometry(stl_path: str):
    geometry = stl_mesh.Mesh.from_file(stl_path)
    triangles = geometry.vectors.astype(np.float64)
    all_vertices = triangles.reshape(-1, 3)
    global_centroid = np.mean(all_vertices, axis=0)
    adjusted_triangles = triangles - global_centroid
    centroids, normals, areas = [], [], []
    for tri in adjusted_triangles:
        A, B, C = tri
        centroid = compute_centroid_triangle(A, B, C)
        normal_vec = np.cross(B - A, C - A)
        norm_mag = np.linalg.norm(normal_vec)
        unit_normal = normal_vec / norm_mag if norm_mag > 0
            else np.array([0.0, 0.0, 0.0])
        area = 0.5 * norm_mag
        centroids.append(centroid)
        normals.append(unit_normal)
        areas.append(area)
    centroids = np.array(centroids)
    normals = np.array(normals)
    areas = np.array(areas)
    adjusted_global_centroid = np.mean(centroids, axis=0)
    return (triangles, adjusted_triangles, centroids, normals,
        areas,
            global_centroid, adjusted_global_centroid)

# ------------------------------
# dphi/dn Calculation
# ------------------------------
```

```
def compute_dphi_dn(adjusted_triangles: np.ndarray, normals:
    np.ndarray) -> np.ndarray:
    num_elements = len(adjusted_triangles)
    dphi_dn = np.zeros((6, num_elements))
    for i in range(num_elements):
        A, B, C = adjusted_triangles[i]
        centroid = compute_centroid_triangle(A, B, C)
        n = normals[i]
        norm_n = np.linalg.norm(n) if np.linalg.norm(n) > 1e
            -12 else 1.0
        alpha, beta, gamma = n / norm_n
        dx, dy, dz = centroid
        dphi_dn[:, i] = [
            alpha,
            beta,
            gamma,
            dy * gamma - dz * beta,
            dz * alpha - dx * gamma,
            dx * beta - dy * alpha
        ]
    return dphi_dn

# ------------------------------------------------------------
# 1) Angular-Radial Subdivision Approach
# ------------------------------------------------------------
def order_vertices(vertices: List[np.ndarray],
                   ref_normal: np.ndarray = np.array([0, 0,
                       1])) -> List[np.ndarray]:
    n_verts = len(vertices)
```

```
    if n_verts < 3:
        return vertices
    if n_verts == 3:
        n = np.cross(vertices[1] - vertices[0], vertices[2] -
            vertices[0])
    else:
        n = np.zeros(3)
        for i in range(n_verts):
            cur = vertices[i]
            nxt = vertices[(i + 1) % n_verts]
            n[0] += (cur[1] - nxt[1]) * (cur[2] + nxt[2])
            n[1] += (cur[2] - nxt[2]) * (cur[0] + nxt[0])
            n[2] += (cur[0] - nxt[0]) * (cur[1] + nxt[1])
    if np.dot(n, ref_normal) < 0:
        vertices = vertices[::-1]
    return vertices


def combined_subdivision_subtriangle(I: np.ndarray,
                                     V1: np.ndarray,
                                     V2: np.ndarray,
                                     Nr: int,
                                     Ntheta: int):
    grid_points = np.empty((Nr + 1, Ntheta + 1, 3), dtype=
        float)
    for i in range(Nr + 1):
        r = i / Nr if Nr > 0 else 0
        for j in range(Ntheta + 1):
            theta = j / Ntheta if Ntheta > 0 else 0
            edge_point = (1 - theta) * V1 + theta * V2
```

```
            grid_points[i, j] = I + r * (edge_point - I)
    elements = []
    for i in range(Nr):
        for j in range(Ntheta):
            if i == 0:
                tri = [grid_points[0, j], grid_points[1, j +
                    1], grid_points[1, j]]
                tri = order_vertices(tri)
                elements.append(("triangle", tri))
            else:
                quad = [grid_points[i, j], grid_points[i, j +
                    1],
                        grid_points[i + 1, j + 1], grid_points
                            [i + 1, j]]
                quad = order_vertices(quad)
                elements.append(("quad", quad))
    return elements

def combined_subdivision_triangle(A: np.ndarray,
                                  B: np.ndarray,
                                  C: np.ndarray,
                                  Nr: int,
                                  Ntheta: int):
    I = compute_centroid_triangle(A, B, C)
    fans = [(I, A, B), (I, B, C), (I, C, A)]
    all_elements = []
    for (I_sub, V1, V2) in fans:
        elems = combined_subdivision_subtriangle(I_sub, V1, V2
            , Nr, Ntheta)
```

```
            all_elements.extend(elems)
        return all_elements

def _quad_approx(quad_vertices: np.ndarray, ref_normal: np.
    ndarray) -> Tuple[float, np.ndarray, np.ndarray]:
        A, B, C, D = quad_vertices
        area1, c1, n1 = compute_triangle_properties(np.array([A, B
            , C]), ref_normal)
        area2, c2, n2 = compute_triangle_properties(np.array([A, C
            , D]), ref_normal)
        area_total = area1 + area2
        if abs(area_total) < 1e-12:
            return 0.0, (A + B + C + D)/4.0, ref_normal
        centroid_combined = (c1 * area1 + c2 * area2) / area_total
        normal_combined = (n1 + n2) / 2.0
        norm_n = np.linalg.norm(normal_combined)
        if norm_n > 1e-12:
            normal_combined /= norm_n
        return area_total, centroid_combined, normal_combined

def compute_influence_coefficients_angular_radial(triangles:
    np.ndarray,
                                                  centroids:
                                                      np.
                                                      ndarray,
                                                  normals: np.
                                                      ndarray,
                                                  Nr: int,
```

```
                                                    Ntheta: int)
                                                        :
    num_elements = len(triangles)
    C_matrix = np.zeros((num_elements, num_elements))
    B_matrix = np.zeros((num_elements, num_elements))
    for i in range(num_elements):
        for j in range(num_elements):
            A, B_, C_ = triangles[j]
            sub_elems = combined_subdivision_triangle(A, B_,
               C_, Nr, Ntheta)
            C_ij = 0.0
            B_ij = 0.0
            for (elem_type, vertices) in sub_elems:
                if elem_type == "triangle":
                    area_sub, sub_centroid, sub_normal =
                       compute_triangle_properties(np.array(
                       vertices),
                else:
                    v = np.array(vertices)
                    area_sub, sub_centroid, sub_normal =
                       _quad_approx(v, normals[j])
                r_ijk = sub_centroid - centroids[i]
```

```
                norm_rijk = np.linalg.norm(r_ijk)
                if norm_rijk < 1e-6:
                    norm_rijk = 1e-6
                rijk_dot_nk = np.dot(r_ijk, sub_normal)
                C_ijk = -(rijk_dot_nk / (norm_rijk ** 3)) *
                   area_sub
                B_ijk = (area_sub / norm_rijk)
                C_ij += C_ijk
                B_ij += B_ijk
            C_matrix[i, j] = C_ij
            B_matrix[i, j] = B_ij
    return C_matrix, B_matrix

# ------------------------------------------------------------
# 2) Gaussian Quadrature Approach
# ------------------------------------------------------------
def compute_triangle_area(A: np.ndarray, B: np.ndarray, C: np.
   ndarray) -> float:
    return 0.5 * np.linalg.norm(np.cross(B - A, C - A))

def get_dunavant_rule(rule: str):
    if rule == "3":
        points = [(0.5, 0.5, 0.0), (0.0, 0.5, 0.5), (0.5, 0.0,
            0.5)]
        weights = [1/3, 1/3, 1/3]
    elif rule == "6":
        points = [
            (0.445948490915965, 0.445948490915965,
               0.108103018168070),
```

```
            (0.445948490915965, 0.108103018168070,
               0.445948490915965),
            (0.108103018168070, 0.445948490915965,
               0.445948490915965),
            (0.091576213509771, 0.091576213509771,
               0.816847572980459),
            (0.091576213509771, 0.816847572980459,
               0.091576213509771),
            (0.816847572980459, 0.091576213509771,
               0.091576213509771)
        ]
        weights = [0.223381589678011, 0.223381589678011,
           0.223381589678011,
                   0.109951743655322, 0.109951743655322,
                      0.109951743655322]
    else:
        raise ValueError(f"Quadrature␣rule␣'{rule}'␣not␣
           implemented␣here.")
    return points, weights

def barycentric_to_cartesian(bary_coords: Tuple[float, float,
   float],
                             vertices: np.ndarray) -> np.
                                ndarray:
    l1, l2, l3 = bary_coords
    return l1 * vertices[0] + l2 * vertices[1] + l3 * vertices
       [2]
```

```
def integrate_over_triangle(func: Callable[[np.ndarray], float
    ],
                            vertices: np.ndarray,
                            rule: str) -> float:
    A, B, C = vertices
    area = compute_triangle_area(A, B, C)
    bary_points, weights = get_dunavant_rule(rule)
    integral_val = 0.0
    for bary, w in zip(bary_points, weights):
        x = barycentric_to_cartesian(bary, vertices)
        integral_val += w * func(x)
    return area * integral_val

def compute_influence_coefficients_gaussian(adjusted_triangles
    : np.ndarray,
                                            centroids: np.
                                               ndarray,
                                            normals: np.
                                               ndarray,
                                            rule: str):
    num_elements = len(adjusted_triangles)
    C_matrix = np.zeros((num_elements, num_elements))
    B_matrix = np.zeros((num_elements, num_elements))
    for i in range(num_elements):
        cent_i = centroids[i]
        for j in range(num_elements):
            vertices_j = adjusted_triangles[j]
            n_j = normals[j]
            def integrand_C(x: np.ndarray) -> float:
```

```
                r_vec = x - cent_i
                r_norm = np.linalg.norm(r_vec)
                r_norm = max(r_norm, 1e-6)
                return -(np.dot(r_vec, n_j) / (r_norm**3))
            def integrand_B(x: np.ndarray) -> float:
                r_vec = x - cent_i
                r_norm = np.linalg.norm(r_vec)
                r_norm = max(r_norm, 1e-6)
                return 1.0 / r_norm
            C_ij = integrate_over_triangle(integrand_C,
                vertices_j, rule)
            B_ij = integrate_over_triangle(integrand_B,
                vertices_j, rule)
            C_matrix[i, j] = C_ij
            B_matrix[i, j] = B_ij
    return C_matrix, B_matrix

# ------------------------------
# Solve for Phi and Compute Added Mass
# ------------------------------
def compute_phi(C_matrix: np.ndarray,
                B_matrix: np.ndarray,
                dphi_dn: np.ndarray) -> np.ndarray:
    N = C_matrix.shape[0]
    A = (2.0 * np.pi) * np.eye(N) - C_matrix
    phi = np.zeros((N, 6))
    for k in range(6):
        rhs = -B_matrix @ dphi_dn[k, :]
        phi[:, k] = np.linalg.solve(A, rhs)
```

```
    return phi

def compute_added_mass_coefficients(phi: np.ndarray,
                                    dphi_dn: np.ndarray,
                                    areas: np.ndarray,
                                    rho: float) -> np.ndarray:
    N = phi.shape[0]
    added_mass = np.zeros((6, 6))
    for i in range(6):
        for j in range(6):
            added_mass[i, j] = -rho * np.sum(phi[:, i] *
                dphi_dn[j, :] * areas)
    return added_mass
```

BIBLIOGRAPHY

Anawati, J. (2024). *Dynamics modelling and simulation of unconventional indoor airships*. Montreal. Retrieved from: https://escholarship.mcgill.ca/concern/theses/s4655n90b.

ANSYS, I. (2021). *ANSYS FLUENT User's Guide, 2021 R2*. United States: ANSYS,Inc.

Azouz, N., Chaabani, S., Lerbet, J. & Abichou, A. (2012). Computation of the Added Masses of an Unconventional Airship. *Journal of Applied Mathematics*, 2012, 1–19.

Bennaceur, S. & Azouz, N. (2012). Contribution of the added masses in the dynamic modelling of flexible airships. *Nonlinear Dynamics*, 67(1), 215–226.

Bessert, N. & Frederich, O. (2005). Nonlinear airship aeroelasticity. *Journal of Fluids and Structures*, 21(8), 731–742.

Bradley, P. (1999). Materials. In Khoury, G. A. & Gillett, J. D. (Eds.), *Airship Technology* (vol. 10, pp. 141–163). Cambridge; New York: Cambridge University Press.

Breches, P.-Y. (2016). *Dynamics modeling and state feedback control of a lighter-than-air cubic blimp*. Montreal. Retrieved from: https://escholarship.mcgill.ca/concern/theses/8623j179f.

Burgess, C. P. (2004). *Airship design*. Honolulu, Hawaii: University Press of the Pacific.

Carbone, G., Martinat, G., Farcy, D. & Harion, J.-L. (2019). Added Masses of generic shape bodies interacting with external walls. *Aerospace Science and Technology*, 90, 70–84. doi: 10.1016/j.ast.2019.04.035.

Carrión, M., Steijl, R., Barakos, G. N. & Stewart, D. (2016). Analysis of Hybrid Air Vehicles Using Computational Fluid Dynamics. *Journal of Aircraft*, 53(4), 1001–1012.

Craig, J. (1999). Aerostatics. In Khoury, G. A. & Gillett, J. D. (Eds.), *Airship Technology* (vol. 10, pp. 211–234). Cambridge; New York: Cambridge University Press.

Cranston, B., AlGhofaily, M. & Palazotto, A. (2017). Design and structural analysis of unique structures under an internal vacuum. *Aerospace Science and Technology*, 68, 68–76.

de Azambuja, R., Fouad, H., Bouteiller, Y., Sol, C. & Beltrame, G. (2022). When Being Soft Makes You Tough: A Collision-Resilient Quadcopter Inspired by Arthropods' Exoskeletons. *2022 International Conference on Robotics and Automation (ICRA)*, pp. 7854–7860. doi: 10.1109/icra46639.2022.9811841.

Dorrington, G. E. (2006). Drag of Spheroid-Cone Shaped Airship. *Journal of Aircraft*, 43(2), 363–371.

Dunavant, D. A. (1985). High degree efficient symmetrical Gaussian quadrature rules for the triangle. *Int. J. Numer. Methods Eng.*, 21(6), 1129–1148.

Fei, X. & Zhengyin, Y. (2009). Drag Reduction for an Airship with Proper Arrangement of Propellers. *Chinese Journal of Aeronautics*, 22(6), 575–582.

Feng, Z.-G. (2010). A Correlation of the Drag Force Coefficient on a Sphere with Interface Slip at Low and Intermediate Reynolds Numbers. *Journal of Dispersion Science and Technology*, 31, 968–974.

Flemmer, R. & Banks, C. (1986). On the drag coefficient of a sphere. *Powder Technology*, 48(3), 217–221.

Fossen, T. I. (1994). *Guidance and control of ocean vehicles*. Chichester; New York: Wiley.

Gawale, A., Raina, A., Pant, R. & Jahagirdar, Y. (2009). Design, Fabrication and Operation of Remotely Controlled Airships in India. *18th AIAA Lighter-Than-Air Systems Technology Conference*.

Ghassemi, H. & Yari, E. (2011). The Added Mass Coefficient computation of sphere, ellipsoid and marine propellers using Boundary Element Method. *Polish Maritime Research*, 18(1), 17–26.

Gomes, S. & Ramos, J. (1998). Airship dynamic modeling for autonomous operation. *Proceedings. 1998 IEEE International Conference on Robotics and Automation (Cat. No.98CH36146)*, 4, 3462–3467. doi: 10.1109/ROBOT.1998.680973.

Hengne, S. S., Korade, D. N. & Jagtap, K. R. (2019). Design and simulation of airship model. pp. 020017.

Hevner, A. & Chatterjee, S. (2010). Design Science Research in Information Systems. In *Integrated Series in Information Systems* (pp. 9–22). Boston, MA: Springer US.

Hoerner, S. F. (1992). *Fluid-dynamic drag: practical information on aerodynamic drag and hydrodynamic resistance* (ed. 2nd ed). Bakersfield: Hoerner Fluid Dynamics.

Javanmard, E., Mansoorzadeh, S. & Mehr, J. A. (2020). A new CFD method for determination of translational added mass coefficients of an underwater vehicle. *Ocean Engineering*, 215, 107-857.

Jones, S. P. & DeLaurier, J. D. (1983). Aerodynamic estimation techniques for aerostats and airships. *Journal of Aircraft*, 20(2), 120–126.

Khoury, G. A. & Gillett, J. D. (Eds.). (1999). *Airship technology*. Cambridge ; New York: Cambridge University Press.

Korotkin, A. I. (2009). *Added masses of ship structures*. United Kingdom: Springer.

Li, Y. & Nahon, M. (2007). Modeling and Simulation of Airship Dynamics. *Journal of Guidance, Control, and Dynamics*, 30(6), 1691–1700.

Li, Y., Nahon, M. & Sharf, I. (2011). Airship dynamics modeling: A literature review. *Progress in Aerospace Sciences*, 47(3), 217–239.

Liu, C. (2014). New Method of Fabric Wrinkle Measurement Based on Image Processing. *Fibres and Textiles in Eastern Europe*, 103, 51-55.

Liu, J.-m., Lu, C.-j. & Xue, L.-p. (2008). Investigation of Airship Aeroelasticity Using Fluid-Structure Interaction. *Journal of Hydrodynamics*, 20(2), 164–171.

Liu, Y., Zeng, P. & Lei, L. P. (2013). Experimental Study on the Stability Properties of Different Design of Tandem Wing Airship Models. *Applied Mechanics and Materials*, 457-458, 1611–1614.

Lu, L., Song, H., Wang, Y. & Huang, C. (2019). Deformation behavior of non-rigid airships in wind tunnel tests. *Chinese Journal of Aeronautics*, 32(3), 611–618.

Luchsinger, R., Pedretti, A., Steingruber, P. & Pedretti, M. (2004). LIGHT WEIGHT STRUCTURES WITH TENSAIRITY. 159-198.

MatWeb. (2020). *Fabric Material n°Mylar, Polyester Film, 1000 Gauge*. MatWeb: Online Materials Information Resource. Retrieved from: https://compositeskn.org/KPC/Reference:4ac81734-995f-3de2-a118-fdda0677547b.

Morino, L. (1974). *A General Theory of Unsteady Compressible Potential Aerodynamics*. Boston. Retrieved from: https://ntrs.nasa.gov/citations/19750004821.

Mueller, J., Paluszek, M. & Zhao, Y. (2004). Development of an Aerodynamic Model and Control Law Design for a High Altitude Airship. *AIAA 3rd "Unmanned Unlimited" Technical Conference, Workshop and Exhibit*.

Mulay, S. S. & Pant, R. S. (2013). Design Fabrication and Flight testing of a Non-rigid Indoor Airship. *AIAA Lighter-Than-Air Systems Technology (LTA) Conference*.

Nong, Y. (2012). *Design of Small Highly Maneuverable Airships*. Montreal. Retrieved from: https://escholarship.mcgill.ca/concern/theses/n009w5992.

Pecora, I. (2017). *Finite Element Simulation of Large-Scale Confined Inflatable Structures*.

Quarteroni, A., Sacco, R. & Saleri, F. (2007). *Numerical Mathematics*. New York, NY: Springer New York.

Raymer, D. P. (2006). *Aircraft design: A conceptual approach* (ed. 4. ed.). Reston, Va.: American Institute of Aeronautics and Astronautics.

Reddy, M. D. & Pant, R. S. (2018). CFD analysis of axisymmetric bodies of revolution using OpenFOAM. *Applied Aerodynamics Conference, 2018*, 1–10.

Shih, T.-H., Liou, W. W., Shabbir, A., Yang, Z. & Zhu, J. (1995). A new k-epsilon eddy viscosity model for high reynolds number turbulent flows. *Computers & Fluids*, 24(3), 227–238.

Smith, M. (2009). *ABAQUS/Standard User's Manual, Version 6.9*. United States: Dassault Systems Simulia Corp.

St-Onge, D., Gosselin, C. & Reeves, N. (2015). Dynamic modelling and control of a cubic flying blimp using external motion capture. *Proceedings of the Institution of Mechanical Engineers, Part I: Journal of Systems and Control Engineering*, 229(10), 970–982.

Su, J. & Xu, B. (1999). Fabric wrinkle evaluation using laser triangulation and neural network classifier. *Optical Engineering*, 38(10), 1688–1693. doi: 10.1117/1.602220.

Sun, J., Yao, M., Xu, B. & Bel, P. (2011). Fabric wrinkle characterization and classification using modified wavelet coefficients and support-vector-machine classifiers. *Textile Research Journal*, 81(9), 902–913. doi: 10.1177/0040517510391702.

Suñol, A. & Vučinić, D. (2020). *Tensairity, an Extra-Light Weight Structure for Airships*. Singapore: Springer. doi: 10.1007/978-981-13-9806-3_6.

Takeda, K. & Kato, M. (1992). Wind tunnel blockage effects on drag coefficient and wind-induced vibration. *Journal of Wind Engineering and Industrial Aerodynamics*, 42(1-3), 897–908.

Thompson, J. F., Warsi, Z. U. A. & Mastin, C. W. (1985). Numerical grid generation: Foundations and applications.

Tran-Cong, S., Gay, M. & Michaelides, E. E. (2004). Drag coefficients of irregularly shaped particles. *Powder Technology*, 139(1), 21–32.

Tuveri, M., Ceruti, A. & Marzocca, P. (2014). Added masses computation for unconventional airships and aerostats through geometric shape evaluation and meshing. *International Journal of Aeronautical and Space Sciences*, 15(3), 241–257.

Wang, C. G., Liu, M. X. & Tan, H. F. (2017). Interactive buckling of an inflated envelope under mechanical and thermal loads. *Acta Mechanica Sinica*, 33(1), 159–172.

Wang, X.-L., Fu, G.-Y., Duan, D.-P. & Shan, X.-X. (2010). Experimental Investigations on Aerodynamic Characteristics of the ZHIYUAN-1 Airship. *Journal of Aircraft*, 47(4), 1463–1468.

White, F. M. & Xue, H. (2021). *Fluid mechanics* (ed. Ninth edition). New York, NY: McGraw-Hill.

Wu, X., Wang, Y., Huang, C., Liu, Y. & Lu, L. (2015). Experiment and numerical simulation on the characteristics of fluid–structure interactions of non-rigid airships. *Theoretical and Applied Mechanics Letters*, 5(6), 258–261.